# COMPARISON STUDY OF MAGNETOTELLURIC INVERSION USING DIFFERENT TRANSFER FUNCTIONS

by

David Frank Bierman

A thesis submitted to the faculty of
The University of Utah
in partial fulfillment of the requirements for the degree of

Master of Science

in

Geophysics

Department of Geology and Geophysics

The University of Utah

August 2014

# The University of Utah Graduate School

## STATEMENT OF THESIS APPROVAL

The thesis of **David Frank Bierman**

has been approved by the following supervisory committee members:

| | | |
|---|---|---|
| **Michael S. Zhdanov** | , Chair | **12/18/13** Date Approved |
| **Eric U. Petersen** | , Member | **12/18/13** Date Approved |
| **Alexander V. Gribenko** | , Member | **12/18/13** Date Approved |

and by **John M. Bartley** , Chair/Dean of

the Department/College/School of **Geology and Geophysics**

and by David B. Kieda, Dean of The Graduate School.

# ABSTRACT

Near-surface inhomogeneities (NSI) are a major problem that distorts magnetotelluric (MT) data. In this thesis, I have developed a method of 3D inversion of MT data based on the phase-tensor approach. Theoretically, unlike conventional MT apparent resistivities, the phase-tensor data are not distorted by the near-surface inhomogeneities and thus should provide more reliable information about deep geoelectrical structures. I have derived the relationships between Fréchet derivatives of the phase tensor and those of the MT impedance components. Once the sensitivities are known, the method closely follows Consortium for Electromagnetic Modeling and Inversion's (CEMI's) 3D MT inversion algorithm, which is based on the integral equation (IE) formulation of EM field equations and receiver footprint approach. In this thesis, I conduct a comparison study of 3D MT inversions, using impedance tensor and phase tensor methods. I present a case study using the MT data from the McArthur River area. The results from the impedance tensor compared well with the results from other publications. The phase tensor results did not compare well with any other results. This indicates that the phase tensor method, being theoretically very robust to near-surface distortions, in practice does not work as well as one would expect. I explain this phenomenon by the significant effects of noise in the field MT data on the components of the phase tensor.

To Andrey Nikolayevich Tikhonov

# CONTENTS

# ACKNOWLEDGMENTS

I would like to express my gratitude to my supervisory committee chair, Professor Michael Zhdanov, for his guidance and support in this research. I am also grateful for the support and useful discussion from my committee members, Professor Erich U. Petersen and Alex Gribenko.

I would also like to express my thanks to, the Consortium for Electromagnetic Modeling and Inversion (CEMI) and the Department of Geology and Geophysics of the University of Utah for supporting my research and study.

I am also thankful for the support and advice given from Martin Cuma and the support and resources from the Center for High performance Computing at the University of Utah is greatly acknowledged.

Finally, I would like to give special thanks to Le Wan, Glenn Wilson, David Chapman, Michael Davis, and Paul Gettings for their support.

# CHAPTER 1

# INTRODUCTION

The magnetotelluric (MT) method makes use of natural electromagnetic (EM) fields, from magnetospheric and ionospheric currents, measured on the surface of the Earth to study the subsurface electrical resistivity. The geoelectrical model of the subsurface formations is obtained by inverting the observed impedance data, which are a ratio of the electric and magnetic fields. The first papers on this subject were published in 1950 by A. N. Tikhonov and in 1953 by L. Cagniard. This method started with 1D models, which led to 2D, and eventually 3D models. The MT method has significantly improved in recent years because of improvements in acquisition equipment, and advancements in computing capabilities (Zhdanov et al., 2011). There are many ways to do forward modeling and inversion which are used in 2D and 3D modeling algorithms. Some examples of forward modeling include finite-difference (Mackie et al., 1993), finite-element (Travis and Chave, 1989), projection (Berdichevsky and Dmitriev, 1976a), integral equation (Berdichevsky and Dmitriev, 1976a), and finite-volume methods (Farquharson et al., 2002). The majority of inversion algorithms are based on regularized conjugate gradient, Newton, or least squares methods (Zhdanov, 2002). There are many 2D and 3D inversion algorithms available, for example, Mackie et al., (1993), Farquharson et al., (2002), Rodi and Mackie (2001), and Siripunvaraporn et al., (2005). In this thesis, a 3D inversion algorithm is used, which employs the integral equation method for forward modeling of the MT data, and regularized conjugate gradient method for the inversion. The forward modeling and inversion processes have been parallelized, to improve speed and memory requirements (Zhdanov et al., 2011; Zhdanov, 2009).

One problem that exists in the MT method is deviations in the electric fields due to galvanic distortions. These deviations produce artifacts in MT data. They are

caused by buildup of excess charge in the near-surface inhomogeneities (NSI), and they affect data at high frequencies. They also affect data at lower frequencies which causes a misrepresentation of the deeper layers (Berdichevsky and Dmitriev, 1976a; 2002; Berdichevsky and Zhdanov, 1984; Jiracek, 1990; Gribenko and Zhdanov, 2011; Groom and Bahr; 1992). The electric fields are deflected to higher or lower values than what would be otherwise observed. The magnetic fields are much less affected by NSI because they are produced by the integrated effect of the excess currents in the inhomogeneities. The NSI cause the apparent resistivity, when plotted on a log-coordinate scale, to have static shifts. The NSI result in higher or lower impedance than what would be observed in the absence of the NSI. As stated in Jiracek (1990) and Sasaki (2004), phase sounding curves are less affected by galvanic distortions, however, phase still maybe affected, depending on the frequency as stated by Chave and Jones (2012). One other affect that Chave and Jones (2012) mention is that the auxiliary components of the impedance tensor are also majorly distorted in the presence of galvanic distortions. The above phenomena will be demonstrated by synthetic modeling in this thesis.

Many techniques have been used to remove the effects of NSI including using a joint inversion of MT and magnetovariational (MV) data (Berdichevsky and Dmitriev, 1976a; Zhu, 2012), decomposition of the impedance tensor (Groom and Bahr, 1992), use of invariant response parameters (Berdichevsky and Dmitriev, 1976b), curve shifting (Jones, 1988), statistical averaging using spatial filtering (Berdichevsky et al., 1989), and use of distortion tensors (Schmucker, 1970). In Jiracek (1990) the following advice is given: "The reader may be disappointed to learn that no magical solution to all problems of near-surface EM distortion is available." Chave and Jones (2012) summarize the removal techniques into two categories which are mathematically or physically-based.

A relatively new approach to remove effects due to galvanic distortions is the phase tensor method published by Caldwell et al., (2004). It is a method of removing distortions due to NSI in the electric fields. The method of 3D inversion of the phase tensor has been developed by Gribenko and Zhdanov (2011). They did a synthetic modeling study which compared the effects due to NSI in inversion results of the

impedance and phase tensors. From their study, it appeared that the phase tensor could be used for removing the effects due to NSI in inversion. Currently there are two papers that have suggested the methods for 3D inversion of the phase tensor, (Pankratov and Kuvshinov, 2010; Egbert and Kelbert, 2012), but they have not applied their methods to MT data.

The purpose of this thesis is to conduct a comparison study of MT inversion using different MT transfer functions and to select the most effective function in modeling the subsurface resistivity. We use a MT data set from the McArthur River area to study the MT inversion of the impedance and phase tensors. The deposit contains the highest grade uranium in the world (Jefferson et al., 2007). It is an unconformity-type uranium deposit, and it is located in the Athabasca basin which is situated in the east and west sides of Alberta and Saskatchewan provinces of Canada, respectively. This MT survey was funded by a Canadian government and industrial partnership called EXTECH-IV (Exploration science and TECHnology initiative). The goal of EXTECH-IV was to develop new techniques of locating unconformity type uranium deposits (Jefferson et al., 2003).

In this thesis, the results from the impedance and phase tensors are examined with the four inversion results that were compared by Craven et al. (2006). Most of the inversion results have very low resistivity anomalies oriented in Northeast-Southwest. There is a reverse fault (called the P2 fault) also oriented in the Northeast-Southwest, and in the same location. The anomalies are interpreted to be caused by graphite deposits, which are in part responsible for the precipitation of uranium in this location. Graphite is very conductive in comparison to the surrounding material, which makes MT a very effective means of exploration in this case (Tuncer et al., 2006).

From synthetic modeling experiments and the inversion results of the McArthur River data set, it appears that the full MT tensor inversion takes NSI into account properly, at the same time, the full phase tensor is not an effective means of subsurface modeling in this case. The phase tensor does not work because the best-fit predicted data does not match the McArthur River observed data well enough. It appears that this mismatch is because of noise affecting the auxiliary components of the impedance tensor. The principal components are much more predictable while the

auxiliary components are noisy and less predictable (Chave and Jones, 2012). The principal and full impedance methods generated results which compare well with the geology and other publications using the same data set.

# CHAPTER 2

# FOUNDATIONS OF THE MAGNETOTELLURIC (MT) METHOD

The MT method uses natural EM fields to calculate the conductivity or, its inverse, resistivity, of the subsurface of the Earth. The method assumes a horizontal plane 2D EM wave. In 1950, A. N. Tikhonov presented the mathematical relationship between observed electric and magnetic fields of the Earth, and the subsurface conductivity. Then in 1953, L. Cagniard also published on this subject, and expanded it for exploration of the subsurface Earth with great optimism stating it would replace other exploration methods. Originally it was simply a 1D, then 2D, and now it is a full 3D method of exploration (Zhdanov, 2009). The benefits of the MT method are that it is relatively inexpensive, the source is free, it can be used for deeper depths of investigation than other EM methods because of its larger frequency spectrum, and it has a very low impact on the environment. Some of the disadvantages of the MT method are it takes a longer time to get all desired frequencies, and there are natural dead spots where no data can be obtained (Simpson and Bahr, 2005). One other issue is static shifts due to NSI which cause the electric field data to have higher or lower apparent resistivity amplitudes than what are produced by the Earth (Berdichevsky and Dmitriev, 2002). The MT method is used to study the mantle, and for the deeper hydrocarbon, mining, and geothermal exploration. The MT method is great for detecting conductive materials of the subsurface for example graphite surrounded by resistive materials. This is because EM fields are not attenuated in resistive materials allowing them to pass through them very easily (Simpson and Bahr, 2005). One other application of the MT method is hydrocarbon exploration below volcanic basalts. The seismic method does not work effectively within the basalts;

however, the MT method passes through them easily because they are very resistive (Chatterjee et al., 2008; Peace et al., 2002).

## 2.1 Tikhonov-Cagniard model of MT fields

The simplest 1D model of MT fields comes from Tikhonov (1950), and Cagniard (1953). It assumes a plane vertically incident monochromatic EM wave that goes through the Earth. The model of the Earth is assumed to be homogeneous isotropic layers with boundaries in the horizontal direction. It also assumes a Cartesian coordinate system with z pointing down, x and y in the north and east directions, respectively. The final results of these assumptions is a simple relationship between measured electric and magnetic fields

$$\mathbf{E}_\tau = \begin{bmatrix} 0 & 1 \\ -1 & 0 \end{bmatrix} \mathbf{H}_\tau, \tag{2.1}$$

where

$$\mathbf{E}_\tau = \begin{bmatrix} E_x \\ E_y \end{bmatrix}, \ \mathbf{H}_\tau = \begin{bmatrix} H_x \\ H_y \end{bmatrix}$$

where the electric and magnetic fields are represented by E and H, respectively. They are the horizontal components of the MT field and Z is the complex scalar called the *Tikhonov-Cagniard impedance*. In the 1D case the following relationships are true:

$$E_x = ZH_y, \ E_y = -ZH_x, \ Z = \frac{E_x}{H_y} = -\frac{E_y}{H_x}. \tag{2.2}$$

The impedance (Z) is rotationally invariant, and it is proportional to the conductivity ($\sigma$) of the Earth. The problem with this simple model is it has been proven to be wrong in certain cases due to the Earth being more complex than a 1D model. In order to correct the cases that were incorrect, the MT impedance tensor was developed which holds true in all cases (Berdichevsky and Dmitriev, 2002).

## 2.2 MT impedance tensor and its properties

The MT impedance tensor is given as follows:

$$Z = \begin{bmatrix} Z_{xx} & Z_{xy} \\ Z_{yx} & Z_{yy} \end{bmatrix}. \tag{2.3}$$

Then using the relationship between the impedance and the electric and magnetic fields in matrix form:

$$\begin{bmatrix} E_x \\ E_y \end{bmatrix} = \begin{bmatrix} Z_{xx} & Z_{xy} \\ Z_{yx} & Z_{yy} \end{bmatrix} \begin{bmatrix} H_x \\ H_y \end{bmatrix}, \tag{2.4}$$

gives the following two equations:

$$E_x = Z_{xx}H_x + Z_{xy}H_y, \tag{2.5}$$

$$E_y = Z_{yx}H_x + Z_{yy}H_y. \tag{2.6}$$

The principle components of the impedance tensor are $Z_{xy}$, $Z_{yx}$, and $Z_{xx}$, $Z_{yy}$ are called the auxiliary components. In the simplest case, with a horizontally uniform Earth model, the auxiliary components are equal to zero, and the principle components have the following relationship $Z_{xy} = -Z_{yx} = Z$. The auxiliary components are an indicator the asymmetry of the anomalous body; they are equal to zero if the body is symmetric about the vertical plane passing through the survey line (Berdichevsky and Dmitriev, 2002). All of the components of the impedance tensor are complex numbers, and from them we can also calculate the apparent resistivity given by the following equations:

$$\begin{aligned} \rho_{xy} &= \frac{1}{\omega\mu_0}|Z_{xy}|^2 \\ \rho_{yx} &= \frac{1}{\omega\mu_0}|Z_{yx}|^2 \end{aligned} \tag{2.7}$$

where $\rho$ represents the apparent resistivity, $\omega$ is the angular frequency, and $\mu_0 = 4\pi \times 10^{-7} H/m$ is the permeability of free space (Berdichevsky and Dmitriev, 2002).

One other important calculation is the skin depth. It is used to determine how deep in the subsurface the MT data can obtain information. It is calculated using the following equation:

$$\delta = \sqrt{10^7 \rho T / 4\pi^2} \approx 500\sqrt{\rho T} \tag{2.8}$$

where $\delta$ is the skin depth in meters, T is the period, and $\rho$ is the resistivity. The skin depth is the depth the signal can go before its strength is diminished by 1/e (= 0.368) where e is Euler's number (Zhdanov, 2009).

## 2.3 MT phase tensor and its properties

The phase tensor was introduced by Caldwell et al. (2004). The idea behind it is one can remove electric distortions by mathematical manipulation. If we assume

that impedance can be represented by $\left[\mathbf{Z}^S\right] = [\mathsf{e}]\left[\mathbf{Z}^R\right]$ where $\left[\mathbf{Z}^S\right]$ and $\left[\mathbf{Z}^R\right]$ are the superposition and regional impedances, and $[\mathsf{e}]$ is the real tensor that represents electric distortions, then separate impedances into real and imaginary parts:

$$\begin{aligned}\left[\mathbf{Z}^R\right] &= \left[\mathbf{X}^R\right] + i\left[\mathbf{Y}^R\right], \\ \left[\mathbf{Z}^S\right] &= \left[\mathbf{X}^S\right] + i\left[\mathbf{Y}^S\right] = [\mathsf{e}]\left[\mathbf{X}^R\right] + i[\mathsf{e}]\left[\mathbf{Y}^R\right],\end{aligned} \tag{2.9}$$

where $[\mathbf{X}^q]$ and $[\mathbf{Y}^q]$ are the real and imaginary tensors of the impedance tensors, respectively, this implies the following:

$$\left[\mathbf{X}^S\right] = [\mathsf{e}]\left[\mathbf{X}^R\right], \quad \left[\mathbf{Y}^S\right] = [\mathsf{e}]\left[\mathbf{Y}^R\right]. \tag{2.10}$$

Now if a real valued tensor is used which is analogous to phase in 1D:

$$\begin{aligned}\left[\Phi^S\right] &= \left[\mathbf{X}^S\right]^{-1}\left[\mathbf{Y}^S\right] = \left[\mathbf{X}^R\right]^{-1}[\mathsf{e}]^{-1}[\mathsf{e}]\left[\mathbf{Y}^R\right] \\ &= \left[\mathbf{X}^R\right]\left[\mathbf{Y}^R\right] = \left[\Phi^R\right] = \begin{bmatrix}\Phi_{xx} & \Phi_{xy} \\ \Phi_{yx} & \Phi_{yy}\end{bmatrix},\end{aligned} \tag{2.11}$$

then the electric distortions are canceled out, and hence noise, caused by electric distortions, is removed from the impedance. The individual components of the phase tensor will be derived later in this thesis. The important thing to note is the electric distortions, which are represented by $[\mathsf{e}]$, are completely removed when using the MT phase tensor. All the components of the phase tensor are real numbers. Note that noise that effects the auxiliary components, caused by instrumentation or the environment, is not canceled; this may explain problems with real data.

## 2.4 Principles of interpretation of MT data

MT data are more difficult to analyze than other methods of exploration for example seismology or gravity. This is because MT data requires a lot of processing of the observed values before properties of the subsurface Earth can be observed (Booker, 2012). Once the data are in the format of impedance, they are plotted with respect to the square-root of period. The apparent resistivity and phase are also plotted in the same manner. One thing that is common for data sets are the xy components have a phase that lies between the values of 0 and 90 degrees. The yx components have a phase that is between -90 and -180 degrees. When the values of impedance are converted to complex numbers both the real and imaginary part of xy and yx are greater than 0, and less than 0, respectively. The apparent resistivity

can show local areas that are more or less conductive than the surroundings. 2D and 3D inversion methods have been shown to be an effective means of mapping the subsurface conductivity (Zhdanov, 2009).

# CHAPTER 3

# FORWARD MODELING OF IMPEDANCE AND PHASE TENSORS

In this chapter, we introduce the forward modeling operator for the MT method. The forward modeling operator is what converts the model ($\mathbf{m}$) to the predicted data ($\mathbf{d}$). It is usually represented as the operator A in $\mathrm{A}(\mathbf{m}) = \mathbf{d}$. One example of a forward modeling operator is the calculation of impedance. For simplicity, consider the 1D impedance equation (2.2)

$$Z = \frac{E_x}{H_y}.$$

The forward modeling operator (A) in this case is the calculation of impedance (Z), the model ($\mathbf{m}$) is the conductivity ($\sigma$), and the observed data ($\mathbf{d}$) is the electric ($E_x$) and magnetic ($H_y$) fields. In this case the conductivity ($\sigma$) of the subsurface of the Earth affects the impedance, which can be calculated by the ratio of electric and magnetic fields measured on the surface of the Earth.

There are many methods of forward modeling; some examples include finite-difference, finite-element, projection, and integral equation methods (Berdichevsky and Dmitriev, 1976). The integral equation method (IE) is used in this thesis, due to its advantage of a smaller inversion domain than other forward modeling methods.

## 3.1 Principles of EM forward modeling using integral equation (IE) method

As mentioned above, the IE method is used in this work, and it computes the electric and magnetic fields. In this thesis, the method will only be introduced following the approach described in Hursán and Zhdanov (2002). Consult their paper for more information on this method. If we have an anomalous body below the surface of the Earth with domain D, background conductivity $\sigma_b$, and anomalous conductivity

$\Delta\sigma$, we can represent the conductivity ($\sigma$) by $\sigma = \sigma_b + \Delta\sigma$. The addition of the background and anomalous fields can be used to calculate the electric and magnetic fields;

$$\mathbf{E} = \mathbf{E}^b + \mathbf{E}^a,\ \mathbf{H}=\mathbf{H}^b + \mathbf{H}^a \tag{3.1}$$

where $\mathbf{E}$ represents the electric field, and $\mathbf{H}$ represents the magnetic field. The background fields, $\mathbf{E}^b$ and $\mathbf{H}^b$ are produced by the background conductivity ($\sigma_b$), and the anomalous fields, $\mathbf{E}^a$ and $\mathbf{H}^a$ are produced by the anomalous conductivity ($\Delta\sigma$).

The anomalous fields in the domain D can be calculated based on the integral of excess currents:

$$\mathbf{E}^a(\mathbf{r}_j) = \mathbf{G}_E[\Delta\sigma(\mathbf{r})\mathbf{E}] = \iiint_D \hat{\mathbf{G}}_E(\mathbf{r}_j|\mathbf{r})\Delta\sigma(\mathbf{r}) \cdot \left[\mathbf{E}^b(\mathbf{r}) + \mathbf{E}^a(\mathbf{r})\right] dv, \tag{3.2}$$

$$\mathbf{H}^a(\mathbf{r}_j) = \mathbf{G}_H[\Delta\sigma(\mathbf{r})\mathbf{E}] = \iiint_D \hat{\mathbf{G}}_H(\mathbf{r}_j|\mathbf{r})\Delta\sigma(\mathbf{r}) \cdot \left[\mathbf{E}^b(\mathbf{r}) + \mathbf{E}^a(\mathbf{r})\right] dv, \tag{3.3}$$

where $\ddot{\mathbf{G}}_E(\mathbf{r}_j|\mathbf{r})$ and $\ddot{\mathbf{G}}_H(\mathbf{r}_j|\mathbf{r})$represent the electric and magnetic Green's tensors, and $\mathbf{G}_E$ and $\mathbf{G}_H$ represent the electric and magnetic Green's operators, respectively. The Green's tensors, above, are the solutions to the following differential equations:

$$\nabla \times \hat{\mathbf{G}}_H = \sigma_b \hat{\mathbf{G}}_E + \hat{\delta}, \tag{3.4}$$

and

$$\nabla \times \hat{\mathbf{G}}_E = i\omega\mu_0 \hat{\mathbf{G}}_B \tag{3.5}$$

where $\mu_0 = 4\pi \times 10^{-7} H/m$ is the free-space magnetic permeability, and $\hat{\delta}$ is the tensor delta function

$$\hat{\delta} = \begin{bmatrix} \delta(\mathbf{r}_j - \mathbf{r}) & 0 & 0 \\ 0 & \delta(\mathbf{r}_j - \mathbf{r}) & 0 \\ 0 & 0 & \delta(\mathbf{r}_j - \mathbf{r}) \end{bmatrix}. \tag{3.6}$$

For a horizontally-layered background model, it can be shown that equations (3.4) and (3.5) can be simplified to the Hankel transform of some elementary functions. Assuming that $\mathbf{r}_j$ is within the domain D of the anomalous conductivity equation (3.2) can be reduced to a singular vector Fredholm integral equation of the second kind which produces the anomalous electric field $\mathbf{E}^a$

$$\mathbf{E}^a = \mathbf{G}_E \left[ \Delta\sigma \left( \mathbf{r} \right) \left( \mathbf{E}^b \left( \mathbf{r} \right) + \mathbf{E}^a \left( \mathbf{r} \right) \right) \right], \mathbf{r}, \mathbf{r}_j \in D, \tag{3.7}$$

which simplifies the total electric field to the following equations,

$$\mathbf{E} \left( \mathbf{r}_j \right) = \mathbf{E}^b \left( \mathbf{r}_j \right) + \mathbf{G}_E \left[ \Delta\sigma \left( \mathbf{r} \right) \mathbf{E} \left( \mathbf{r} \right) \right], \mathbf{r}, \mathbf{r}_j \in D. \tag{3.8}$$

After the electric field is determined, equations (3.2) and (3.3) are used to calculate the electric and magnetic fields at the receiver locations.

## 3.2 Forward modeling of MT impedance tensor

There are two standard polarizations for the impedance tensor, they included the transverse electric (TE) and the transverse magnetic (TM). The TE mode describes electric fields moving in the strike direction (x direction) which induces magnetic fields perpendicular to the strike. The TM mode describes magnetic fields parallel to the strike direction and electric fields perpendicular to the strike direction. The TE and TM mode therefore, describe current flowing parallel and perpendicular to the strike, respectively. The TE mode therefore, has the following background conductivity:

$$\mathbf{E}^{b(1)} = \left\{ {E_x}^{b(1)}, 0, 0 \right\}, \ \mathbf{H}^{b(1)} = \left\{ 0, {H_y}^{b(1)}, 0 \right\}. \tag{3.9}$$

While the TM mode, has the following background conductivity:

$$\mathbf{E}^{b(2)} = \left\{ 0, {E_y}^{b(2)}, 0 \right\}, \mathbf{H}^{b(2)} = \left\{ {H_x}^{b(2)}, 0, 0 \right\}. \tag{3.10}$$

Using the combination of the TE and TM polarizations, one can solve for the individual components of the impedance. With the $Z_{xy}$ and $Z_{xx}$ component derived from equation (2.5) as follows:

$$Z_{xy} = \frac{{E_x}^{(1)} {H_x}^{(2)} - {E_x}^{(2)} {H_x}^{(1)}}{{H_y}^{(1)} {H_x}^{(2)} - {H_y}^{(2)} {H_x}^{(1)}}, Z_{xx} = \frac{{E_x}^{(1)} {H_y}^{(2)} - {E_x}^{(2)} {H_y}^{(1)}}{{H_x}^{(1)} {H_y}^{(2)} - {H_x}^{(2)} {H_y}^{(1)}}. \tag{3.11}$$

The other two components are derived from equation (2.6):

$$Z_{yy} = \frac{{E_y}^{(1)} {H_x}^{(2)} - {E_y}^{(2)} {H_x}^{(1)}}{{H_y}^{(1)} {H_x}^{(2)} - {H_y}^{(2)} {H_x}^{(1)}}, Z_{yx} = \frac{{E_y}^{(1)} {H_y}^{(2)} - {E_y}^{(2)} {H_y}^{(1)}}{{H_x}^{(1)} {H_y}^{(2)} - {H_x}^{(2)} {H_y}^{(1)}} \tag{3.12}$$

Full impedance inversion includes all of the above components from the impedance tensor, but principal impedance inversion only includes $Z_{xy}$ and $Z_{yx}$ components (Zhdanov, 2009; Simpson and Bahr, 2005).

## 3.3 Forward modeling of MT phase tensor

As mentioned earlier in this thesis, the impedance components are all complex numbers. They can be separated as follows:

$$Z = \begin{bmatrix} X_{xx} & X_{xy} \\ X_{yx} & X_{yy} \end{bmatrix} + i \begin{bmatrix} Y_{xx} & Y_{xy} \\ Y_{yx} & Y_{yy} \end{bmatrix} = X + iY, \tag{3.13}$$

where

$$X = \begin{bmatrix} X_{xx} & X_{xy} \\ X_{yx} & X_{yy} \end{bmatrix}, \text{ and } Y = \begin{bmatrix} Y_{xx} & Y_{xy} \\ Y_{yx} & Y_{yy} \end{bmatrix}, \tag{3.14}$$

are the real and imaginary impedance tensors.

The phase tensor is given the following definition as was described earlier:

$$\Phi = X^{-1}Y, \tag{3.15}$$

where $X^{-1}$ represents the inverse of $X$.

Using the Cartesian coordinate system, the MT phase tensor can be derived as follows:

$$\begin{bmatrix} \Phi_{xx} & \Phi_{xy} \\ \Phi_{yx} & \Phi_{yy} \end{bmatrix} = \frac{1}{\det(X)} \begin{bmatrix} X_{yy}Y_{xx} - X_{xy}Y_{yx} & X_{yy}Y_{xy} - X_{xy}Y_{yy} \\ X_{xx}Y_{yx} - X_{yx}Y_{xx} & X_{xx}Y_{yy} - X_{yx}Y_{xy} \end{bmatrix} \tag{3.16}$$

where $\det(X)$ is the determinant of $X$.

The components of the MT phase tensor are all real. The diagonal components $\Phi_{xx}$, $\Phi_{yy}$, and the off-diagonal components $\Phi_{xy}$, $\Phi_{yx}$ are the principle and auxiliary components, respectively (Caldwell et al., 2004).

# CHAPTER 4

# INVERSION OF MT IMPEDANCE AND PHASE TENSOR

In the last chapter forward modeling was described. Associated with forward modeling is inversion. In many exploration geophysical applications, data ($\mathbf{d}$) are collected on the surface of the Earth. There is no way to know the exact physical properties of the Earth that generate the data (Zhdanov, 2002). A model ($\mathbf{m}$) is created that represents the physical properties of the Earth, which are a possible source of the data. The forward modeling operator ($A(\mathbf{m})$) is something that converts the model space to the data space which is called the predicted data. The forward modeling operator for MT applications is nonlinear, and there is no unique solution $\mathbf{m}$. In order to find the best possible model that creates predicted data from the forward modeling operator, which matches the observed data, inversion theory must be used. In this thesis the regularized conjugate gradient method is used, and will only be briefly described. For a more complete description of inversion theory the reader should consult a textbook on inversion theory, for example, Zhdanov (2002).

## 4.1 Principles of regularized geophysical inversion

The goal of any inverse problem is to find the best model ($\mathbf{m}$) that will generate predicted data to match the observed data. This is done by minimizing the parametric functional ($P^{\alpha}(\mathbf{m}, \mathbf{d})$) which is defined as:

$$P^{\alpha}(\mathbf{m}, \mathbf{d}) = \|\mathbf{W}_d\mathbf{A}(\mathbf{m}) - \mathbf{W}_d\mathbf{d}\|^2 + \alpha\|\mathbf{W}_m\mathbf{m} - \mathbf{W}_m\mathbf{m}_{apr}\|^2. \tag{4.1}$$

The first and second parts on the right-hand side of equation (4.1) represent the misfit and the stabilizing functional, respectively. The term symbolized by $\alpha$ represents the regularization parameter. It is calculated from

$$\alpha = q\alpha_0 \frac{\|\mathbf{W}_d\mathbf{A}(\mathbf{m}) - \mathbf{W}_d\mathbf{d}\|^2}{\|\mathbf{W}_m\mathbf{m} - \mathbf{W}_m\mathbf{m}_{apr}\|^2} \tag{4.2}$$

where q is a real number greater than zero and less than 1, and $\alpha_0$ is any constant to scale the regularization parameter (Zhdanov, 2002). The term $\mathbf{m}_{apr}$ represents the *a priori* model which has any known parameters of the model. $\mathbf{W}_d$ and $\mathbf{W}_m$ represent the data and model weights, respectively. They help constrain model geometry to the correct location. The model weight is defined by the following equation (Zhdanov, 2002):

$$\mathbf{W}_m = \sqrt[4]{\mathbf{F}^*\mathbf{F}} \tag{4.3}$$

where $\mathbf{F}$ and $\mathbf{F}^*$represents the Fréchet derivative and the complex conjugate of the Fréchet derivative, which will be discussed later in this thesis. The data weight chosen will also be discussed later in this thesis. After minimizing the parametric functional the following algorithm, called the regularized conjugate gradient method, is developed:

$$\begin{aligned}
&\mathbf{r}_n = A\left(\mathbf{m}_n\right) - \mathbf{d}, \\
&\mathbf{l}_n{}^{\alpha_n} = \mathbf{l}^{\alpha_n}\left(\mathbf{m}_n\right) = \mathbf{F}_{m_n}{}^T \mathbf{W}_d{}^2 \mathbf{r}_n + \alpha_n \mathbf{W}_m{}^2 \left(\mathbf{m}_n - \mathbf{m}_{apr}\right), \\
&\beta_n{}^{\alpha_n} = \|\mathbf{l}_n{}^{\alpha_n}\|^2 / \|\mathbf{l}_{n-1}{}^{\alpha_{n-1}}\|^2, \widetilde{\mathbf{l}}_n^{\alpha_n} = \mathbf{l}_n{}^{\alpha_n} + \beta_n{}^{\alpha_n} \widetilde{\mathbf{l}}_{n-1}^{\alpha_{n-1}}, \widetilde{\mathbf{l}}_0^{\alpha_0} = \mathbf{l}_0{}^{\alpha_0}, \\
&\widetilde{k}_n^{\alpha_n} = \widetilde{\mathbf{l}}_n^{\alpha_n T} \mathbf{l}_n{}^{\alpha_n} / \left\{ \left\| \mathbf{W}_d \mathbf{F}_{m_n} \widetilde{\mathbf{l}}_n^{\alpha_n} \right\|^2 + \alpha_n \left\| \mathbf{W}_m \widetilde{\mathbf{l}}_n^{\alpha_n} \right\|^2 \right\} \\
&\mathbf{m}_{n+1} = \mathbf{m}_n - \widetilde{k}_n^{\alpha_n} \widetilde{\mathbf{l}}_n^{\alpha_n},
\end{aligned} \tag{4.4}$$

where $\mathbf{r}_n$ is the residual, $\mathbf{l}$ is the step direction of steepest ascent, $\mathbf{F}$ is the Fréchet derivative of the matrix A, and $\beta$ is the coefficient to find the conjugate direction, $\widetilde{\mathbf{l}}$ is the conjugate direction, and $\widetilde{k}$ is the conjugate step length. This is an iterative process, and the model ($\mathbf{m}$) changes every iteration to obtain a model which creates predicted data that best matches the observed data, which in turn minimizes the parametric functional (Zhdanov, 2002).

It is often necessary to keep the model parameter inside specific boundaries based on known physical boundaries of the system. In order to do this, logarithmic inversion is carried out using the following equation:

$$\tilde{\mathbf{m}} = \ln\left(\frac{\mathbf{m}_i - \mathbf{m}_i{}^-}{\mathbf{m}_i{}^+ - \mathbf{m}_i}\right) \tag{4.5}$$

where $\tilde{\mathbf{m}}$ represents the logarithmic model parameter, $\mathbf{m}_i$ represents the individual model values, $\mathbf{m}_i{}^-$ and $\mathbf{m}_i{}^+$ represent the lower and upper bounds of the inversion domain, respectively (Zhdanov, 2002).

One way to quantify how well the predicted data matches the observed data is the normalized misfit. In this thesis it is calculated by the following equation:

$$\varphi = \left( \frac{norm(\mathbf{W}_d \left( \mathbf{d}_{obs} - \mathbf{d}_{pre} \right)}{norm \left( \mathbf{W}_d \mathbf{d}_{obs} \right)} \right)^2 \tag{4.6}$$

where the norm is the L2 normalization, $\mathbf{d}_{obs}$is the observed data, and $\mathbf{d}_{pre}$is the predicted data (Zhdanov, 2002). If the misfit is equal to zero, then predicted data matches the observed data perfectly.

## 4.2 Fréchet derivative calculation of impedance tensor

The following information on the derivative of the impedance tensor can be found in Zhdanov (2009), and it is useful information for the development of the Fréchet derivative of the MT phase tensor which is only found in this thesis. The Fréchet derivative for any modeling parameter is the derivative of the forward modeling operator A with respect to the model parameter $\mathbf{m}$:

$$F = \frac{\partial A(\mathbf{m})}{\partial \mathbf{m}}. \tag{4.7}$$

To begin with, let us consider a simple case: the Fréchet derivative of the xy component of the 1D impedance:

$$Z_{xy} = \frac{E_x}{H_y}. \tag{4.8}$$

The Fréchet derivative is the following:

$$F_{Z_{xy}} = \frac{\partial Z_{xy}}{\partial \sigma} = \frac{\partial}{\partial \sigma} \frac{E_x}{H_y} = \frac{1}{H_y} \frac{\partial E_x}{\partial \sigma} - \frac{E_x}{H^2{}_y} \frac{\partial H_y}{\partial \sigma}. \tag{4.9}$$

The following definition, simplifies the above expressions:

$$F_{Q_\alpha} = \frac{\partial Q_\alpha}{\partial \sigma}. \tag{4.10}$$

where Q is E or H, and $\alpha$ is x or y. Applying the above substitution to equation (4.10) gives the following:

$$F_{Z_{xy}} = \frac{1}{H_y} F_{E_x} - \frac{E_x}{H^2{}_y} F_{H_y}. \tag{4.11}$$

Note that the Fréchet derivative of the individual electric and magnetic fields is very complex. However, the Fréchet derivative of the individual electric and magnetic fields can be simplified to the following simple equations:

$$\begin{aligned} \mathbf{F}_E(\mathbf{r}_j|\mathbf{r}) &= \widehat{\mathbf{G}}_E(\mathbf{r}_j|\mathbf{r})\,\mathbf{E}^{(n)}(\mathbf{r}), \\ \mathbf{F}_H(\mathbf{r}_j|\mathbf{r}) &= \widehat{\mathbf{G}}_H(\mathbf{r}_j|\mathbf{r})\,\mathbf{E}^{(n)}(\mathbf{r}) \end{aligned} \tag{4.12}$$

by the quasi-Born approximation (Gribenko and Zhdanov, 2007).

Using the principles above, the Fréchet derivative of the impedance components are the following:

$$F_{Z_{xy}} = \frac{dZ_{xy}}{d\sigma} = \sum_{i=1,2}\left(\frac{\partial Z_{xy}}{\partial {E_x}^{(i)}}F_{{E_x}^{(i)}} + \sum_{\alpha=x,y}\frac{\partial Z_{xy}}{\partial {H_\alpha}^{(i)}}F_{{H_\alpha}^{(i)}}\right) \tag{4.13}$$

where the partial derivatives are defined as follows:

$$\frac{\partial Z_{xy}}{\partial {E_x}^{(1)}} = \frac{{H_x}^{(2)}}{{H_y}^{(1)}{H_x}^{(2)} - {H_y}^{(2)}{H_x}^{(1)}} \tag{4.14}$$

$$\frac{\partial Z_{xy}}{\partial {H_x}^{(2)}} = \frac{{H_x}^{(1)}\left[{E_x}^{(2)}{H_y}^{(1)} - {E_x}^{(1)}{H_y}^{(2)}\right]}{\left[{H_y}^{(1)}{H_x}^{(2)} - {H_y}^{(2)}{H_x}^{(1)}\right]^2} \tag{4.15}$$

$$\frac{\partial Z_{xy}}{\partial {H_x}^{(1)}} = \frac{{H_x}^{(2)}\left[{E_x}^{(1)}{H_y}^{(2)} - {E_x}^{(2)}{H_y}^{(1)}\right]}{\left[{H_y}^{(1)}{H_x}^{(2)} - {H_y}^{(2)}{H_x}^{(1)}\right]^2} \tag{4.16}$$

$$\frac{\partial Z_{xy}}{{H_y}^{(1)}} = \frac{{H_x}^{(2)}\left[{E_x}^{(2)}{H_x}^{(1)} - {E_x}^{(1)}{H_x}^{(2)}\right]}{\left[{H_y}^{(1)}{H_x}^{(2)} - {H_y}^{(2)}{H_x}^{(1)}\right]^2} \tag{4.17}$$

$$\frac{\partial Z_{xy}}{\partial {H_y}^{(2)}} = \frac{{H_x}^{(1)}\left[{E_x}^{(1)}{H_x}^{(2)} - {E_x}^{(2)}{H_x}^{(1)}\right]}{\left[{H_y}^{(1)}{H_x}^{(2)} - {H_y}^{(2)}{H_x}^{(1)}\right]^2} \tag{4.18}$$

$$\frac{\partial Z_{xy}}{\partial {E_x}^{(2)}} = \frac{-{H_x}^{(1)}}{{H_y}^{(1)}{H_x}^{(2)} - {H_y}^{(2)}{H_x}^{(1)}}. \tag{4.19}$$

The Fréchet derivative of $Z_{yx}$ is the following:

$$F_{Z_{yx}} = \sum_{i=1,2}\left(\frac{\partial Z_{yx}}{\partial {E_y}^{(i)}}F_{{E_y}^{(i)}} + \sum_{\alpha=x,y}\frac{\partial Z_{yx}}{\partial {H_\alpha}^{(i)}}F_{{H_\alpha}^{(i)}}\right) \tag{4.20}$$

where the partial derivatives are defined as follows:

$$\frac{\partial Z_{yx}}{\partial {E_y}^{(1)}} = \frac{{H_y}^{(2)}}{{H_x}^{(1)}{H_y}^{(2)} - {H_x}^{(2)}{H_y}^{(1)}} \tag{4.21}$$

$$\frac{\partial Z_{yx}}{\partial {H_y}^{(2)}} = \frac{{H_y}^{(1)}\left[{E_y}^{(2)}{H_x}^{(1)} - {E_y}^{(1)}{H_x}^{(2)}\right]}{\left[{H_x}^{(1)}{H_y}^{(2)} - {H_x}^{(2)}{H_y}^{(1)}\right]^2} \tag{4.22}$$

$$\frac{\partial Z_{yx}}{\partial {H_y}^{(1)}} = \frac{{H_y}^{(2)}\left[{E_y}^{(1)}{H_x}^{(2)} - {E_y}^{(2)}{H_x}^{(1)}\right]}{\left[{H_x}^{(1)}{H_y}^{(2)} - {H_x}^{(2)}{H_y}^{(1)}\right]^2} \tag{4.23}$$

$$\frac{\partial Z_{yx}}{\partial {H_x}^{(1)}} = \frac{{H_y}^{(2)}\left[{E_y}^{(2)}{H_y}^{(1)} - {E_y}^{(1)}{H_y}^{(2)}\right]}{\left[{H_x}^{(1)}{H_y}^{(2)} - {H_x}^{(2)}{H_y}^{(1)}\right]^2} \tag{4.24}$$

$$\frac{\partial Z_{yx}}{\partial {H_x}^{(2)}} = \frac{{H_y}^{(1)}\left[{E_y}^{(1)}{H_y}^{(2)} - {E_y}^{(2)}{H_y}^{(1)}\right]}{\left[{H_x}^{(1)}{H_y}^{(2)} - {H_x}^{(2)}{H_y}^{(1)}\right]^2} \tag{4.25}$$

$$\frac{\partial Z_{yx}}{\partial {E_y}^{(2)}} = -\frac{{H_y}^{(1)}}{{H_x}^{(1)}{H_y}^{(2)} - {H_x}^{(2)}{H_y}^{(1)}}. \tag{4.26}$$

The Fréchet derivative of $Z_{xx}$ component is the following:

$$F_{Z_{xx}} = \sum_{i=1,2}\left(\frac{\partial Z_{xx}}{\partial {E_x}^{(i)}}F_{{E_x}^{(i)}} + \sum_{\alpha=x,y}\frac{\partial Z_{xx}}{\partial {H_\alpha}^{(i)}}F_{{H_\alpha}^{(i)}}\right) \tag{4.27}$$

where the partial derivatives are defined as follows:

$$\frac{\partial Z_{xx}}{\partial {E_x}^{(1)}} = \frac{{H_y}^{(2)}}{{H_x}^{(1)}{H_y}^{(2)} - {H_x}^{(2)}{H_y}^{(1)}} \tag{4.28}$$

$$\frac{\partial Z_{xx}}{\partial {H_y}^{(2)}} = \frac{{H_y}^{(1)}\left[{E_x}^{(2)}{H_x}^{(1)} - {E_x}^{(1)}{H_x}^{(2)}\right]}{\left[{H_x}^{(1)}{H_y}^{(2)} - {H_x}^{(2)}{H_y}^{(1)}\right]^2} \tag{4.29}$$

$$\frac{\partial Z_{xx}}{\partial {H_y}^{(1)}} = \frac{{H_y}^{(2)}\left[{E_x}^{(1)}{H_x}^{(2)} - {E_x}^{(2)}{H_x}^{(1)}\right]}{\left[{H_x}^{(1)}{H_y}^{(2)} - {H_x}^{(2)}{H_y}^{(1)}\right]^2} \tag{4.30}$$

$$\frac{\partial Z_{xx}}{\partial {H_x}^{(1)}} = \frac{{H_y}^{(2)}\left[{E_x}^{(2)}{H_y}^{(1)} - {E_x}^{(1)}{H_y}^{(2)}\right]}{\left[{H_x}^{(1)}{H_y}^{(2)} - {H_x}^{(2)}{H_y}^{(1)}\right]^2} \tag{4.31}$$

$$\frac{\partial Z_{xx}}{\partial {H_x}^{(2)}} = \frac{{H_y}^{(1)}\left[{E_x}^{(1)}{H_y}^{(2)} - {E_x}^{(2)}{H_y}^{(1)}\right]}{\left[{H_x}^{(1)}{H_y}^{(2)} - {H_x}^{(2)}{H_y}^{(1)}\right]^2} \tag{4.32}$$

$$\frac{\partial Z_{xx}}{\partial {E_x}^{(2)}} = -\frac{{H_y}^{(1)}}{{H_x}^{(1)}{H_y}^{(2)} - {H_x}^{(2)}{H_y}^{(1)}}. \tag{4.33}$$

Lastly the Fréchet derivative of $Z_{yy}$ is the following:

$$F_{Z_{yy}} = \sum_{i=1,2}\left(\frac{\partial Z_{yy}}{\partial {E_y}^{(i)}}F_{{E_y}^{(i)}} + \sum_{\alpha=x,y}\frac{\partial Z_{yy}}{\partial {H_\alpha}^{(i)}}F_{{H_\alpha}^{(i)}}\right) \tag{4.34}$$

where the partial derivatives are defined as follows:

$$\frac{\partial Z_{yy}}{\partial {E_y}^{(1)}} = \frac{{H_x}^{(2)}}{{H_y}^{(1)}{H_x}^{(2)} - {H_y}^{(2)}{H_x}^{(2)}} \tag{4.35}$$

$$\frac{\partial Z_{yy}}{\partial {H_x}^{(2)}} = \frac{{H_x}^{(1)}\left[{E_y}^{(2)}{H_y}^{(1)} - {E_y}^{(1)}{H_y}^{(2)}\right]}{\left[{H_y}^{(1)}{H_x}^{(2)} - {H_y}^{(2)}{H_x}^{(2)}\right]^2} \tag{4.36}$$

$$\frac{\partial Z_{yy}}{\partial {H_x}^{(1)}} = \frac{{H_x}^{(2)}\left[{E_y}^{(1)}{H_y}^{(2)} - {E_y}^{(2)}{H_y}^{(1)}\right]}{\left[{H_y}^{(1)}{H_x}^{(2)} - {H_y}^{(2)}{H_x}^{(2)}\right]^2} \tag{4.37}$$

$$\frac{\partial Z_{yy}}{\partial {H_y}^{(1)}} = \frac{{H_x}^{(2)}\left[{E_y}^{(2)}{H_x}^{(1)} - {E_y}^{(1)}{H_x}^{(2)}\right]}{\left[{H_y}^{(1)}{H_x}^{(2)} - {H_y}^{(2)}{H_x}^{(2)}\right]^2} \tag{4.38}$$

$$\frac{\partial Z_{yy}}{\partial {H_y}^{(2)}} = \frac{{H_x}^{(1)}\left[{E_y}^{(1)}{H_x}^{(2)} - {E_y}^{(2)}{H_x}^{(1)}\right]}{\left[{H_y}^{(1)}{H_x}^{(2)} - {H_y}^{(2)}{H_x}^{(2)}\right]^2} \tag{4.39}$$

$$\frac{\partial Z_{yy}}{\partial {E_y}^{(2)}} = -\frac{{H_x}^{(1)}}{{H_y}^{(1)}{H_x}^{(2)} - {H_y}^{(2)}{H_x}^{(2)}}. \tag{4.40}$$

This completes the Fréchet derivative calculation of the impedance tensor.

## 4.3 Fréchet derivative calculation of phase tensor

Using the same reasoning as above, the Fréchet derivative for the phase tensor is as follows:

$$F_{\Phi_{xx}} = \sum_{j=x,y}\left(\sum_{i=x,y}\frac{\partial \Phi_{ij}}{\partial X_{ij}}F_{X_{ij}} + \frac{\partial \Phi_{jx}}{\partial Y_{jx}}F_{Y_{jx}}\right) \tag{4.41}$$

where the partial derivatives are defined as follows:

$$\frac{\partial \Phi_{xx}}{\partial X_{xx}} = \frac{X_{yy}\left[X_{xy}Y_{yx} - X_{yy}Y_{xx}\right]}{\det\left(X\right)^2} \tag{4.42}$$

$$\frac{\partial \Phi_{xx}}{\partial X_{yy}} = \frac{X_{xy}\left[Y_{yx}X_{xx} - Y_{xx}X_{yx}\right]}{\det\left(X\right)^2} \tag{4.43}$$

$$\frac{\partial \Phi}{\partial X_{xy}} = \frac{X_{yy}\left(X_{yx}Y_{xx} - Y_{yx}X_{xx}\right)}{\det\left(X\right)^2} \tag{4.44}$$

$$\frac{\partial \Phi_{xx}}{\partial X_{yx}} = \frac{X_{xy}\left[X_{yy}Y_{xx} - X_{xy}Y_{yx}\right]}{\det\left(X\right)^2} \tag{4.45}$$

$$\frac{\partial \Phi}{\partial Y_{xx}} = \frac{X_{yy}}{\det\left(X\right)} \tag{4.46}$$

$$\frac{\partial \Phi}{\partial Y_{yx}} = -\frac{X_{xy}}{\det\left(X\right)}. \tag{4.47}$$

Now the Fréchet of $\Phi_{yy}$

$$F_{\Phi_{yy}} = \sum_{j=x,y}\left(\sum_{i=x,y}\frac{\partial \Phi_{yy}}{\partial X_{ij}}F_{X_{ij}} + \frac{\partial \Phi_{yy}}{\partial Y_{jy}}F_{Y_{jy}}\right) \tag{4.48}$$

where the partial derivatives are defined as follows:

$$\frac{\partial \Phi_{yy}}{\partial X_{xx}} = \frac{X_{yx}\left[X_{yy}Y_{xy} - X_{xy}Y_{yy}\right]}{\det\left(X\right)^2} \tag{4.49}$$

$$\frac{\partial \Phi_{yy}}{\partial X_{yy}} = \frac{X_{xx}\left[X_{yx}Y_{xy} - X_{xx}Y_{yy}\right]}{\det\left(X\right)^2} \tag{4.50}$$

$$\frac{\partial \Phi_{yy}}{\partial X_{xy}} = \frac{X_{yx}\left[X_{xx}Y_{yy} - X_{yx}Y_{xy}\right]}{\det\left(X\right)^2} \tag{4.51}$$

$$\frac{\partial \Phi_{yy}}{\partial X_{yx}} = \frac{X_{xx}\left[X_{xy}Y_{yy} - X_{yy}Y_{xy}\right]}{\det\left(X\right)^2} \tag{4.52}$$

$$\frac{\partial \Phi_{yy}}{\partial Y_{xy}} = -\frac{X_{yx}}{\det\left(X\right)} \tag{4.53}$$

$$\frac{\partial \Phi_{yy}}{\partial Y_{yy}} = \frac{X_{xx}}{\det\left(X\right)}. \tag{4.54}$$

Next, the off diagonal components starting with $\Phi_{xy}$:

$$F_{\Phi_{xy}} = \sum_{j=x,y}\left(\sum_{i=x,y}\frac{\partial \Phi_{xy}}{\partial X_{ij}}F_{X_{ij}} + \frac{\partial \Phi_{xy}}{\partial Y_{jy}}F_{Y_{jy}}\right) \tag{4.55}$$

with the partial derivatives are defined in the following way:

$$\frac{\partial \Phi_{xy}}{\partial X_{xx}} = \frac{X_{yy}\left[X_{xy}Y_{yy} - X_{yy}Y_{xy}\right]}{\det\left(X\right)^2} \tag{4.56}$$

$$\frac{\partial \Phi_{xy}}{\partial X_{yy}} = \frac{X_{xy}\left(X_{xx}Y_{yy} - X_{yx}Y_{xy}\right)}{\det\left(X\right)^2} \tag{4.57}$$

$$\frac{\partial \Phi_{xy}}{\partial X_{xy}} = \frac{X_{yy}\left[X_{yx}Y_{xy} - X_{xx}Y_{yy}\right]}{\det\left(X\right)^2} \tag{4.58}$$

$$\frac{\partial \Phi_{xy}}{\partial X_{yx}} = \frac{X_{xy}\left[X_{yy}Y_{xy} - X_{xy}Y_{yy}\right]}{\det\left(X\right)^2} \tag{4.59}$$

$$\frac{\partial \Phi_{xy}}{\partial Y_{xy}} = \frac{X_{yy}}{\det\left(X\right)} \tag{4.60}$$

$$\frac{\partial \Phi_{xy}}{\partial Y_{yy}} = \frac{-X_{xy}}{\det\left(X\right)}. \tag{4.61}$$

Lastly $\Phi_{yx}$

$$F_{\Phi_{yx}} = \sum_{j=x,y}\left(\sum_{i=x,y}\frac{\partial \Phi_{yx}}{\partial X_{ij}}F_{X_{ij}} + \frac{\partial \Phi_{yx}}{\partial Y_{jx}}F_{Y_{jx}}\right). \tag{4.62}$$

With the partial derivatives defined as follows:

$$\frac{\partial \Phi_{yx}}{\partial X_{xx}} = \frac{X_{yx}\left[X_{yy}Y_{xx} - X_{yx}Y_{yx}\right]}{\det\left(X\right)^2} \tag{4.63}$$

$$\frac{\partial \Phi_{yx}}{\partial X_{yy}} = \frac{X_{xx}\left[X_{yx}Y_{xx} - X_{xx}Y_{yx}\right]}{\det\left(X\right)^2} \tag{4.64}$$

$$\frac{\partial \Phi_{yx}}{\partial X_{xy}} = \frac{X_{yx}\left[X_{xx}Y_{yx} - X_{yx}Y_{xx}\right]}{\det\left(X\right)^2} \tag{4.65}$$

$$\frac{\partial \Phi_{yx}}{\partial X_{yx}} = \frac{X_{xx}\left(X_{xy}Y_{yx} - X_{yy}Y_{xx}\right)}{\det\left(X\right)^2} \tag{4.66}$$

$$\frac{\partial \Phi_{yx}}{\partial Y_{yx}} = \frac{X_{xx}}{\det\left(X\right)} \tag{4.67}$$

$$\frac{\partial \Phi_{yx}}{\partial Y_{xx}} = \frac{-X_{yx}}{\det\left(X\right)}. \tag{4.68}$$

In summary, using a quasi-Born approximation the Fréchet derivative has been calculated for both the impedance and phase tensors.

# CHAPTER 5

# INVERSION OF SYNTHETIC MT DATA

In the first few chapters of this thesis, the background and mathematical theory for impedance and phase tensor inversion associated with the MT method have been presented. In this chapter, the ideas will be tested by modeling with synthetic data. There are three necessary requirements for an inversion algorithm to work properly. First, the parametric functional must continuously decrease; second, the predicted data must match the observed data; and third, the model must resemble what is expected from the geology of the subsurface. If the algorithm can do these three things with a synthetic model, then these criteria provided a good indicator that the algorithm might make geologically meaningful models of the subsurface using real data. The next step is to use collected geophysical data, and if the above requirements are met then there is a good chance that a useful model has been produced.

In this chapter, three different inversion models will be presented: model one is an L-shaped body, model two is model one with NSI added, and model three is the same as model two except sparse NSI are used (there are only NSI under the receivers). All three models were inverted using only the principal components of the impedance and phase tensors, and all components of the impedance and phase tensors. Random noise was also added to model one, and inverted using both the impedance and phase tensors. Some results from the full impedance and full phase tensor inversion will be presented.

## 5.1 Inversion of MT impedance tensor

First model one will be presented, which is an L-shaped conductive body in a homogenous resistive background material. Figure 5.1 is a 3D view of the L-shaped body, without the background conductivity shown, with the receivers on top represented by dots. Figure 5.2 is a 2D horizontal view of the same L-shaped body

with the background resistivity displayed. There are 81 receivers, spaced 1 km apart, located at the surface which spans from 250 m to 8250 m in the x and y directions. The resistivity of the anomalous L-shaped body is 10 Ω-m with a background homogenous half-space of 1000 Ω-m. The body is 300 m thick, located 1500 m to 1800 m below the surface. The leg in the y direction is 1 km by 5 km, and 6 km by 1 km in the x direction. This body was chosen to represent the geology of the McArthur River, and to see how well the impedance and phase tensor methods recovered the L-shaped known body.

After the synthetic model was created, forward modeling was done using the integral equation method, described in section 3.1, (PIE3D parallel integral equation 3D was used a code developed by CEMI), which generated synthetic electric and magnetic fields. These fields were converted to the components of the impedance tensor, $Z_{xy}$, $Z_{yx}$, $Z_{xx}$, and $Z_{yy}$, using equations (3.11) and (3.12). There were eight frequencies used that were logarithmically spaced from 0.1 to 20 Hz. The forward modeling generated observed data for the impedance tensor as shown in Figures 5.3 and 5.4 using one frequency (20 Hz). Figure 5.3 displays a 2D interpolated contour map of the real and imaginary parts of $Z_{xy}$ and $Z_{yx}$ components, respectively. Notice that the real and imaginary parts of the $Z_{xy}$ and $Z_{yx}$ component are greater and less than zero, respectively. The $Z_{xy}$ component is caused by currents flowing in the x direction which are observed by the $E_x$ term within the equation to calculate $Z_{xy}$. The $Z_{yx}$ component is caused by currents flowing in the y direction which is observed by the $E_y$ component within the equation to calculate $Z_{yx}$ component. The L-shaped body is resolved in the x direction for the $Z_{xy}$ component with impedance values that are less than the background. It is also clearly shown in the y direction for the $Z_{yx}$ component with absolute impedance values that are less than the background. Figure 5.4 displays the real and imaginary parts of the $Z_{xx}$ and $Z_{yy}$ components, respectively. Notice that all the components can be positive or negative, and they are smaller than the principal, $Z_{xy}$ and $Z_{yx}$, components in magnitude by at least a factor of 10. One other thing to observe is that the L-shaped body cannot be observed from any of the auxiliary components $Z_{xx}$ or $Z_{yy}$.

The impedance data increase as the frequency increases, and this phenomena is

independent of the physical parameters of the Earth. In order to make the values comparable, they are separated into their individual components $Z_{xy}$, $Z_{yx}$, $Z_{xx}$, or $Z_{yy}$, and multiplied by the inverse of the residual for this component. This is called data weighting by the component and frequency (Zhdanov, 2002).

The synthetic data set described above was initially inverted using only the principal components of the impedance tensor ($Z_{xy}$ and $Z_{yx}$). The cells in the x and y directions were 250 m, and 100 m in the z direction. The inversion domain was -750 m to 9750 m, -500 m to 9500 m, and 100 m to 40100 m in the x, y, and z directions, respectively. The total length, width and height were 10500 m, 10000 m, and 4000 m in the x, y, and z directions, respectively. There were a total of 42x40x40 or 67200 cells. The regularization parameter ($\alpha$) was selected using equation (4.2); and q were set to 0.01 and 0.5, respectively, because they caused the parametric function to continuously decrease. The *a priori* model ($\mathbf{m}_{apr}$) was set to zero to see how well the synthetic model would be recovered without it. The background resistivity was set to 1000 Ω-m homogenous half-space in the inversion, which is the same as the background resistivity in the forward modeling. The upper and lower limits of resistivity used in equation (4.5) were 10,000 Ω-m and 10 Ω-m, respectively, so that the inversion did not produce unreasonable resistivity values. The model weight ($\mathbf{W}_m$) equation (4.3), was recalculated starting at the fifth iteration, and recalculated every five iterations until the forty-fifth iteration. This was done because the Fréchet derivative is changing every iteration. The inversion was run for 50 iterations using the L2 minimum norm stabilizer, at which time it was terminated. The final normalized misfit, from equation (4.6), was $7.7 \times 10^{-3}\%$. This was done because the inverted model looked reasonable, and the normalized misfit was very low.

As was discussed in the introduction of this section, there are three things that need to be true for any inversion to work "properly." The parametric functional must continuously decrease, the predicted data must match the observed data, and the model must reasonably match the expected geology. Figure 5.5 A shows the normalized misfit, and Figure 5.5 B shows the parametric functional, both are respect to iteration number. Notice that both figures decrease every iteration. The observed and predicted data are shown with a frequency of 20 Hz in Figures 5.6 - 5.7. The

figures on the left-hand side represent the observed data, and the figures on right-hand side represent the predicted data. Notice that the colorbar limits are set to the same values. From this figure one can see that the observed and predicted data have very similar values. If the misfit value was zero then the observed and predicted data would be exactly the same. The normalized misfit is close to zero, $7.7 \times 10^{-3}\%$, which indicates that the observed and predicted data are very close to one another. A horizontal and vertical slice at z = 1600 m and y = 2000 m, of the inversion results are shown in Figure 5.8. The slices correspond to inversion results through approximately the center of the body in the horizontal direction, and through the leg in the x direction of the L-shaped body in the vertical direction. The black L-shaped lines and rectangle represent the location of the true body. The body was recovered well in the x and y directions, but there is smearing in the z direction, because MT is a diffusive method. The resistivity is greater than 100 Ω-m while the true body's resistivity is 10 Ω-m. Thus principal impedance inversion has a parametric functional that continuously decreases, the predicted data matches the observed data, and the inversion model matches the original model in the x and y directions. These three results from inversion indicate that the inversion algorithm works when using the principal impedance, and it can be used for real MT data.

The principal impedance inversion worked; next, the full impedance tensor was inverted. The input parameters were exactly the same for forward modeling and inversion as the principal impedance. The only difference was the input data was the full impedance instead of the principal impedance. The inversion was run for 50 iterations then stopped with a normalized misfit of $1.7 \times 10^{-2}\%$. Note that the misfit from one method is not comparable to another method as was found by comparing misfit of different synthetic models. The observed and predicted data for the $Z_{xx}$ and $Z_{yy}$ components are shown in the Figures 5.9 - 5.10, respectively. The observed and predicted data from the principal components ($Z_{xy}$ and $Z_{yx}$) were not included, but they look very similar to the principal impedance observed and predicted data (Figures 5.6- 5.7). Notice that the colorbars have the same limits and the predicted data on the right-hand side have very similar values as the observed data on the left-hand side. The final normalized misfit, $1.7 \times 10^{-2}\%$, demonstrates that the

observed and predicted data were very close match. The parametric functional also continuously decreased. Figure 5.11 shows the inversion results of the full impedance inversion. There is a horizontal slice near the center of the body at z = 1600 m, and a vertical slice passing through the leg in the x direction at y = 2000 m as shown in Figures 5.11 A and B, respectively. The figures show that the inversion recovered the L-shaped body really well in the x and y directions. Once again there is smearing in the z direction due to the fact that MT is a diffusive method. The full impedance inversion recovered a resistivity that is close to 10 Ω-m which is very close to the true value. These results indicate that when all the components from full impedance tensor are used, the inversion recovers the body better than the principal-component impedance inversion.

## 5.2 Inversion of MT phase tensor

In the last section, it was made evident that the MT impedance method with all components worked well to invert the anomalous L-shaped body with low resistivity. In this section, the inversion results of the MT phase tensor will be shown. The first step was to take the impedance data set, that was obtained from forward modeling the L-shaped body of Figure 5.1, and convert it to a phase tensor data set using equation (3.16). The Fréchet derivative has also been converted to the phase tensor form. The inversion used all the same input parameters as for the impedance inversion. The data set was then inverted first using the principal components of the phase tensor ($\Phi_{xx}$ and $\Phi_{yy}$). The inversion was run for 50 iterations with a final normalized misfit of $3.4 \times 10^{-3}$%. The inversion results are shown in Figure 5.12 with a horizontal and vertical slice at z = 1600 m and y = 2000 m, respectively. The horizontal slice of the inversion results show that the principal phase tensor inversion does not recover the body in exactly the right location. Once again there is smearing in the z direction due to the fact that MT is a diffusive method. The resistivity of the anomaly is greater than 100 Ω-m and the true body had 10 Ω-m. The predicted data matches the observed data, and the parametric functional continually decreases. The three inversion indicators show that the principal phase tensor inversion works for synthetic data.

Next all the components of the phase tensor were inverted. The input parameters were exactly the same as the previous inversion settings. The only difference was the input data was changed to full phase tensor instead of principal phase tensor. The inversion was run for 50 iterations, and it came to a normalized misfit of $4.5 \times 10^{-3}\%$. Figure 5.13 shows the inversion results of the full phase tensor with horizontal and vertical slices passing through about the middle of the L-shaped body at z = 1600 m, and one of the legs at y = 2000 m. The inversion results have a very similar shape to the L-shaped body in the horizontal direction. There is smearing in the z direction once again because the MT method is a diffusive method. The resistivity of the full phase tensor inversion results are greater than 10 Ω-m, and are very close to the original body. The full phase tensor results are much better than the principal phase tensor results, because the location and resistivity matches the original body better. These results indicate that the full phase tensor is an effective means of inverting anomalous conductive bodies.

From the four synthetic modeling experiments of the above section, it can be concluded that the impedance and phase tensor methods both recover the L-shaped body very well when using all the components of the impedance and phase tensors, respectively. When only the principal components are used, the impedance and phase tensor methods work fairly well.

## 5.3 Inversion of synthetic MT data with NSI

Once it was confirmed that the impedance and phase tensor methods were able to recover the L-shaped synthetic model, NSI were added to test the method's ability to recover the L-shaped body with NSI. The phase tensor method promises to remove those effects, theoretically, in equation (2.11). Two different models are presented that added NSI to model one. Model two (as shown in Figure 5.14) has random cells with resistivity values that range from 10 to 1000 Ω-m everywhere there were receivers. These cells were 10 m thick and they were centered 6m below the surface. Figure 5.15 shows a 2D view of the NSI of model two. Figure 5.16 shows the synthetic observed impedance data of model two at 20 Hz. Notice that the L-shaped body cannot be distinguished at all in these maps. Model three has sparse NSI as shown in

Figure 5.17. The NSI are nearly identical as in model two, the only difference is there are only NSI under the receiver locations. Figure 5.18 shows a 2D plane view of the NSI, with the background conductivity also displayed, and the receivers represented by the black dots. Figure 5.19 shows the synthetic observed impedance data at 20 Hz from model three. Notice that the NSI have distorted the results so that the L-shaped body cannot be distinguished.

The apparent resistivity (equation 2.7) and phase were plotted with respect to the square root of period, and they were compared using these three models (as shown in Figure 5.20). The figures clearly show that the apparent resistivity has been shifted to lower values when NSI are present, but the phase is much less affected by the NSI especially with longer periods (lower frequencies). These are the phenomena which are described as static shift.

The phase tensor data set was also plotted with respect to the square root of period, and compared using the three models (as shown in Figure 5.21). The phase tensor values do not remove the effects of NSI completely, but the scale is very small, and for the most part the phase tensor does remove the effects due to NSI.

The impedance tensor was inverted using the synthetic data from model three. All of the input parameters for principal impedance inversion were exactly the same as those from model one. The inversion was run for 50 iterations at which time it reached a normalized misfit of $1.68 \times 10^{-2}\%$. The NSI added $9.1 \times 10^{-3}\%$ noise to the normalized misfit. A horizontal and vertical slice at z = 1600 m and y = 2000 m, of the inversion results are shown in Figure 5.22. The slices correspond to inversion results through approximately the center of the body in the horizontal direction, and through the leg in the x direction of the L-shaped body in the vertical direction. The body was recovered well in the x and y directions, but there is more smearing than in the same inversion results without noise (Figure 5.8). There is smearing in the z direction, because MT is a diffusion method. There is also smearing above the anomaly because of the added synthetic NSI. The resistivity is greater than 100 Ω-m while the true body's resistivity is 10 Ω-m. This shows that with the added noise, the inversion using principal impedance tensor still recovers the synthetic anomalous body.

The full impedance tensor was also inverted, using the data from model three. The input parameters were once again exactly the same as those from model one. The only difference with the inversion was the input data was changed to full impedance synthetic data from model three. The inversion was run for 50 iterations at which time it reached a normalized misfit of 0.14%. This represents an increase in normalized misfit value from the inversion with no noise, model 1, of 0.12%. The full impedance inversion results, using the data from model three, are displayed in Figure 5.23. Once again there is a horizontal slice at z = 1600 m, and a vertical slice at y = 2000 m. If the two different full impedance inversion results, that is synthetic data from model 3 (Figure 5.23) are compared with full impedance inversion results from model 1 (Figure 5.11), then this comparison shows that the L-shaped body is recovered in the same location in the horizontal direction. In the vertical direction there are some effects from the NSI, however, the full impedance tensor method still recovers the true body very well.

The principal components of the phase tensor were also inverted using the synthetic data from model three. The input parameters are exactly the same as model one, the only difference is the input data was changed to principal phase tensor data from model three. The inversion was run for 50 iterations, at which time it reached a normalized misfit of $3.4 \times 10^{-3}$%. There is no misfit increase from model one. The inversion results are displayed in Figure 5.24. Once again there is a horizontal slice at z = 1600 m, and a vertical slice at y = 2000 m. Comparing these inversion results with those using the principal phase tensor and synthetic data from model one (Figure 5.12), shows that they are very similar. The horizontal slice shows that the anomaly from model three has a higher resistivity, and the full L-shaped body is less distinguishable. The vertical slice also shows that the inversion results from model three are also more resistive.

All the components from the phase tensor were also inverted using the synthetic data from model three. The input parameters are exactly the same as model one; however, the input data was changed to all the components of the phase tensor method from model three. The inversion was run for 50 iterations, at which time it reached a normalized misfit of $5.2 \times 10^{-3}$%. There is an increase in normalized misfit

of $7 \times 10^{-2}\%$. The inversion results are displayed in Figure 5.25. Once again there is a horizontal slice at z = 1600 m, and a horizontal slice at y = 2000 m. Comparing the same inversion methods, full phase tensor, with different input synthetic data model one (Figure 5.13) and model three (Figure 5.25), visually the results look very similar. These results show that the phase tensor is able to remove the effects due to NSI, the full phase tensor results recover the true model much better than the principal components of the phase tensor.

In summary, both the impedance and phase tensors are capable of recovering the L-shaped body when NSI are added. Both methods work better when all the components are used versus simply the principal components. Looking at the inversion results, using the synthetic data from model three, it appears that the full phase tensor (Figure 5.25) produced the best results. However, comparing the results from model three inversion of the phase tensor with the impedance tensor shows that the phase tensor is only a slight improvement.

## 5.4 Effects of noise added to synthetic MT data

In the previous parts of this thesis it was demonstrated that the phase tensor removes noise caused by NSI. The phase tensor is only capable of removing effects due to static shift which distorts the electric field. However, there are other types of noise that affect the principal and auxiliary components of the impedance tensor. The amplitude of the principal components is much larger than the auxiliary components, and the auxiliary components are much more affected by distortions (Chave and Jones 2012). This idea was tested with synthetic modeling, and was confirmed to be correct in this case. Five percent random noise was added to the observed electric and magnetic fields. Next, the components of the impedance and phase tensor were calculated and inverted. Figure 5.26 is the observed and predicted data of the full impedance tensor with respect to the square root of period from model 1 with no noise added. Notice that the predicted data almost perfectly match the observed data. All the figures (5.26 - 5.29) have the same receiver located at rx = 4250 m and ry = 8250 m. Figure 5.27 is the observed and predicted data from model one with added noise described above. Notice that the principal components of the impedance tensor ($Z_{xy}$

and $Z_{yx}$) are unaffected by the added noise. However, the auxiliary components ($Z_{xx}$ and $Z_{yy}$) are slightly affected by the added noise. Figure 5.28 is the observed and predicted data of the phase tensor with respect to the square root of frequency with synthetic data from model one. Notice that the predicted data matches the observed data almost perfectly. Figure 5.29 is the observed and predicted data of the phase tensor with respect to the square root of period from model one with added noise. Notice how every component of the phase tensor is affected by the added noise. This is because the phase tensor (equation 3.16) is calculated by multiplication and division of the principal components and the auxiliary components together. The principal components become distorted by the noise of the auxiliary components, and the final outcome is distorted data. This implies that the phase tensor might have problems when inverting real data because all real data are affected by noise.

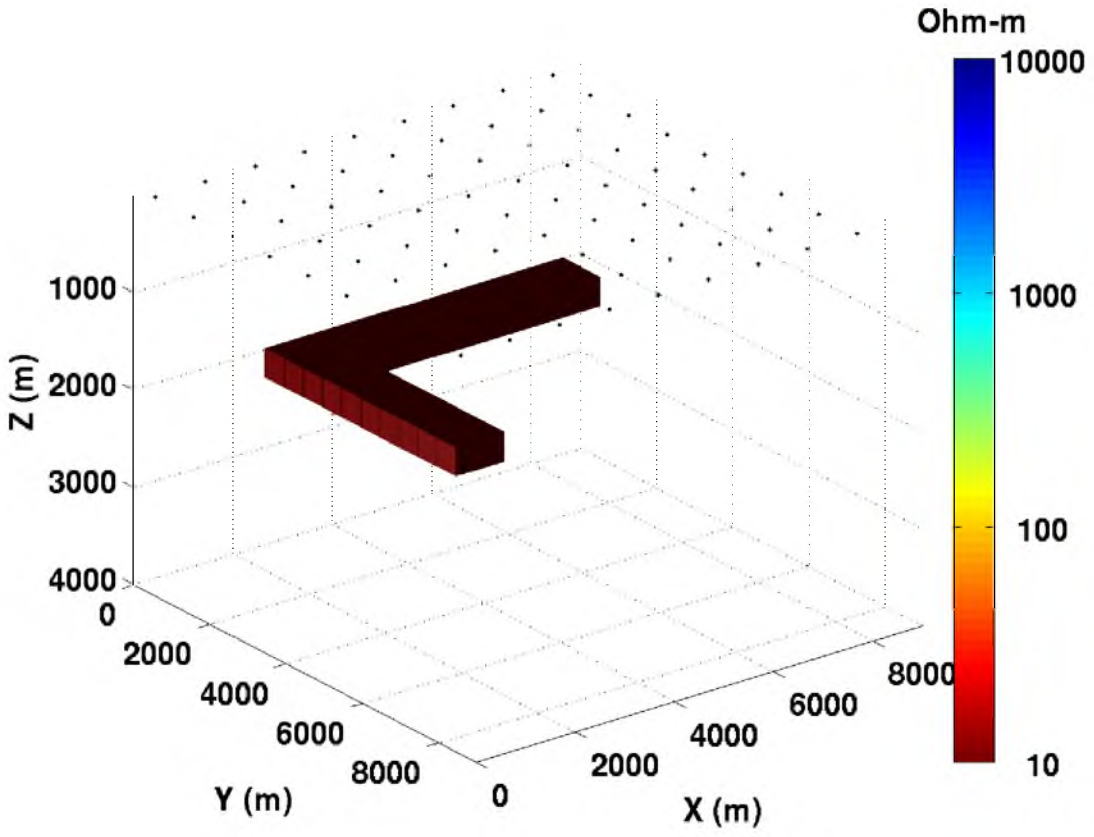


**Figure 5.1**. 3D view of inversion model, L-shaped body, located 1500-1800m below the surface. The legs are 1 km by 6 km in the x direction, and 1 km by 5 km in the y direction. There are 81 receivers represented by the dots. The body has a resistivity of 10 Ω-m, and the background resistivity (not shown) is 1000 Ω-m.

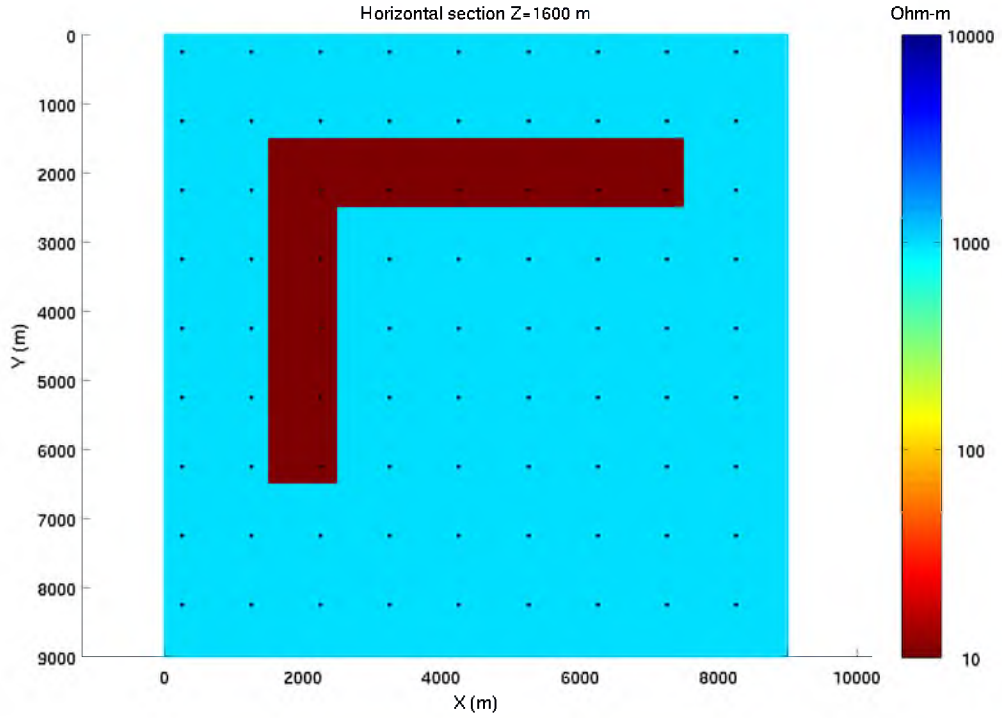


**Figure 5.2**. 2D view of the L-shaped body as shown in Figure 5.1. The legs are 1 km by 6 km in the x direction, and 1 km by 5 km in the y direction. The resistivity of the L-shaped body is 10 Ω-m. The background resistivity of 1000 Ω-m is shown having the light blue color. There are 81 receivers, represented by the black dots.

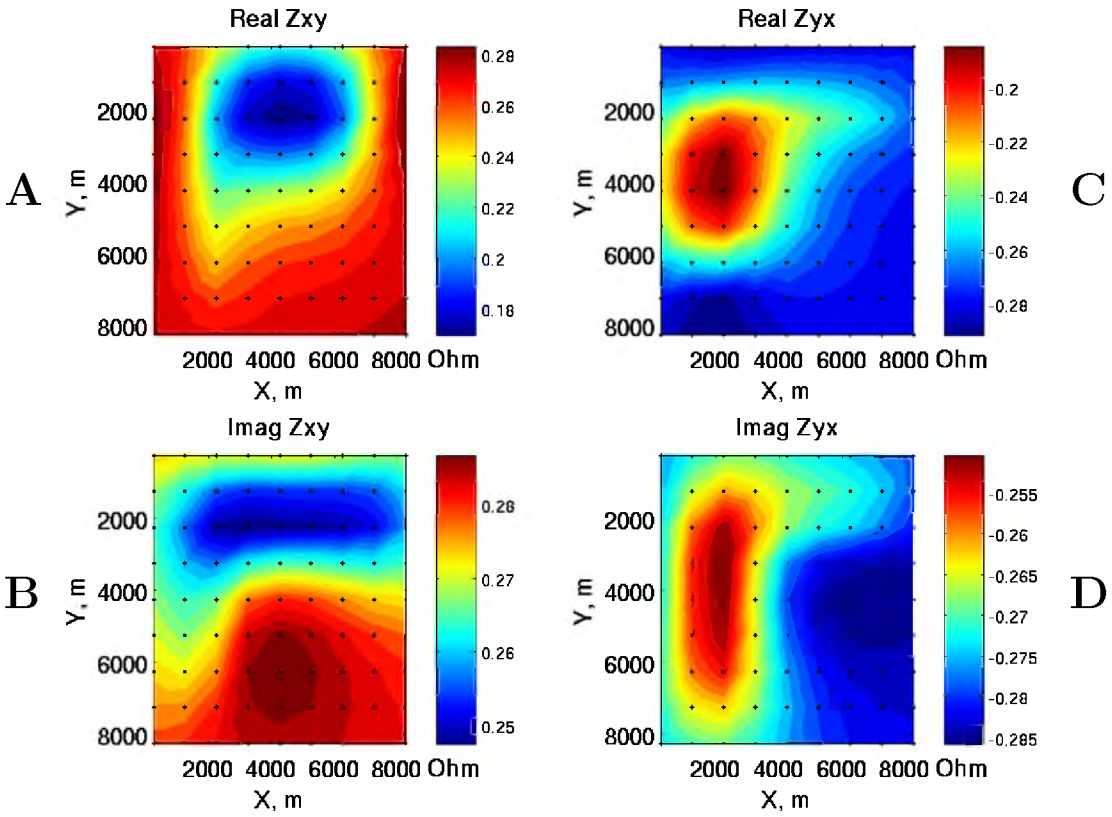


**Figure 5.3**. Observed auxiliary components synthetic data from the L-shaped body in Figure 5.1. A) and B) represent the xy components and C) and D) the yx components of the impedance tensor, respectively. A) and C) represent the real parts. B) and D) represent the imaginary parts. Data computed at 20 Hz. The black dots represent the receivers spaced 1 km apart.

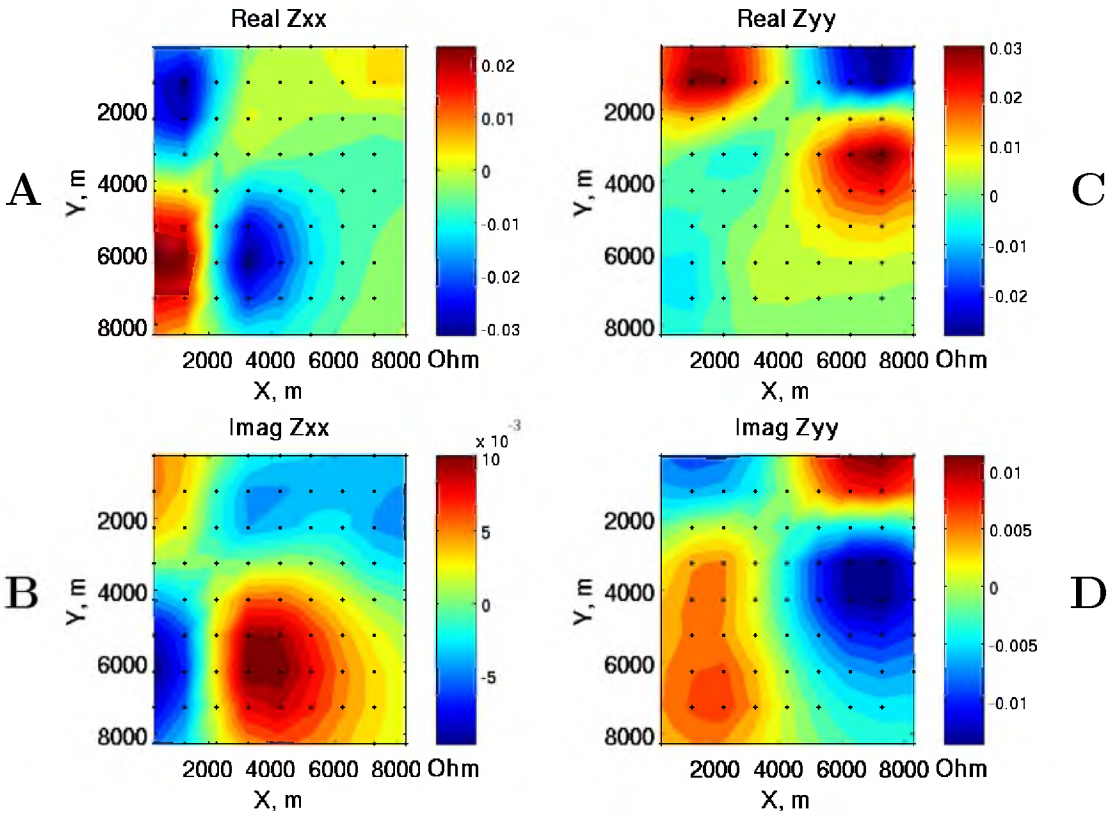


**Figure 5.4**. Observed auxiliary components synthetic data from the L-shaped body in Figure 5.1. A) and B) represent the xx components and C) and D) the yy components of the impedance tensor, respectively. A) and C) represent the real parts. B) and D) represent the imaginary parts. Data computed at 20 Hz. The black dots represent the receivers spaced 1 km apart.

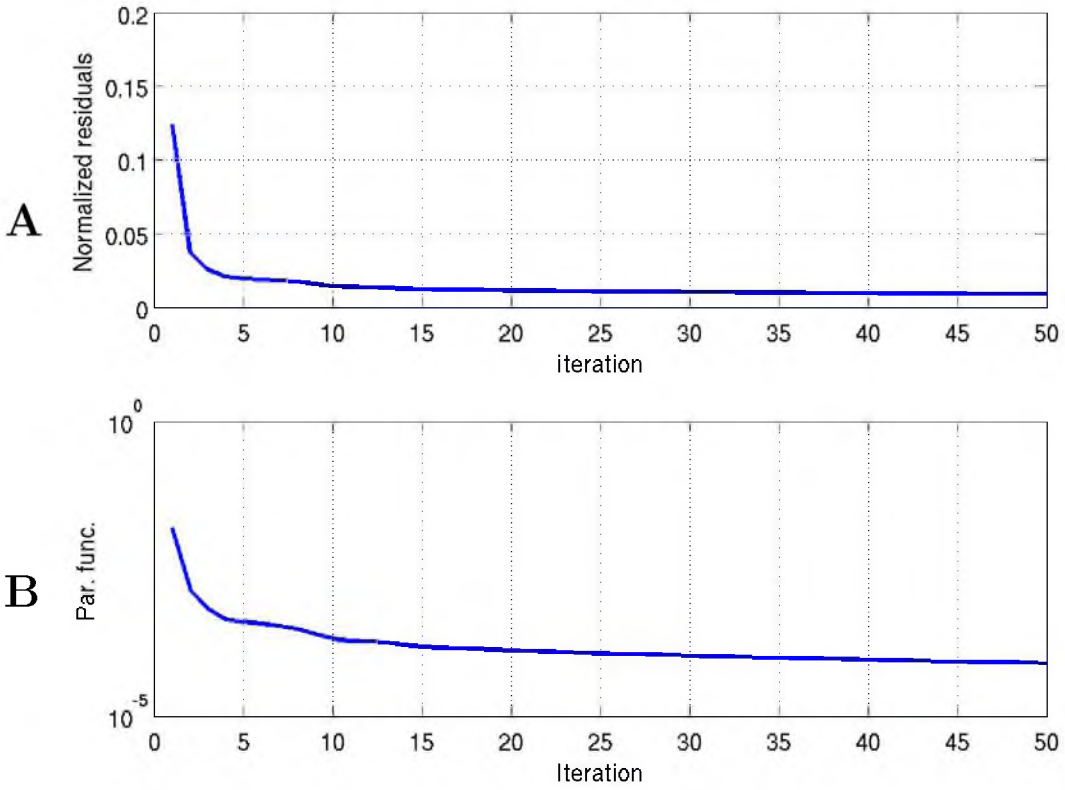


**Figure 5.5**. The parametric functional must continuously decrease in order for an inversion algorithm to work properly. The misfit functional should also be as small as possible. A) shows normalized misfit, and B) shows the parametric functional. Both A) and B) are with respect to iteration number. Notice that the parametric and misfit functionals continuously decrease.

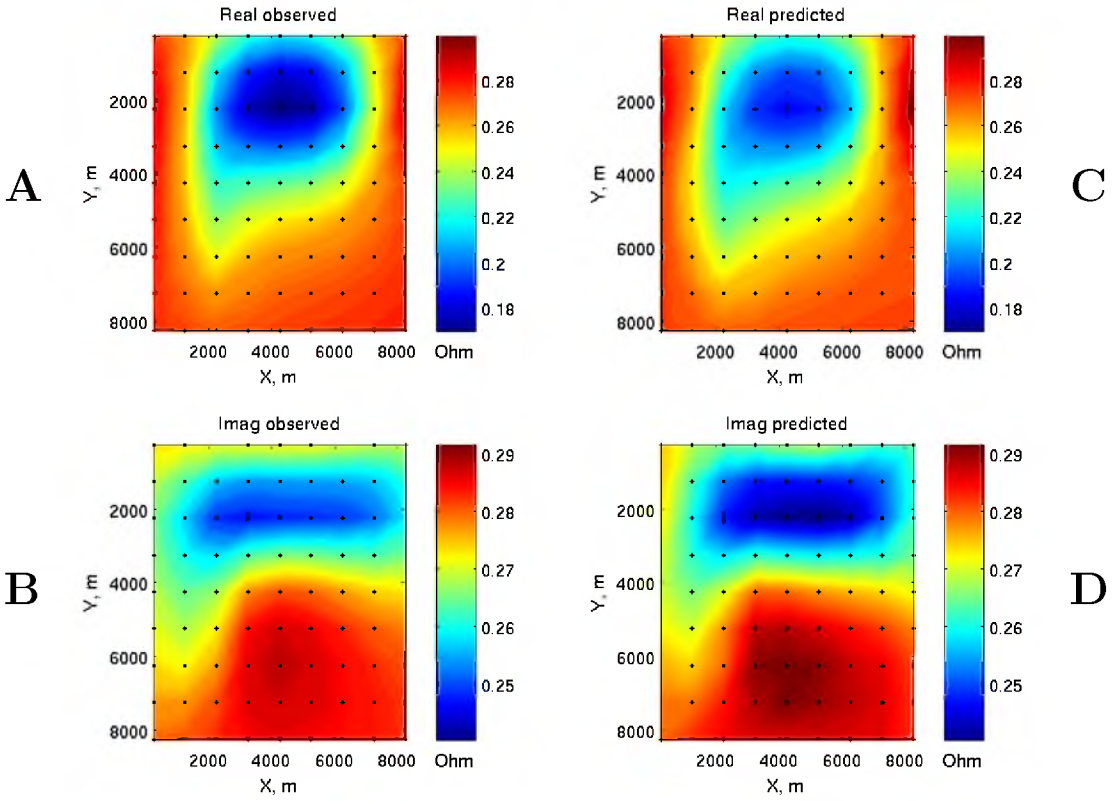


**Figure 5.6**. Observed and predicted maps of $Z_{xy}$ at 20 Hz for the L-shaped synthetic model from the principal impedance inversion. A) shows the real parts and C) the imaginary parts of the observed data. B) shows the real and D) the imaginary parts of the predicted data. The black dots represent the receivers spaced 1 km apart. Notice that the predicted data are a close match to the observed data.

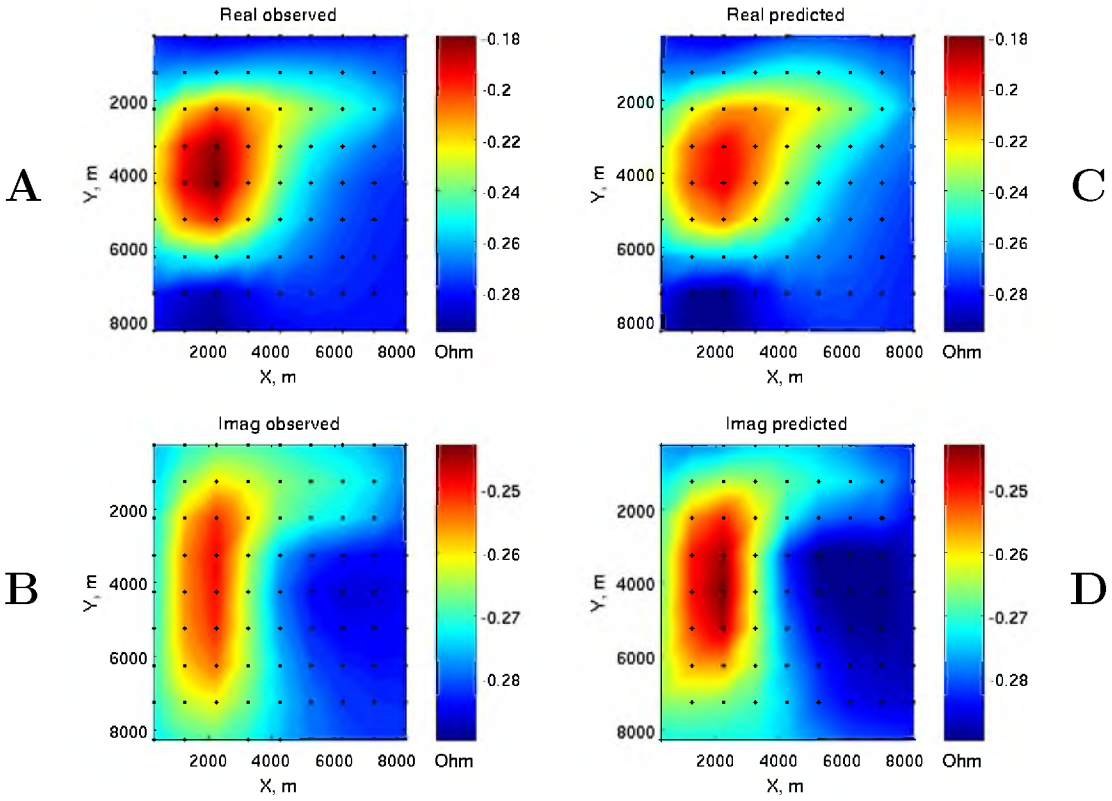


**Figure 5.7**. Observed and predicted maps of $Z_{yx}$ at 20 Hz for the L-shaped synthetic model from the principal impedance inversion. A) shows the real parts and C) the imaginary parts of the observed data. B) shows the real and D) the imaginary parts of the predicted data. The black dots represent the receivers spaced 1 km apart. Notice that the predicted data are a close match to the observed data.

A

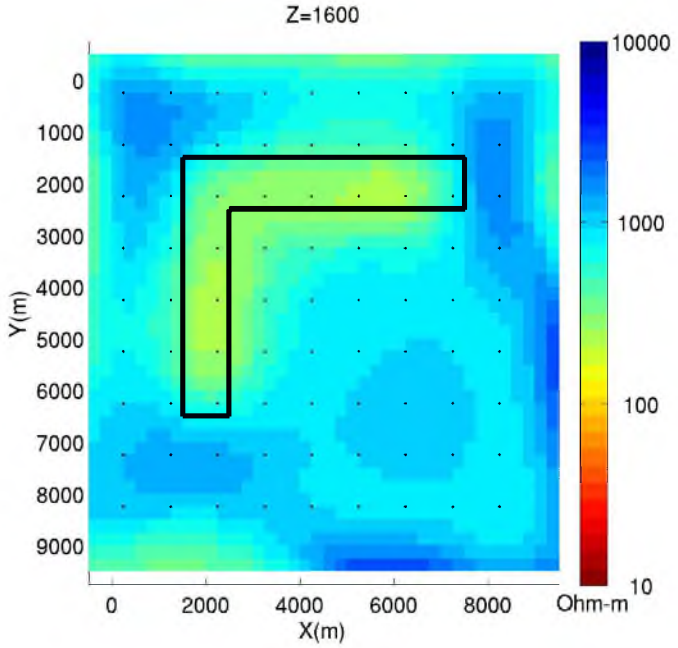


B

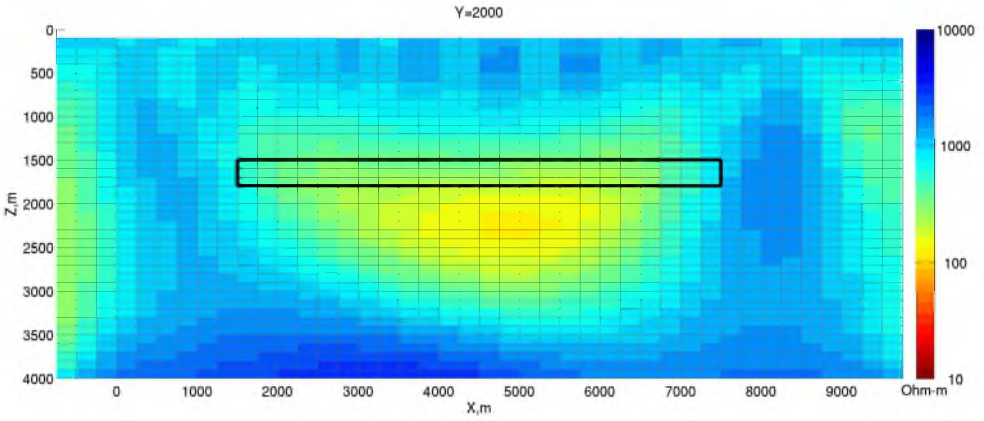


**Figure 5.8**. A horizontal and vertical slice of the inversion results of the L-shaped body, as shown in Figure 5.1, located at A) Z=1600 m and B) Y = 2000 m . The synthetic data came from the principal components of the impedance tensor ($Z_{xy}$ and $Z_{yx}$). The black L-shaped lines and rectangle represent the location of the true body in the horizontal and vertical direction, respectively. The recovered body has an average resistivity greater than 100 Ω-m, while the true body was 10 Ω-m. The inverted body matches the original L-shaped body in the horizontal view, but it is smeared in the Z direction. This is because MT is a diffusive method. The dots '.' on the horizontal slice represent the location of the receivers.

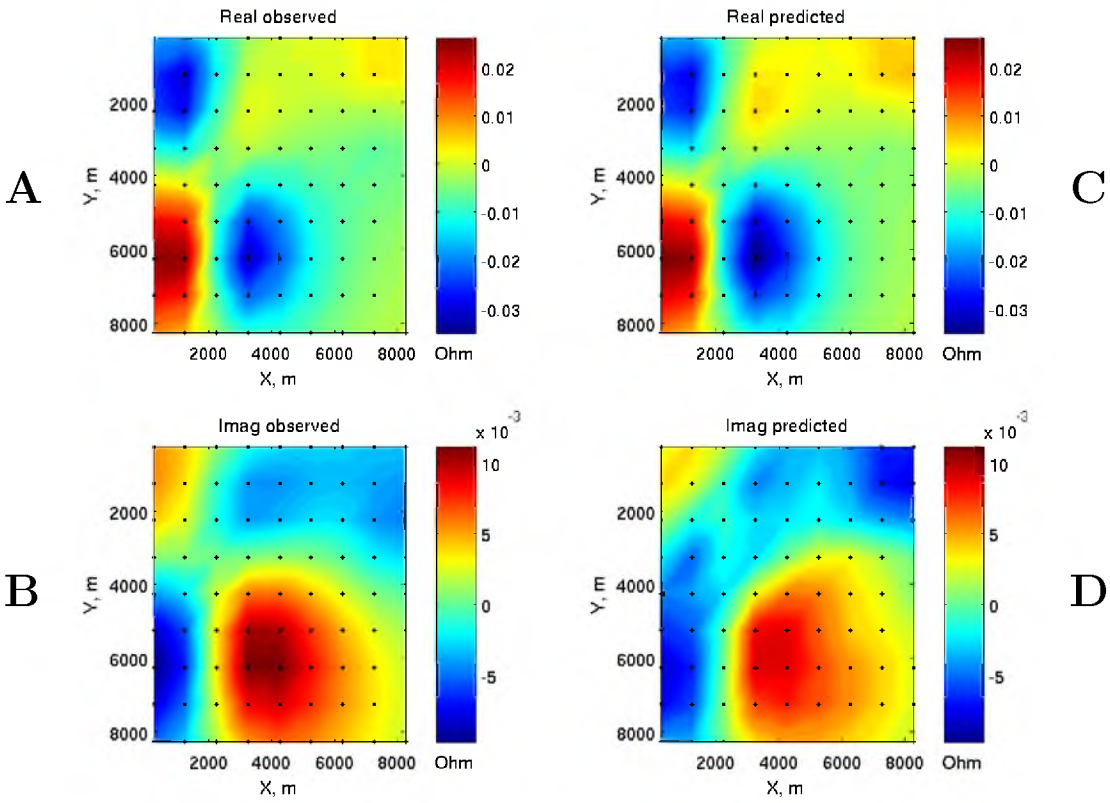


**Figure 5.9**. Observed and predicted maps of $Z_{xx}$ at 20 Hz for the L-shaped synthetic model from the principal impedance inversion. A) shows the real parts and C) the imaginary parts of the observed data. B) shows the real and D) the imaginary parts of the predicted data. The black dots represent the receivers spaced 1 km apart. Notice that the predicted data are a close match to the observed data.

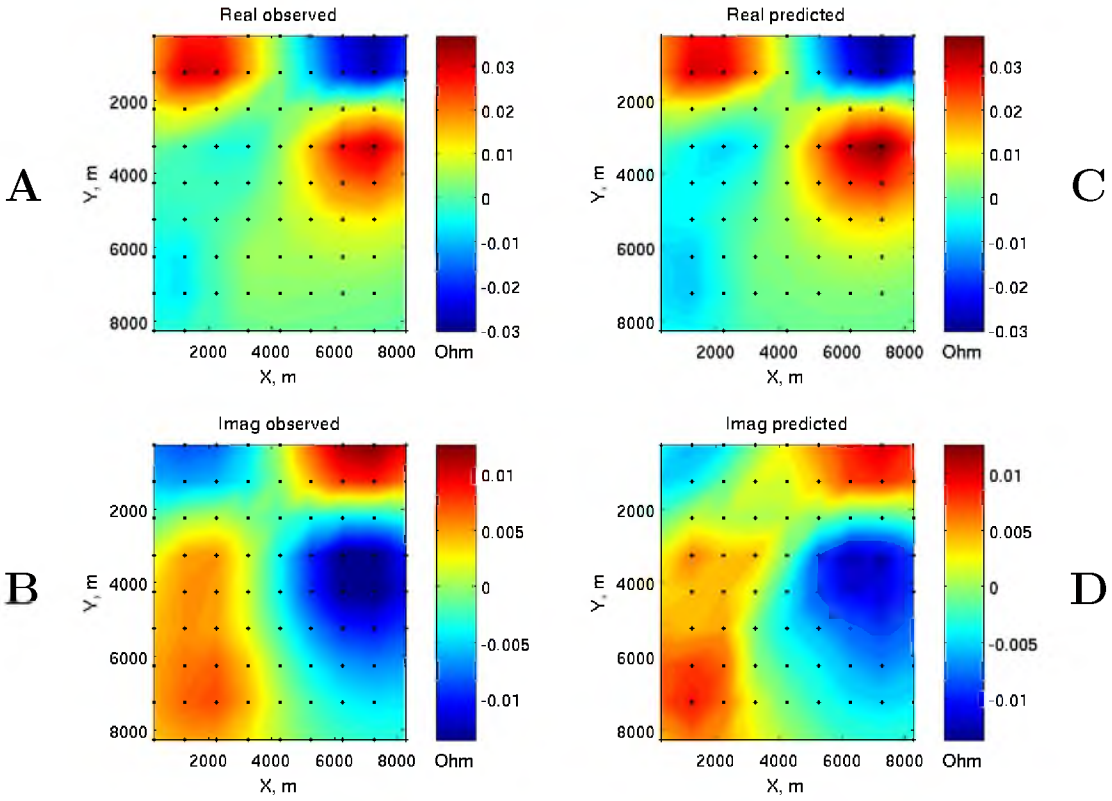


**Figure 5.10**. Observed and predicted maps of $Z_{yy}$ at 20 Hz for the L-shaped synthetic model from the principal impedance inversion. A) shows the real parts and C) the imaginary parts of the observed data. B) shows the real and D) the imaginary parts of the predicted data. The black dots represent the receivers spaced 1 km apart. Notice that the predicted data are a close match to the observed data.

A

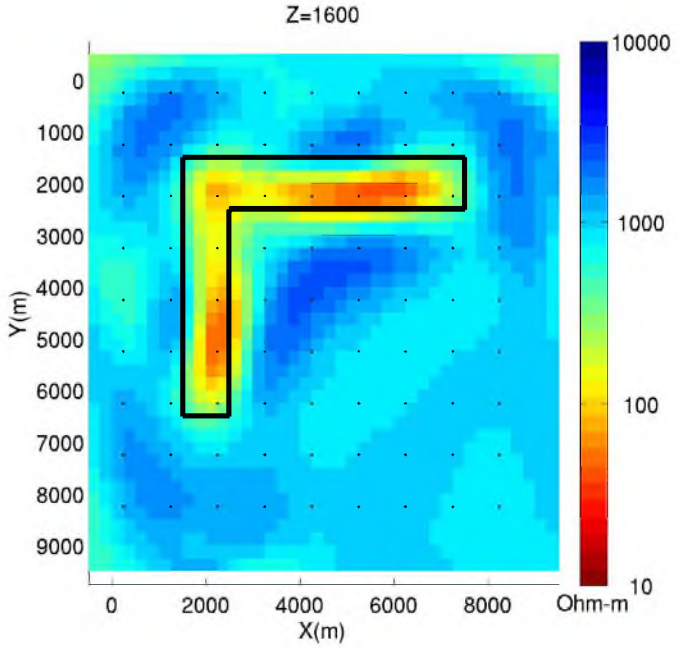


B

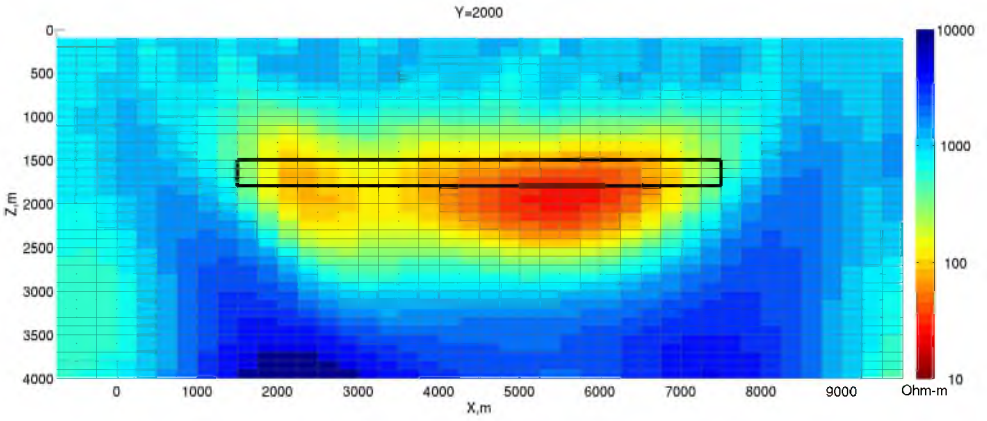


**Figure 5.11**. A horizontal and vertical slice of the inversion results of the L-shaped body, as shown in Figure 5.1, located at A) Z=1600 m and B) Y = 2000 m. The synthetic data came from all the components of the impedance tensor ($Z_{xy}$, $Z_{yx}$, $Z_{xx}$, and $Z_{yy}$). The black L-shaped lines and rectangle represent the location of the true body in the horizontal and vertical direction, respectively. The recovered body has an average resistivity greater than 10 Ω-m, while the true body was 10 Ω-m. The inverted body matches the original L-shaped body in the horizontal view, but it is smeared in the Z direction. This is because MT is a diffusive method. The dots '.' on the horizontal slice represent the locations of the receivers.

A

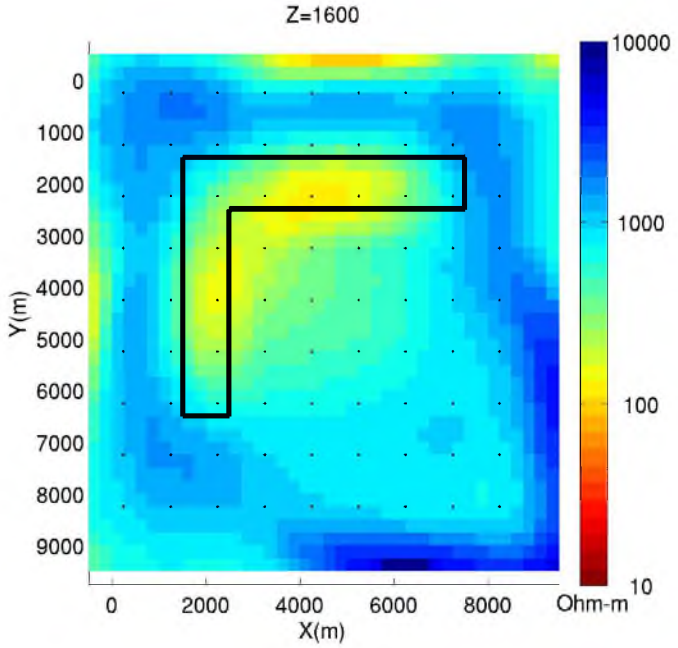


B

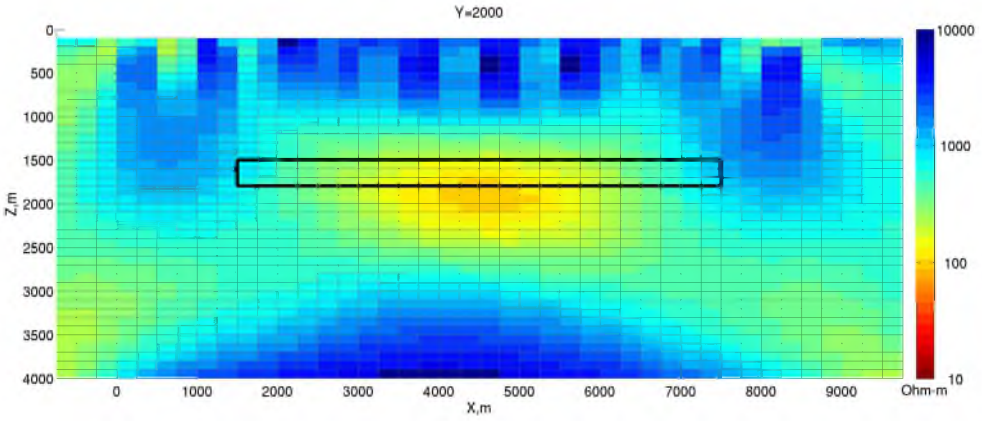


**Figure 5.12**. A horizontal and vertical slice of the inversion results of the L-shaped body, as shown in Figure 5.1, located at A) Z=1600 m and B) Y = 2000 m. The synthetic data came from the principal components of the phase tensor ($\Phi_{xx}$, and $\Phi_{yy}$). The black L-shaped lines and rectangle represent the location of the true body in the horizontal and vertical direction, respectively. The recovered body has an average resistivity greater than 100 Ω-m, while the true body was 10 Ω-m. The inverted body matches the original L-shaped body, in most locations, in the horizontal view, but it is smeared in the Z direction. This is because MT is a diffusive method. The dots '.' on the horizontal slice represent the location of the receivers.

A

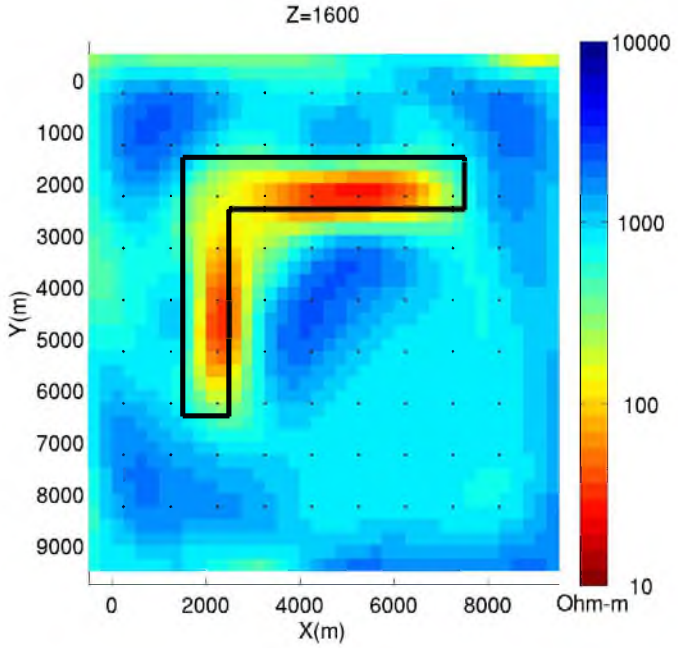


B

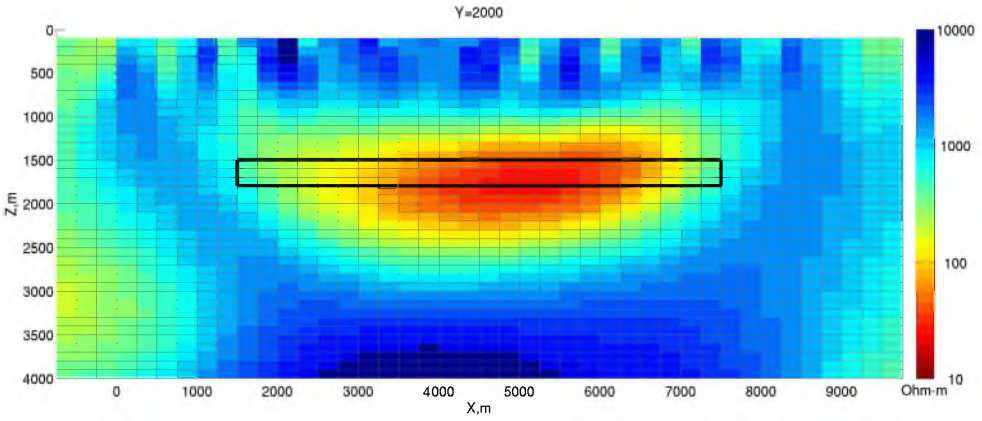


**Figure 5.13**. A horizontal and vertical slice of the inversion results of the L-shaped body, as shown in Figure 5.1, located at A) Z=1600 m and B) Y = 2000 m. The synthetic data came from all the components of the phase tensor ($\Phi_{xy}$,$\Phi_{yx}$,$\Phi_{xx}$, and $\Phi_{yy}$). The black L-shaped lines and rectangle represent the location of the true body in the horizontal and vertical direction, respectively. The recovered body has an average resistivity greater than 10 Ω-m, while the true body was 10 Ω-m. The inverted body matches the original L-shaped body in the horizontal view, but it is smeared in the Z direction. This is because MT is a diffusive method. The dots '.' on the horizontal slice represent the location of the receivers.

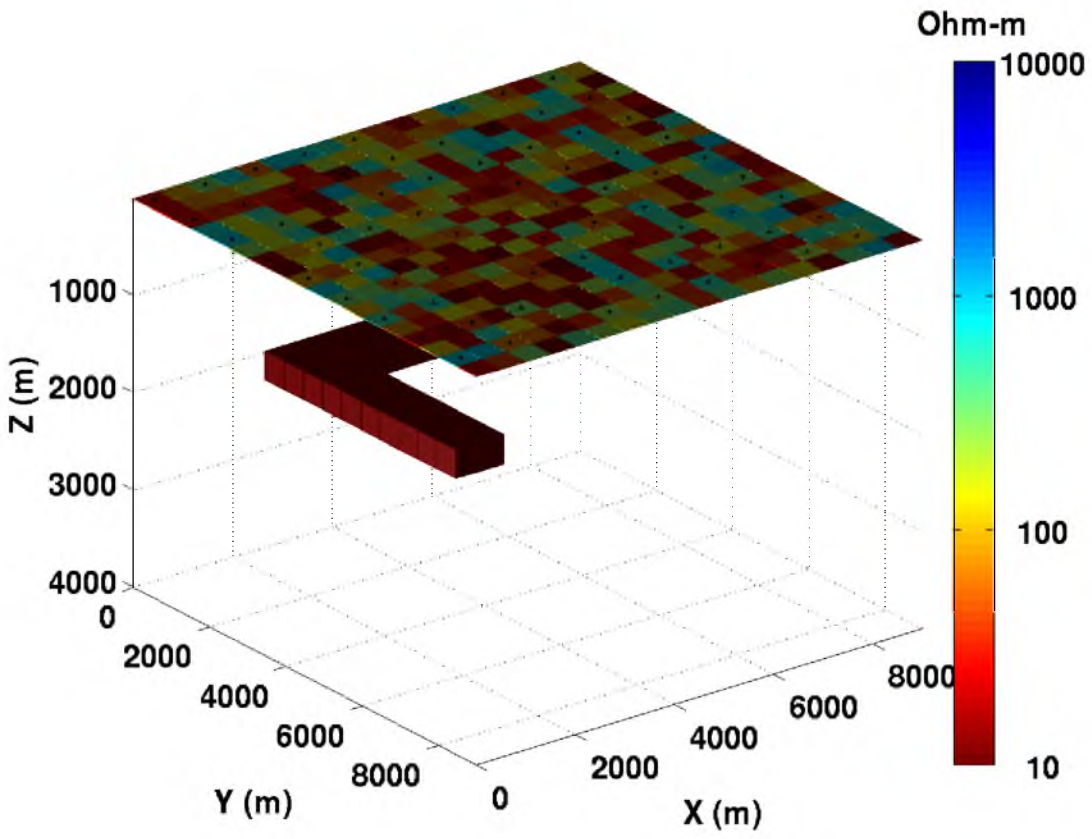


**Figure 5.14**. 3D view of synthetic NSI over the L-shaped body with 10 Ω-m resistivity as shown in Figure 5.1. They are randomly generated and have resistivity values that range from 10 to 1000 Ω-m. The black dots represent the 81 receivers spaced 1 km apart.

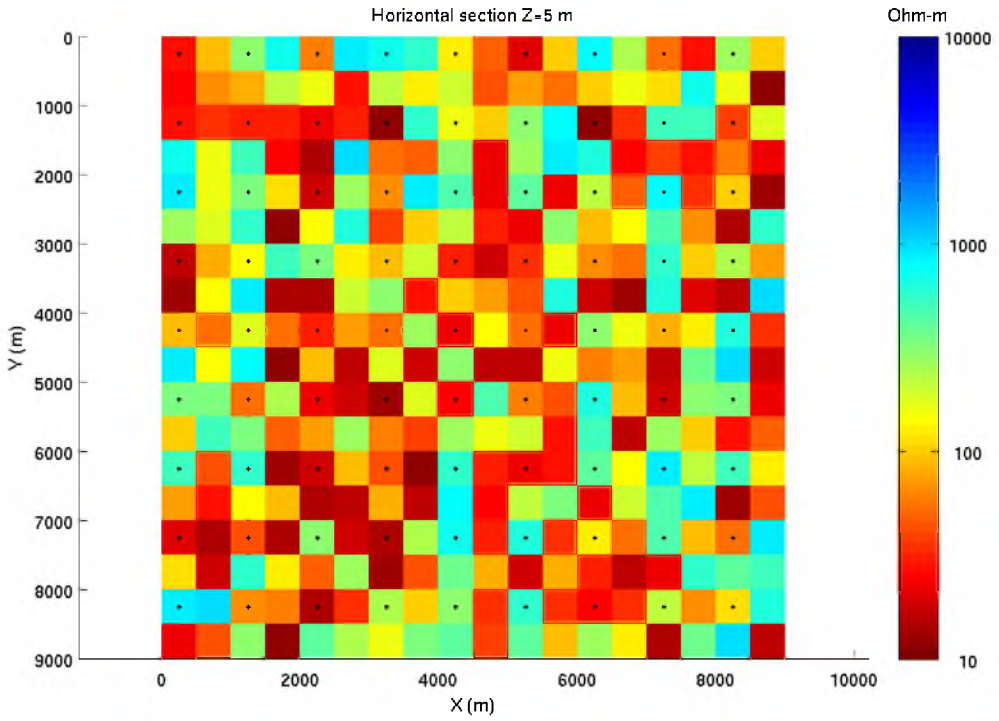


**Figure 5.15**. 2D view of the randomly generated NSI that range in values from 10-1000 Ω-m as shown in Figure 5.14 (the L-shaped body is buried below the NSI). The black dots represent the 81 receivers spaced 1 km apart.

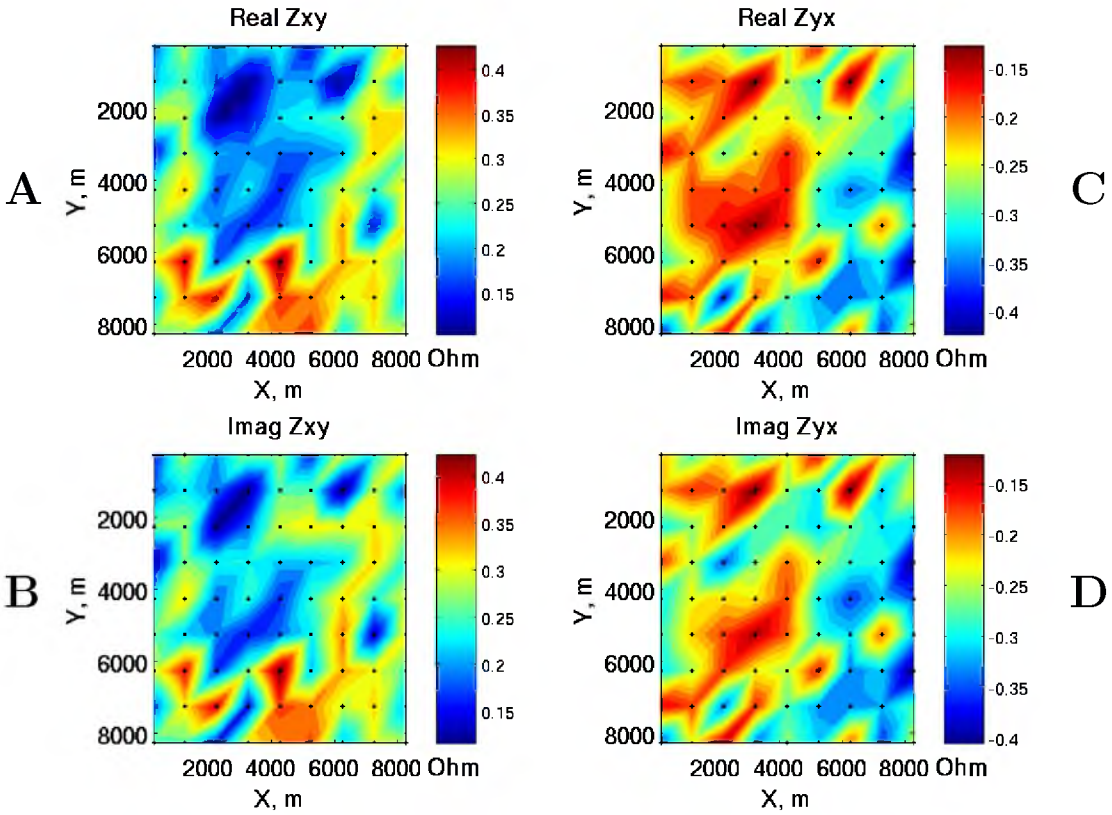


**Figure 5.16**. Observed synthetic data from the L-shaped body with NSI as shown in Figure 5.14. A) and B) represent the xy components and C) and D) the yx components of the impedance tensor, respectively. A) and C) represent the real parts. B) and D) represent the imaginary parts. Data computed at 20 Hz. The black dots represent the receivers spaced 1 km apart. Notice that the NSI make it impossible to distinguish the L-shaped body.

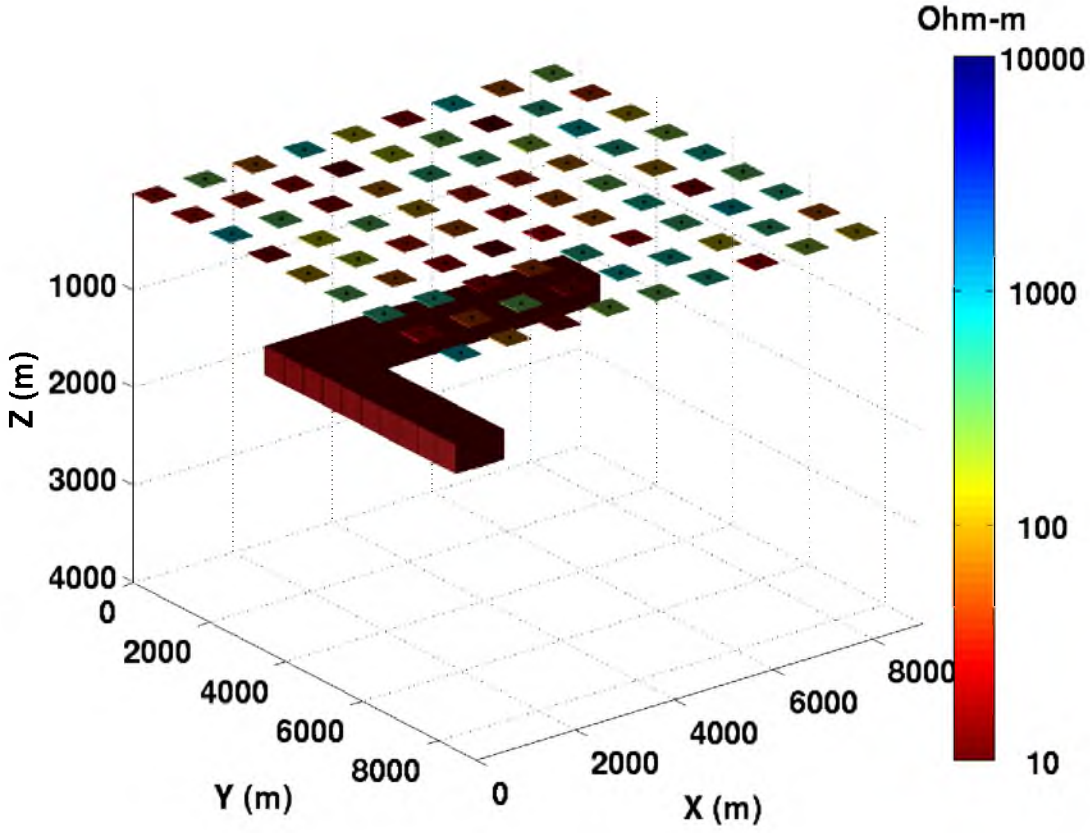


**Figure 5.17**. 3D view of synthetic sparse NSI over the L-shaped body as shown in Figure 5.1. They are randomly generated and have resistivity values that range from 10 Ω-m to 1000 Ω-m. The black dots represent the 81 receivers spaced 1 km apart.

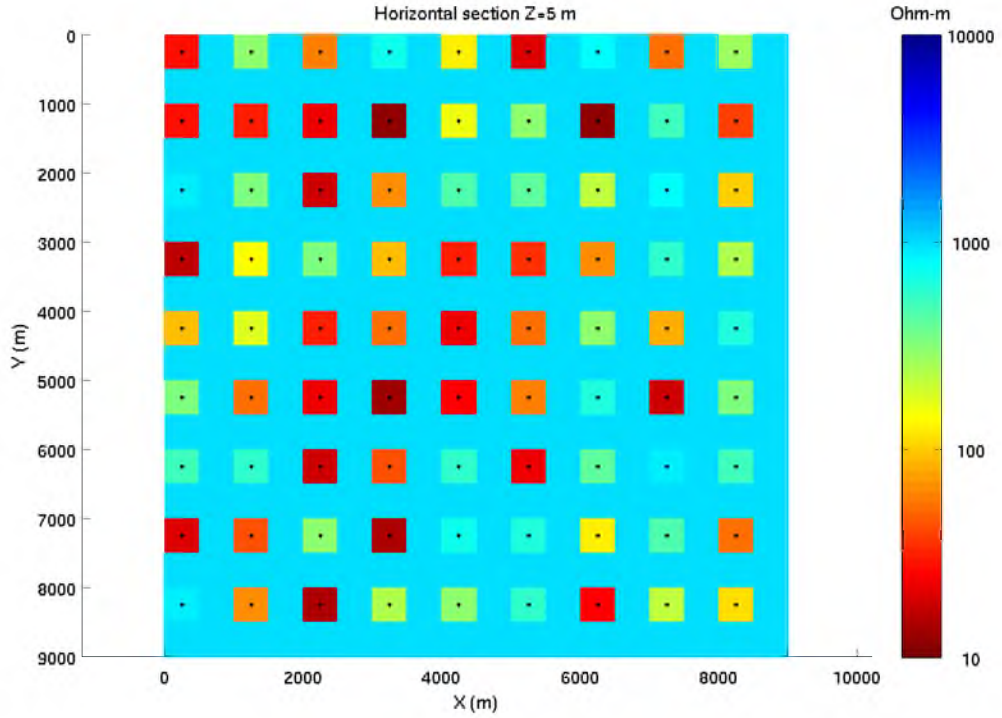


**Figure 5.18**. 2D plane view of the sparse NSI with background conductivity of 1000 Ω-m as shown in Figure 5.17. The anomalies have randomly distributed resistivity values from 10-1000 Ω-m. There are 81 receivers represented by the black dots spaced 1 km apart.

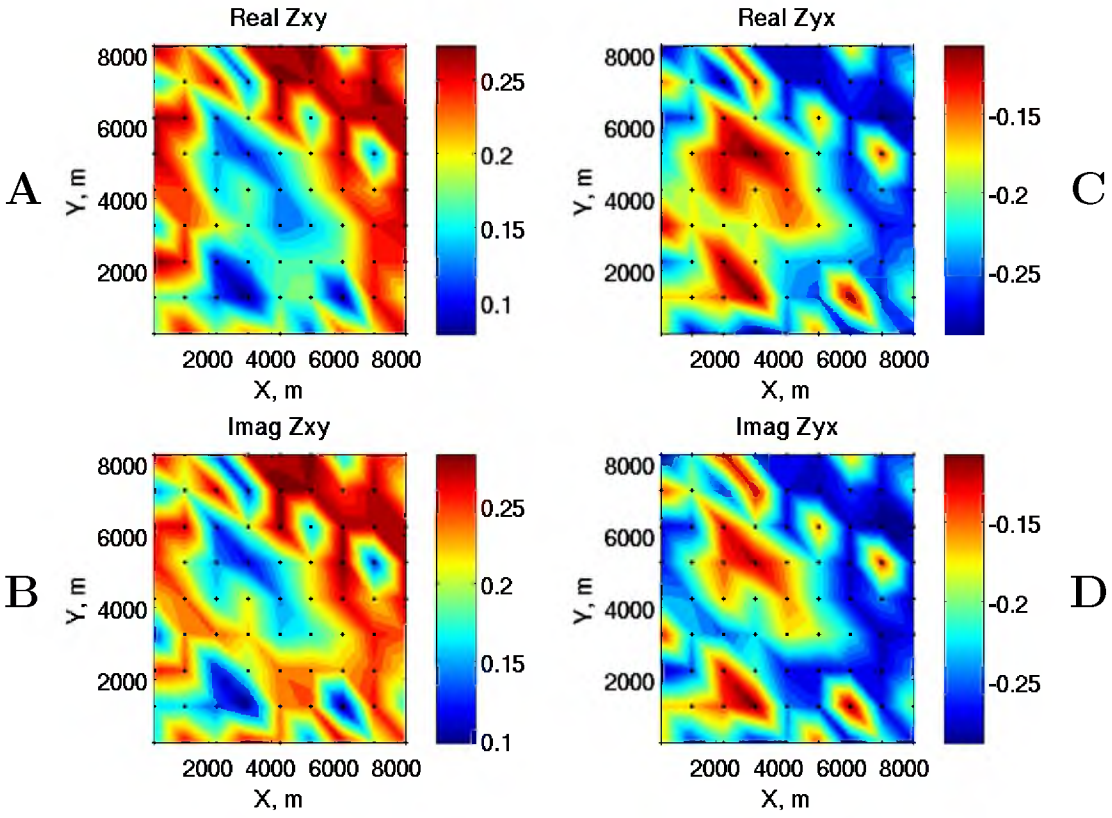


**Figure 5.19**. Observed synthetic data from the L-shaped body with sparse NSI as shown in Figure 5.17. A) and B) represent the xy components and C) and D) the yx components of the impedance tensor, respectively. A) and C) represent the real parts. B) and D) represent the imaginary parts. Data computed at 20 Hz. The black dots represent the receivers spaced 1 km apart. Notice that the NSI make it impossible to distinguish the L-shaped body.

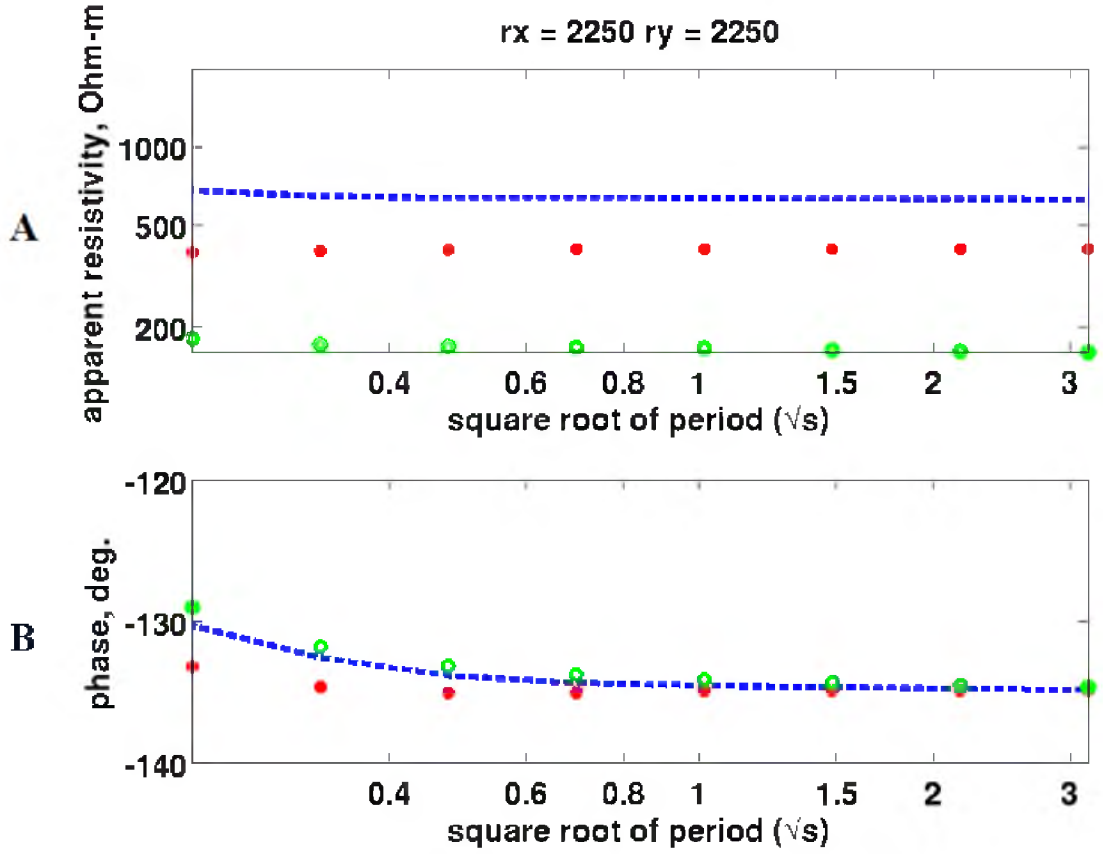


**Figure 5.20**. The apparent resistivity and phase are shown above. A) is the apparent resistivity ($\rho_a$) and B) the phase with respect to the square root of the period, respectively. The measurements are made using the $Z_{yx}$ component of the impedance tensor. The blue dashed line represents the data from L-shaped model with no NSI (model 1), the red and green dots represent the data with full (model 2) and sparse NSI (model 3), respectively. From this figure we can see that the apparent resistivity is affected by the NSI causing static shift, but the phase is much less effected and only in shorter periods (higher frequencies). The apparent resistivity A) is plotted on a log-log scale, and the phase B) is a log scale in the x-direction, and linear scale in the y-direction.

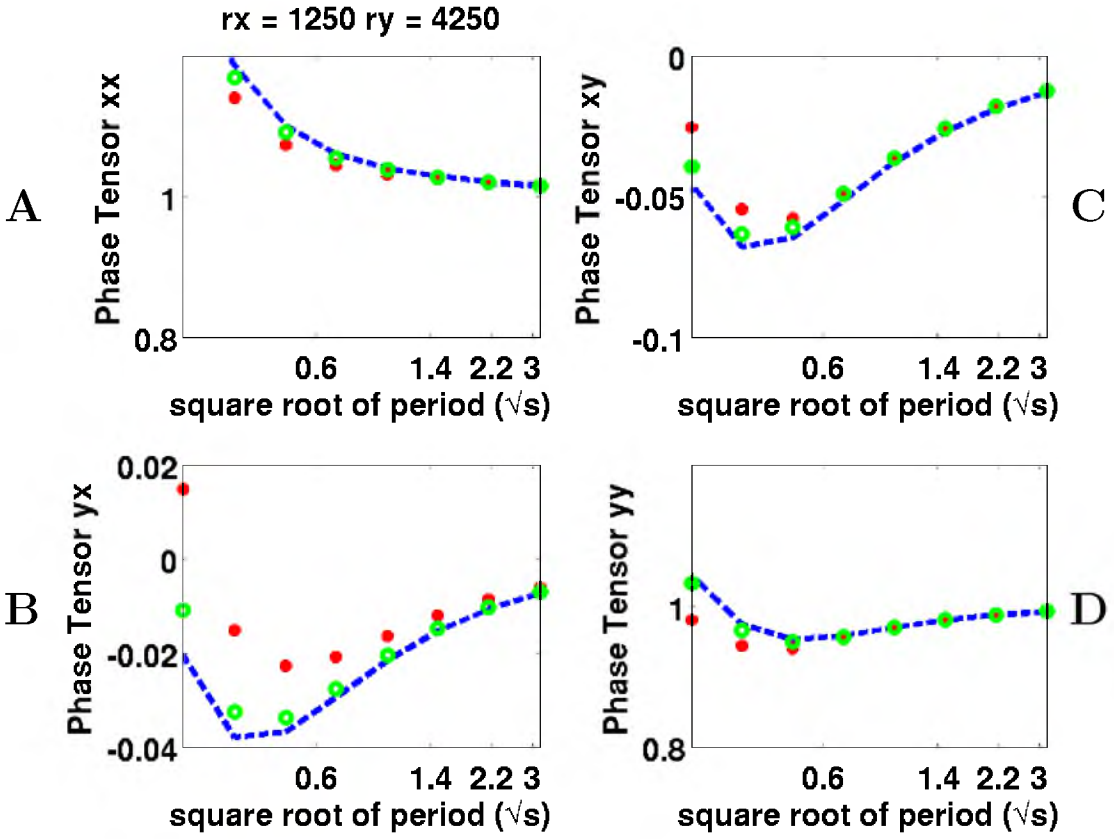


**Figure 5.21**. The four parts above represent data from the individual components of the phase tensor plotted with respect to the square root of period. The blue dashed line represents the data from L-shaped model with no NSI (model 1), the red and green dots represent the data with full (model 2) and sparse NSI (model 3), respectively. It is expected that these data are exactly the same, however, there are small gaps especially in parts B) and C). This figure demonstrates that the phase tensor works fairly well at removing effects due to NSI. All the plots have a log scale in the x-direction and linear scale in the y-direction.

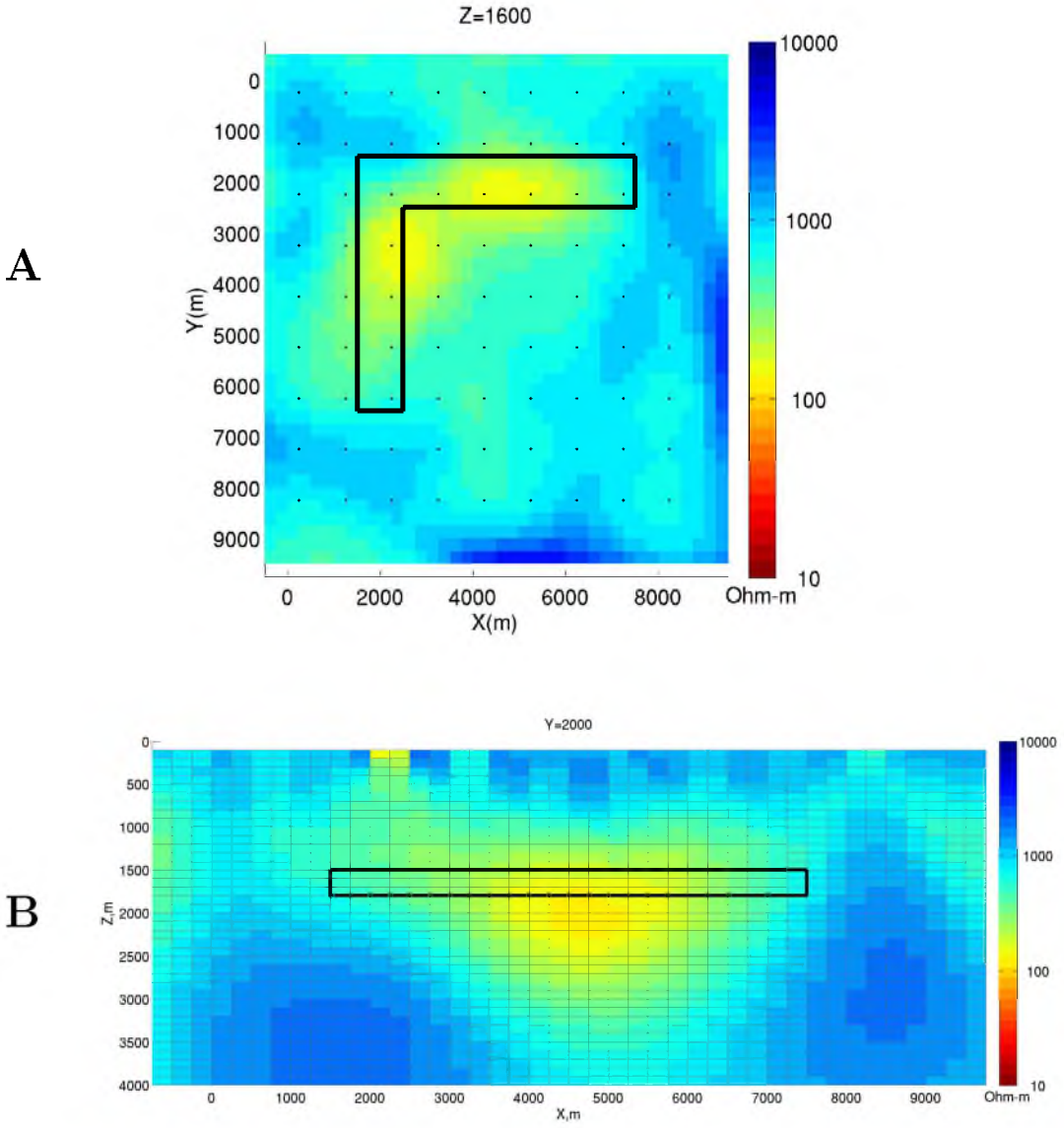


**Figure 5.22**. A horizontal and vertical slice of the inversion results of the L-shaped body with sparse NSI, as shown in Figure 5.17, located at A) Z=1600 m and B) Y = 2000 m. The synthetic data came from the principal components of the impedance tensor ($Z_{xy}$, $Z_{yx}$). The black L-shaped lines and rectangle represent the location of the true body in the horizontal and vertical direction, respectively. The recovered body has an average resistivity greater than 100 Ω-m, while the true body was 10 Ω-m. The inverted body matches the original L-shaped body in the horizontal view, but it is smeared in the Z direction. This is because MT is a diffusive method. There is also an anomaly above the inverted L-shaped body which is caused by NSI. The dots '.' on the horizontal slice represent the location of the receivers.

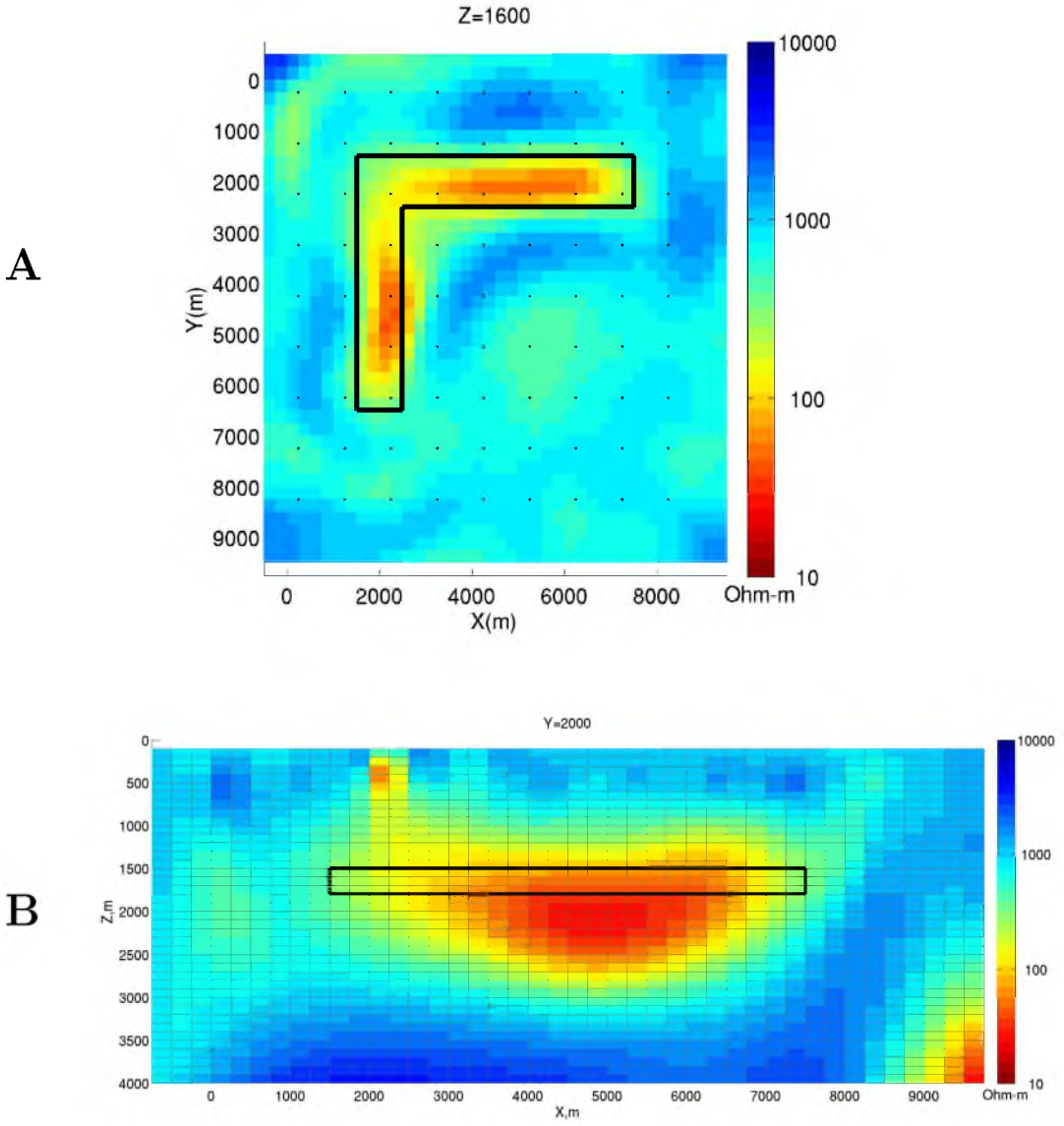


**Figure 5.23**. A horizontal and vertical slice of the inversion results of the L-shaped body with sparse NSI, as shown in Figure 5.17, located at A) Z=1600 m and B) Y = 2000 m. The synthetic data came from all the components of the impedance tensor ($Z_{xy}$, $Z_{yx}$, $Z_{xx}$, and $Z_{yy}$). The black L-shaped lines and rectangle represent the location of the true body in the horizontal and vertical direction, respectively. The recovered body has an average resistivity greater than 100 Ω-m, while the true body was 10 Ω-m. The inverted body matches the original L-shaped body in the horizontal view, but it is smeared in the Z direction. This is because MT is a diffusive method. There is also an anomaly above the inverted L-shaped body which is caused by NSI. The dots '.' on the horizontal slice represent the location of the receivers.

A

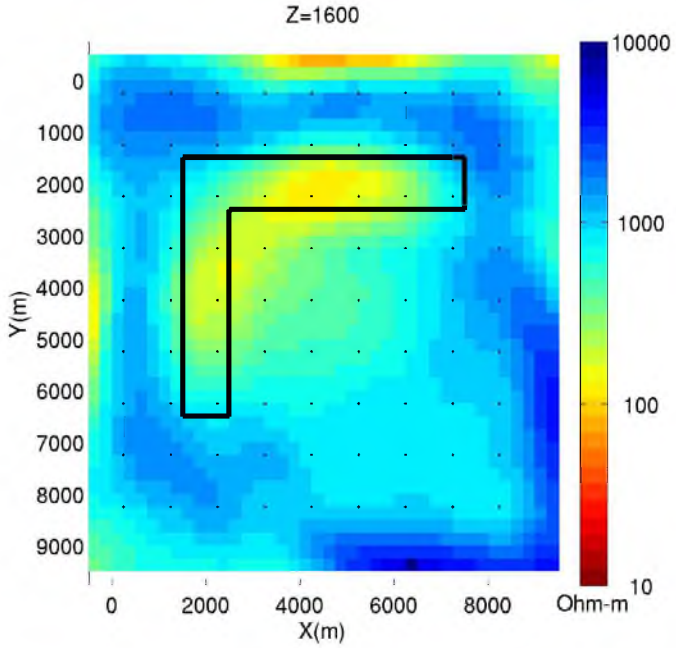


B

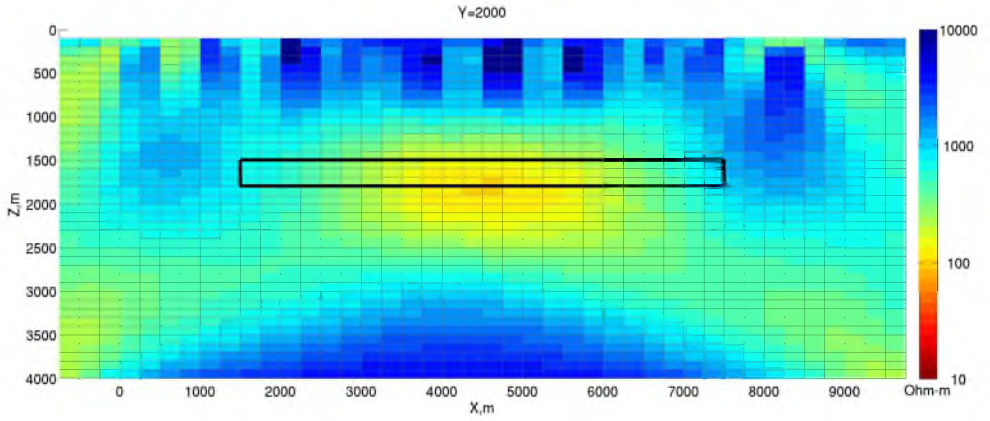


**Figure 5.24**. A horizontal and vertical slice of the inversion results of the L-shaped body with sparse NSI, as shown in Figure 5.17, located at A) Z=1600 m and B) Y = 2000 m. The synthetic data came from the principal components of the phase tensor ($\Phi_{xx}$, and $\Phi_{yy}$). The black L-shaped lines and rectangle represent the location of the true body in the horizontal and vertical direction, respectively. The recovered body has an average resistivity greater than 100 Ω-m, while the true body was 10 Ω-m. The inverted body matches the original L-shaped body in the horizontal view, but it is smeared in the Z direction. This is because MT is a diffusive method. Notice that the inverted results are very similar to those with no NSI. The dots '.' on the horizontal slice represent the location of the receivers. Notice that the inverted results are very similar to those with no NSI.

A

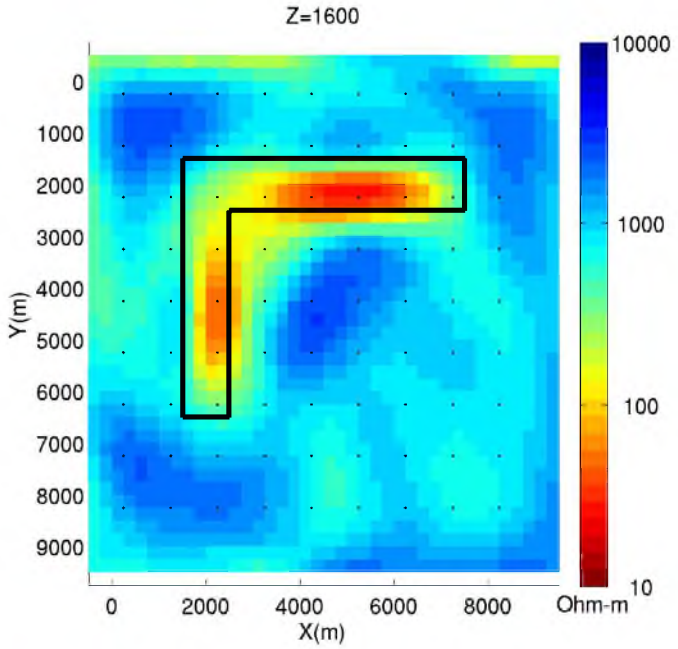


B

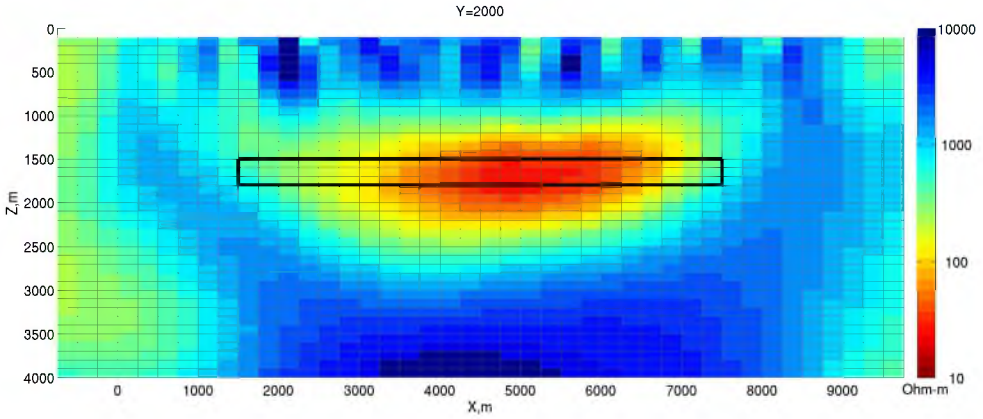


**Figure 5.25**. A horizontal and vertical slice of the inversion results of the L-shaped body with sparse NSI, as shown in Figure 5.17, located at A) Z=1600 m and B) Y = 2000 m. The synthetic data came from all the components of the phase tensor ($\Phi_{xy}$, $\Phi_{yx}$, $\Phi_{xx}$, and $\Phi_{yy}$). The black L-shaped lines and rectangle represent the location of the true body in the horizontal and vertical direction, respectively. The recovered body has an average resistivity greater than 100 Ω-m, while the true body was 10 Ω-m. The inverted body matches the original L-shaped body in the horizontal view, but it is smeared in the Z direction. This is because MT is a diffusive method. Notice that the inverted results are very similar to those with no NSI. The dots '.' on the horizontal slice represent the location of the receivers.

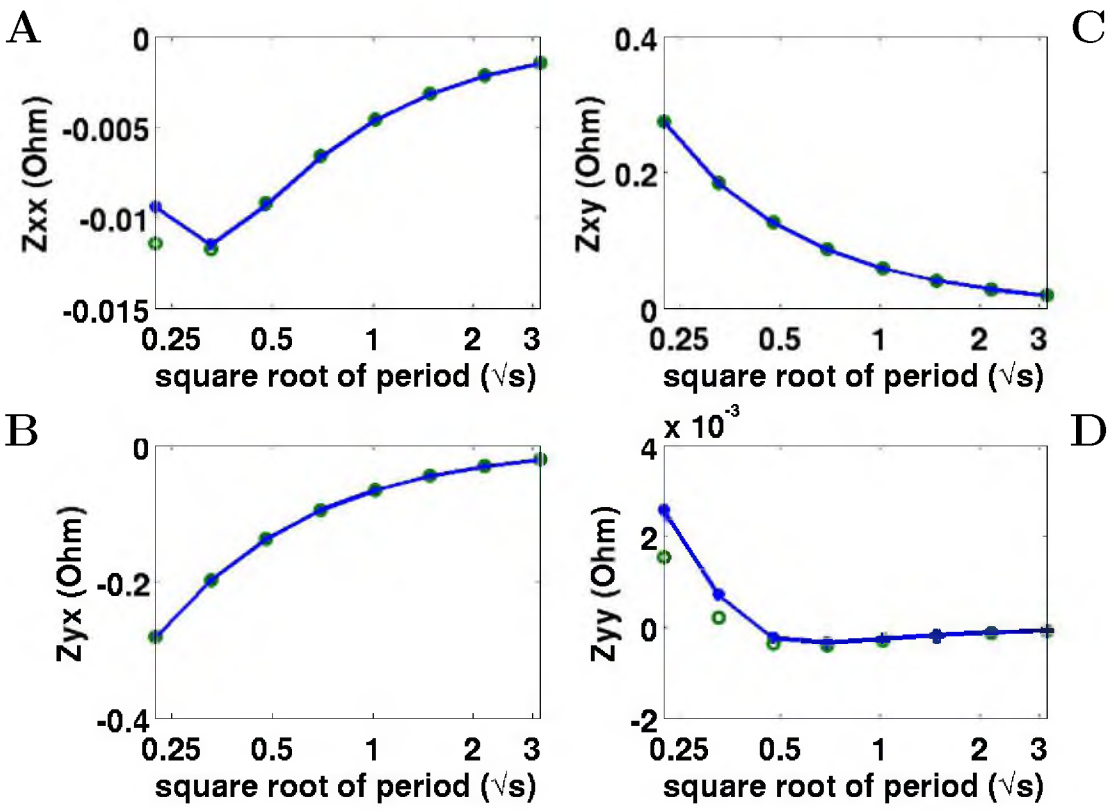


**Figure 5.26**. Observed and predicted data, from model one with no noise added, for the individual components of the impedance tensor with respect to the square root of period. The blue lines with blue dots represent the observed data, and the green circles represent the predicted data. Notice that the predicted data matches the observed data almost perfectly. The receiver is located at rx = 4250 m and ry = 8250 m.

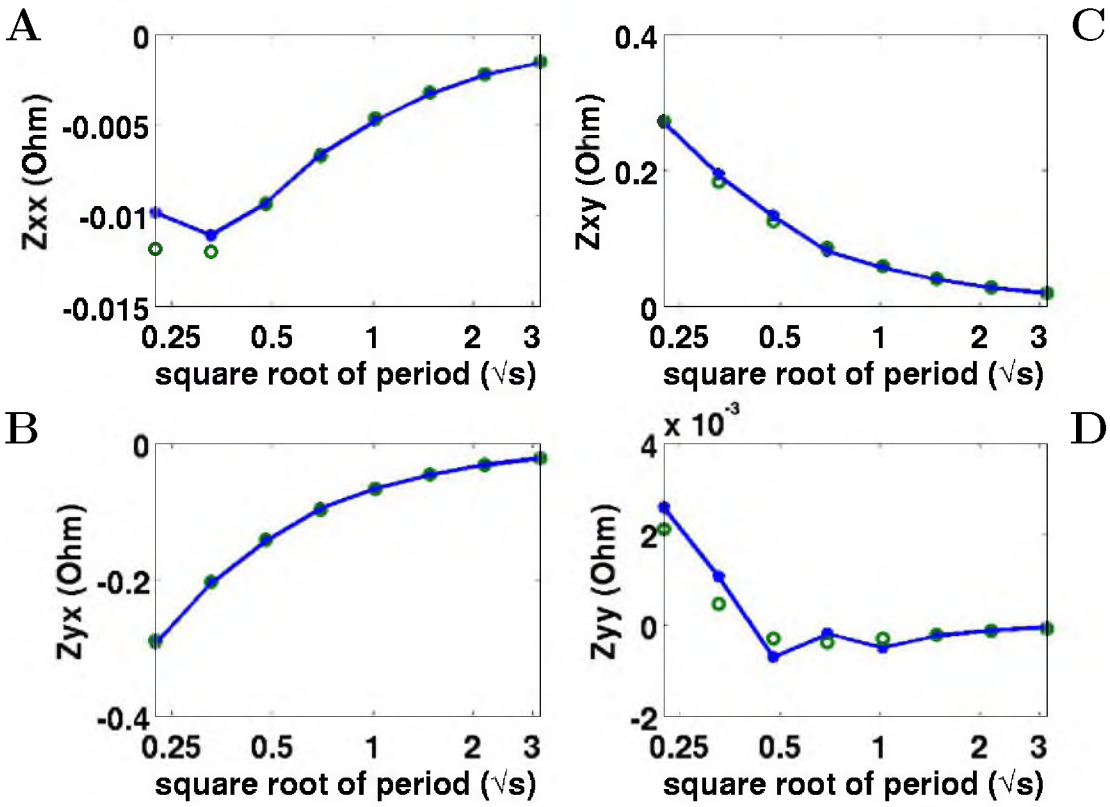


**Figure 5.27**. Observed and predicted data, from model one with 5% noise added, for the individual components of the impedance tensor with respect to the square root of period. The blue lines with blue dots represent the observed data, and the green circles represent the predicted data. Notice that the predicted data matches the observed data almost perfectly for the principal components ($Z_{xy}$ (B) and $Z_{yx}$ C); however, the auxiliary components ($Z_{xx}$ A) and $Z_{yy}$ D)) are slightly affected by the added noise. The receiver is located at rx = 4250 and ry = 8250 m.

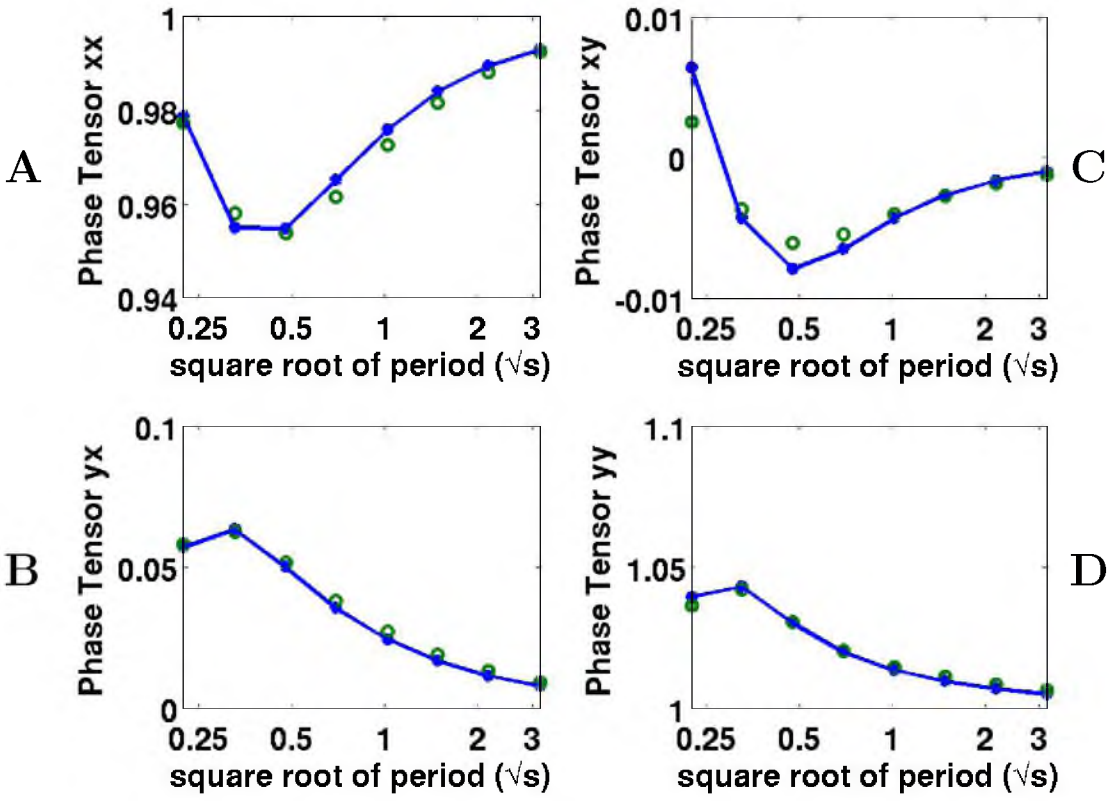


**Figure 5.28**. Observed and predicted data, from model one with no noise added, for the individual components of the phase tensor with respect to the square root of period. The blue lines with blue dots represent the observed data, and the green circles represent the predicted data. Notice that the predicted data matches the observed data almost perfectly. The receiver is located at rx = 4250 and ry = 8250 m.

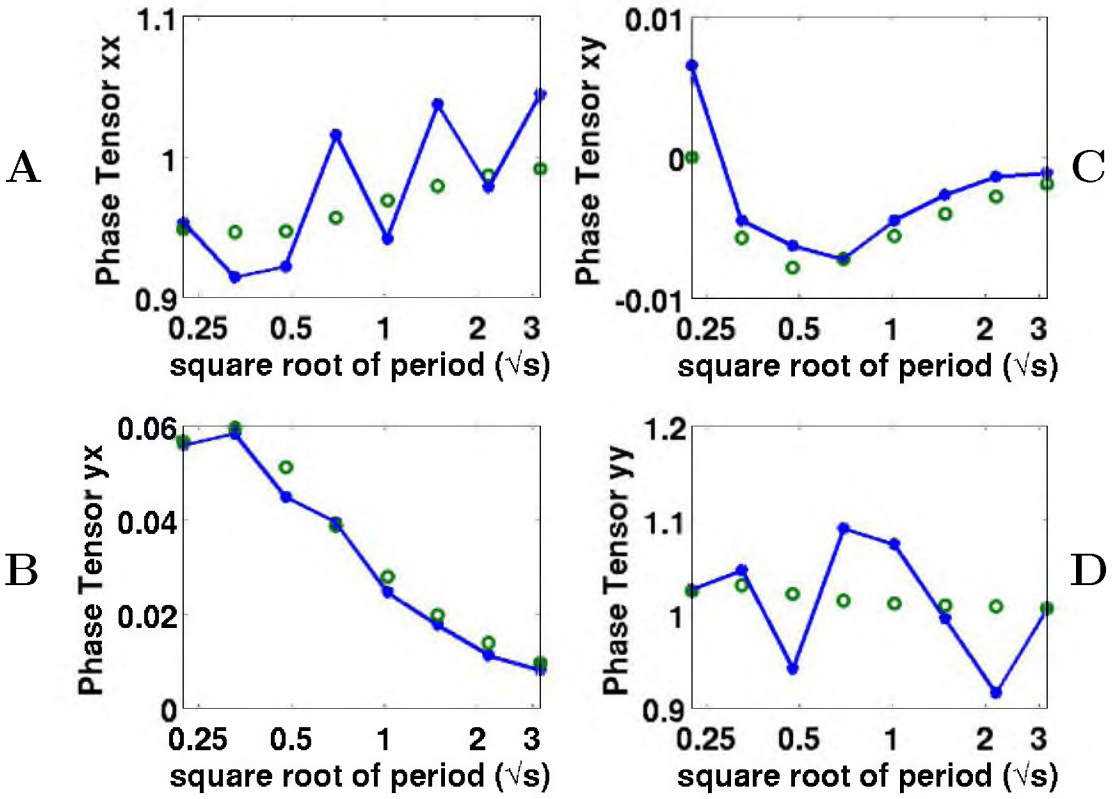


**Figure 5.29**. Observed and predicted data, from model one with 5% noise added, for the individual components of the phase tensor with respect to the square root of period. The blue lines with blue dots represent the observed data, and the green circles represent the predicted data. Notice that all of the components are affected by the added noise. The receiver is located at rx = 4250 and ry = 8250 m.

# CHAPTER 6

# CASE STUDY: MCARTHUR RIVER MT SURVEY

In this chapter, a MT data set from the McArthur River area will be inverted using both the impedance and phase tensors. These results will be compared with inversion results from four publications using the same data set. The McArthur River area is important because it hosts the world's largest concentration of high grade uranium. It is located in the northern part of the Saskatchewan province which is within the Athabasca basin. The MT method is used because it can detect the very low resistivity of the graphite deposits in this area. The graphite is partly responsible for the precipitation of the uranium in this location (Lehmann, 2008).

## 6.1 Geology of the survey area

The presence of significant amounts of uranium ore is why the geology of the McArthur River area is of particular interest. In the upper 10 km of the Earth's continental crust there is an average of 2.7 g/t of U. The uranium concentration in some parts of the McArthur River area is 20% U, or approximately 200,000 g/t. This means the concentration of uranium at McArthur River is about 74,000 times the average concentration within the Earth's crust. The reason why this area has such high concentrations of uranium is large volumes of rock have their uranium leached by oxidized warm water which deposits uranium in a compact site commonly in the form of uraninite ($UO_2$). Uranium has two naturally occurring oxidation states; hexavalent ($U^{6+}$), which is highly soluble, and tetravalent ($U^{4+}$), which is highly insoluble. This is summarized in the following reaction:

$$U^{6+}(aqueous) + 2e^- = U^{4+} \downarrow (precipitation)$$

Uranium can be transported by various complexes. The key is to reduce an oxidized solution with organics (Lehmann, 2008).

The bedrock of the Athabasca basin consists of the Athabasca Group, mostly siliciclastic rocks-sandstone conglomerate and mudstone, overlying basement of Wollaston Domain Mesoproterozoic gneisses of the Trans-Hudson Orogen. An unconformity separates the basement rock and the overlying Athabasca group. Uranium deposits are located at this interface. The Athabasca group is divided into four members. From oldest to youngest they are: MFa (or Read Formation RD) – discontinuous basal conglomerate, intercalated coarse sandstone, conglomerate and red mudstone; MFb-interbedded conglomerate and pebbly sandstone; MFc-granule sandstone; MFd-medium-fine sandstone with mudstone intraclasts (Figure 6.1).

The McArthur River area is a textbook example of an unconformity-type uranium deposit, and there are several subtypes. It is located within the Athabasca basin which is situated on the stable North American Craton. Large amounts of oxidized warm water, can leach the uranium from the overlying km-thick red sandstone and underlying metamorphic basement (Lehmann, 2008). The basement rock has a layer of regolith above it which is believed to be the source uranium (Ruzicka, 1996). There is a reverse fault in the area, locally referred to as the P2 fault (Figure 6.2 from Tuncer et al. 2006), which is associated with high concentrations of graphite. Deposits of this type are thought to have formed through an oxidation-reduction reaction where oxidized fluids mix with reducing fluids. This occurs at the unconformity between the basement rocks and overlying sedimentary rocks. The P2 fault is a graphitic fault that might be the conduit for the reducing fluids (Bronkhorst et al., 2012) The fault acts as a high permeability and porosity conduit which allows the fluids, with aqueous uranium, to flow through this region much easier than other areas (McGill et al., 1993). As the uranium-charged water interacts with the reducing agent within the fault it precipitates uraninite. The oxidized water with aqueous uranium, the P2 fault with high permeability and porosity, and high concentration of graphite, in combination explain why there exist significant uranium deposits in association with the graphite and P2 fault (Lehmann, 2008).

The McArthur river deposit contains nine distinct mineralized areas. The names of the mineralized areas are Zone 1, Zone 2, Zone 3, Zone 4, South, Zone A, Zone B, McA North (1) and McA North (2). Figure 6.3 shows an orthogonal view of the underground development and mineralized zones. Figure 6.4 shows a plan view of the surface drill collar location map. This map includes the locations of the known mineralized areas. All of the McArthur River mineralization is associated with the graphitic P2 thrust fault. With the exception of Zone 2, most of the mineralization is located within the Athabasca sandstone and adjacent basement rocks, near the main zone of thrust faulting (Figure 6.5). Zone 2 mineralization occurs deeper in the basement rocks in a unique location of the deposit (Figure 6.5). The P2 thrust fault is the most critical mineralization control within the McArthur River deposit. From surface drilling the strike length of the uranium mineralization is 1,700 m. The depths of the mineralization are 500 m to 640 m below the surface. The width of the mineralized zone is variable, however, most of the high grade mineralization occurs proximal to the main graphitic thrust fault (Bronkhorst et al., 2012).

During the initial mineralizing event botryoidal uraninite masses and subhedral uraninite aggregates. Pyrite, chalcopyrite, and galena were also deposited during the earliest phase of mineralization. Later deposit events include, remobilized uraninite that occurs as disseminated veinlets, and fracture coatings within chlorite breccia zones and along margins of silt beds in the Athabasca sandstone. Other minerals found in trace amounts include: nickel, cobalt, and arsenic bering minerals (Bronkhorst et al., 2012).

The resistivity of the subsurface stratum has been measured from borehole data at the McArthur River as shown in Figure 6.6 (Tuncer et al., 2006; Mwenifumbo et al., 2004). The resistivity logs indicate resistive upper members on the order of 1000 m, which increases up to 10000 m in the middle of the section, and very low resistive lower sections with a resistivity on the order of 100 m. The upper sandstone stratus changes its resistivity due the change in porosity. The decrease in porosity causes an increase in resistivity. The porosity decreases with depth, because the Athabasca Group layers are altered mainly due to silicification (Mwenifumbo et al., 2004). Ascending fluids silicified the sandstone prior to mineralization (Tuncer et

al., 2006). There are no resistivity logs of the basement rock. The boreholes did intersect the high-grade uraninite and crystalline basement; however, these boreholes were cemented to the top of the mineralized zone for environmental reasons. Because of the cemented logs no borehole data were collected (Mwenifumbo et al., 2004).

## 6.2 Practical MT data

As discussed in Chapter 1, MT's data source is natural EM waves from the magnetospheric and ionospheric currents. The natural fields do not produce impedance values for all frequencies, and these are referred to as dead bands (see Figures 6.7 - 6.9; Simpson and Bahr, 2005). One way to overcome this problem is interpolation of the data points as shown in Figures 6.7 - 6.9. First 1D interpolation was done (Figure 6.7) followed by a 2D interpolation (Figures 6.8 - 6.9). The 1D interpolation was done using the MATLAB function interp1 which is a code developed to interpolate 1D data sets. The 2D interpolation was completed using the MATLAB function TriScatteredInterp, which is a code used to interpolate 2D and 3D data sets. The default linear interpolation setting was used in both the 1D and 2D interpolations.

## 6.3 Inversion results for impedance tensor

For all the inversion experiments, the same input parameters were used, and the only thing that changed was the data to be inverted. The background conductivity was set to 1/1000 S/m (or resistivity 1000 Ω-m), which is an average of the apparent resistivity of the McArthur River MT data. The background conductivity was confirmed to be reasonable based on borehole data described in the geology section. The cells in the x and y directions were 100 m. In the z direction there are logarithmically-spaced cells that start 10 m and end at 460 meters long with 50 cells in between. There were a total of 111, 88, and 50 cells in the x, y, and z directions, respectively. Therefore, the total number of cells was 488400. The seven frequencies used are 7, 15, 33, 51, 97, 177, and 336 Hz. The frequencies are a subset of those used by Farquharson and Craven (2006). All inversions consist of 50 iterations. Tests using 100 iterations did not improve the results. The resistivity was bounded by the following upper and lower limits: 10,000 Ω-m and 10 Ω-m, respectively (equation

4.5). The parameters $\alpha$ and q were set to 0.01 and 0.5, respectively. Alpha represents the weight of the regularization. In order to make the regularization smaller and to increase convergence alpha is started with a small value. The value q also controls how fast alpha decreases, hence small values are chosen. Other values have been tested, but these values seem to work well in MT (M. Cuma, personal communication, October 27, 2012). The model weight was recalculated on the fifth iteration, and every five iterations until the forty-fifth iteration. This is because the model is changing, so the model weight is recalculated to keep it closer to the actual model. This once again helps increase convergence of the parametric functional (M. Cuma, personal communication, October 27, 2012).

The average dip of the P2 fault is 45° (Ng et al., 2013). The vertical slices selected are 45° to the fault. Therefore the apparent dip should be 35°. Lines have been drawn on all the figures, that have inversion results, to represent the location of the P2 fault at depth. The dashed lines represent the inferred location of the fault with depth. The solid lines represent the known location of the fault due to drilling (E. Petersen, personal communication, November 25, 2013).

The horizontal slices of the principal impedance tensor inversion results are shown in Figures 6.10 - 6.13, which correspond to 250, 500, 750, and 1000 m. The misfit after 50 iterations came to 0.13%. In the slices at depths of 250 and 500 m the images show a predominantly high homogenous resistivity greater than 1000 Ω-m (these sections are above the elevation of the ore bodies and unconformity). This is interpreted to be caused by the resistivity of the Athabasca Group. There are only three small anomalies, two are on the edges, and one in the center whose cause is unknown. The anomaly on the right-hand side with low resistivity is believed to be an artifact because there are no receivers above it, and it is close to the edge which might be an edge effect. The slices at 750 and 1000 m show a strong anomaly in the northeast direction. This anomaly is believed to be due to the very high conductivity (very low resistivity) of the underlying graphite, and it corresponds to the projected location of the P2 reverse fault.

There are also two vertical slices of the principal impedance inversion results shown in Figures 6.14 - 6.15. Figure 6.14 passes through the near the center of the survey

in the north direction at 6402 km. Notice how the anomalies match the horizontal slices. The very low resistivity on the edges is believed to be caused by edge effects. Figure 6.15 passes through the near the center of the survey in the east direction at 496 km. In both the vertical slices described above the there are anomalies in the near surface. These anomalies are believed to be caused by near surface inhomogeneities. The interpreted location of the P2 fault is at the boundary of a large conductive anomaly as shown in Figures 6.14 and 6.15. This implies the inversion results, using the principal components of the impedance tensor, effectively detect the graphite located within the fault.

The horizontal slices of the full impedance tensor inversion results are shown in Figures 6.16 - 6.19, which correspond to 250, 500, 750, and 1000 m. The misfit after 50 iterations was 0.39%. There are very similar results for the full impedance as the principal impedance results. The slices at 250 and 500 m show homogenous background resistivity greater than 1000 Ω-m with only a very small anomaly in the center. The homogenous resistivity is believed to be caused by the Athabasca Group, which is very resistive, and is in the same location. The anomalies on the perimeter are believed to be artifacts, because there are no receivers above them. The slices at 250 and 500 m appear to have much more random conductivities. The random conductivities appear to be caused by the additional data from the auxiliary components of the impedance tensor ($Z_{xx}$ and $Z_{yy}$). They could also be caused by NSI. Similar phenomena are shown in the inversion results of the full impedance tensor with NSI (see Figure 5.23). The slices at 750 and 1000 m show a very strong anomaly in the northeast direction which is also an indicator of the contrast in resistivity due to the graphite within the P2 fault. The predicted data match the observed data very well when the full impedance inversion was done, as shown in Figures 6.22 - 6.25. Notice that the limits of the colorbar are the same for the observed data and the predicted data. Also notice that visually the predicted data match the observed data, which is to be expected.

There are also two vertical slices of the principal impedance inversion results shown in Figures 6.20 - 6.21. Figure 6.20 passes through the near the center of the survey in the north direction at 6402 km. The very low resistivity in the bottom right hand side

is believed to be an artifact due to edge effects. Notice how the anomalies match the horizontal slices. Figure 6.21 passes through the near the center of the survey in the east direction at 496 km. The very low resistivity on the edges is believed to be caused by edge effects. In both the vertical slices described above, there are anomalies in the near surface. These are believed to be caused by NSI. The interpreted location of the P2 fault is at the boundary of a large conductive anomaly as shown in Figures 6.20 - 6.21. This implies the inversion results, using all the components of the impedance tensor, also effectively detect the graphite located within the fault.

## 6.4 Inversion results for phase tensor

The input parameters for the phase tensor were the same as the impedance tensor. The only difference was that the input data were converted to phase tensor data and the Fréchet derivative was changed for the phase tensor. The full phase tensor was inverted, but the inversion results looked unreasonable. Also, the observed data did not match the predicted data. Visually the contour maps of the observed and predicted data did not match.

The principal phase tensor was also inverted using the same input parameters with the only difference being the input data were changed to phase tensor data. The Fréchet derivative was also changed for the phase tensor inversion. The inversion was run for 50 iterations at which time it reached a misfit of 0.96%. The horizontal slices can be seen in Figures 6.26 - 6.29 and they correspond to depth slices at 250, 500, 750, and 1000 m. The slices at 250 and 500 m do not show any strong anomalies, and have resistivity that is similar to the background resistivity. This is believed to be caused by the high resistivity of the Athabasca Group. The slices at 750 and 1000 m show anomalies in the same location as the impedance inversion results. Although the anomalies are in the correct location they appear to trend in the northwest direction. This is not expected because the fault is in the northeast direction. Therefore it appears that the phase tensor does not work properly.

There are also two vertical slices of the principal phase tensor inversion results shown in Figures 6.30 - 6.31. Figure 6.30 passes through near the center of the survey in the north direction at 6402 km. Figure 6.31 passes through near the center of the

survey in the east direction at 496 km. The interpreted location of the P2 fault passes near the boundaries of conductive anomalies as shown in the inversion results of the impedance tensor. This is similar to the results of the impedance tensor, however, the anomalies are much larger.

One possible reason why the phase tensor inversion results are different than the impedance inversion results are because noise from the auxiliary components of the impedance tensor ($Z_{xx}$ and $Z_{yy}$) is added to the less noisy principal components ($Z_{xy}$ and $Z_{yx}$) to produce the components of the phase tensor (equation 3.16). The test in synthetic modeling demonstrates this idea clearly (see Figures 5.26 - 5.29). The observed and predicted data of the full impedance tensor, full phase tensor, and principal phase tensors are shown in the Appendix.

The inversion results from this study are all compared in Figure 6.32 along with inversion results from four other research groups (Craven et al., 2006). Column A shows inversion results using the full impedance tensor. Column B shows the inversion results using the principal impedance tensor. Column C shows the inversion results using the principal components of the phase tensor. Columns A, B, and C are all from this thesis, and are described above. Column D contains the figures from V. Tuncer and M. J. Unsworth (Craven et al., 2006). They used the 2D inversion algorithm described in Rodi and Mackie (2001) which uses finite-difference equations for the forward modeling, and nonlinear conjugate gradients for inversion. The data used were the principal components of the impedance tensor, and tipper, Z component of the magnetic field. Column E is the figures by W. Siripunvaraporn (Craven et al., 2006). The 3D MT algorithm used can be described in Siripunvaraporn et al. (2005). It uses finite-difference for the forward modeling, and data-space Occam inversion method. The data used were the principal components of the impedance tensor. Column F is the results from R. L. Mackie (Craven et al., 2006). The inversion algorithm is described in Mackie et al. (2001). The algorithm uses the finite-difference method for forward modeling, and nonlinear conjugate gradients for inversion. The data used were the full impedance tensor along with the tipper. Column G shows results from C. G. Farquharson (Craven et al., 2006). The algorithm used is described in Farquharson et al. (2002). The algorithm uses finite-volume for the forward

modeling and the Gauss-Newton method for the inversion. The data used were full impedance tensor.

The results from columns A, F, and G all used the full impedance tensor from the McArthur data set. They should all compare to one another. Columns A and F do compare well with one another; the location of the anomaly is in the same location, and it looks similar. The results from column G do not match columns A and F and the reason for this is unknown. The results from column B, D, and E all used the principal components of the impedance tensor, and they all compare well with each other. There are large low resistivity anomalies in the northeast direction at depths of 750 m and 1000 m in the results from A, B, D, E, and F. This is believed to be caused by the graphite with in the P2 reverse fault.

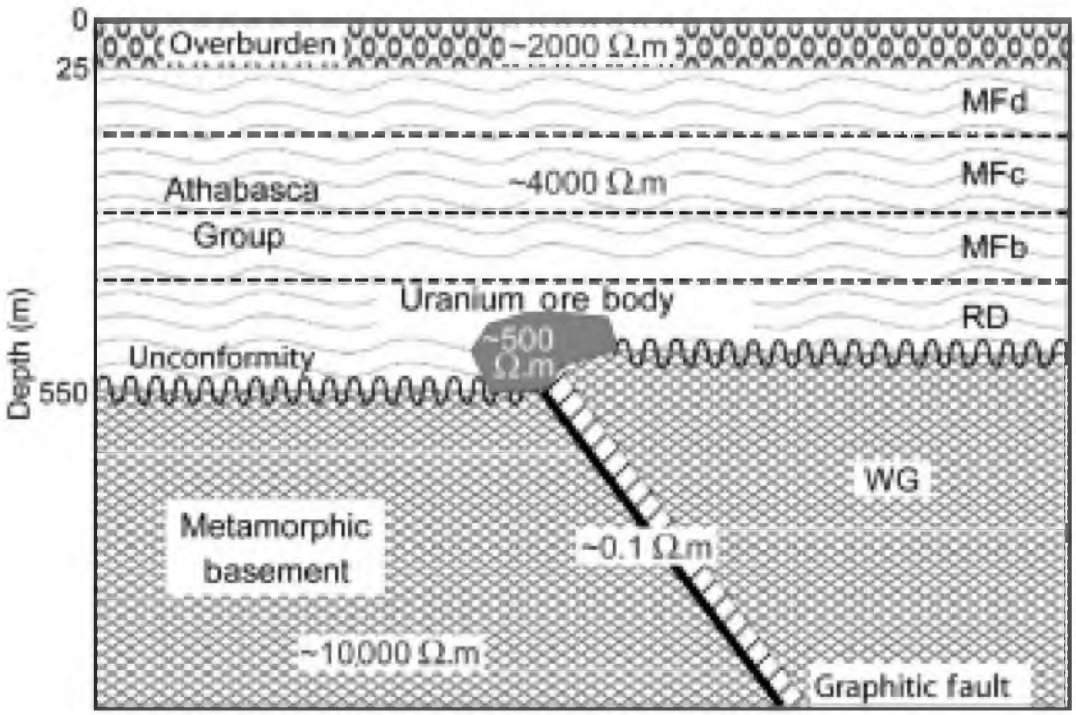


**Figure 6.1**. Generic model of an unconformity-type uranium deposit in the Athabasca basin (modified from McMullan et al., 1987; Mweinfumbo et al. 2004). The Athabasca Group consists of four major units from bottom to top. The Read Formation (RD, formerly MFa) comprises discontinuous basal conglomerate, intercalated coarse sandstone, conglomerate and red mudstone. The Manitou Falls Formation comprises MFb: interbedded conglomerate and pebbly sandstone; MFc: granule sandstone; and MFd: medium-fine sandstone with mudstone intraclasts. WG is the Wollaston Group. (Reprinted with permission Tuncer et al., 2006).

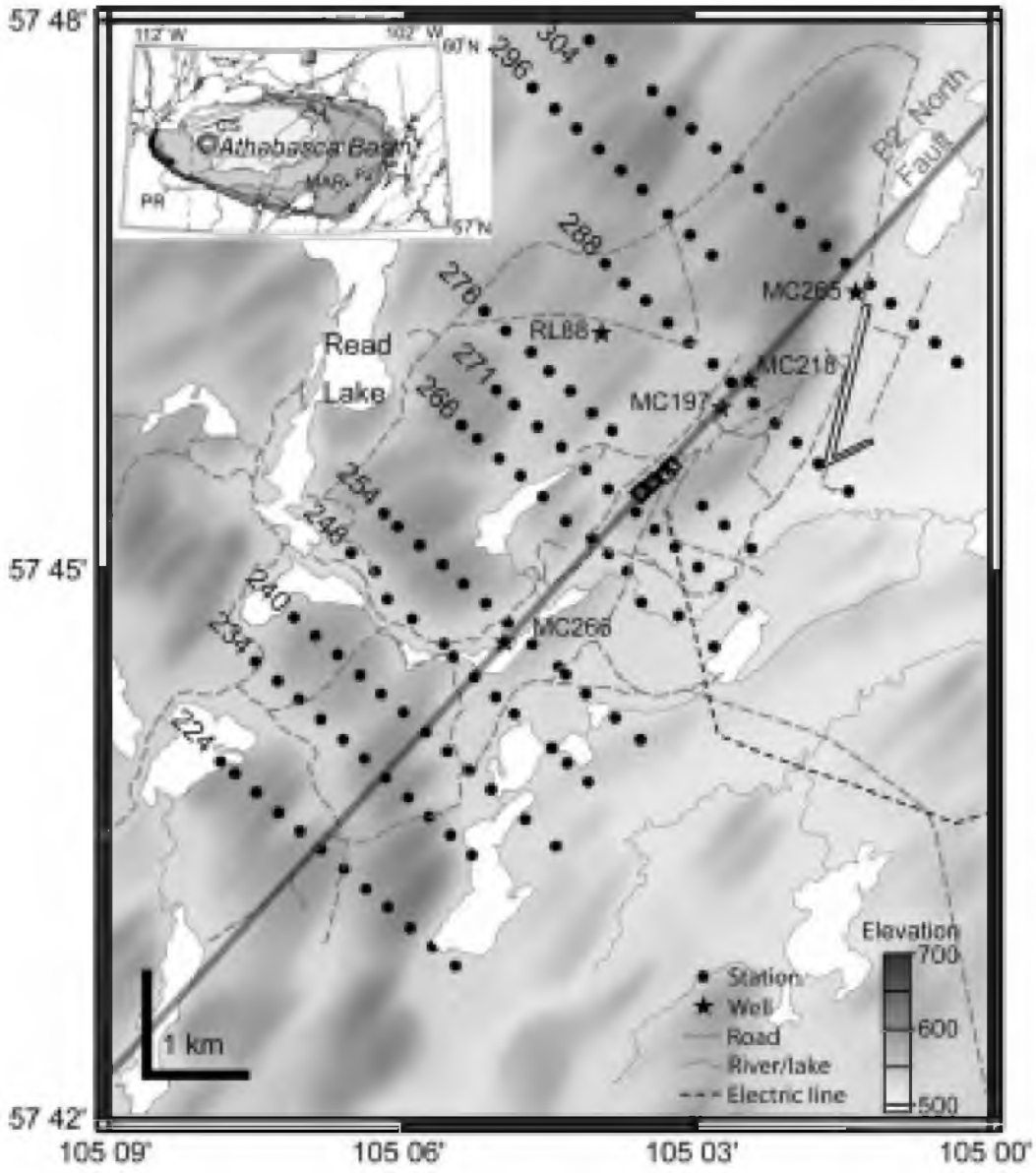


**Figure 6.2**. The location of the P2 fault is displayed above along with the MT station locations used in the McArthur River MT survey. The fault dips to the SW approximately 60°. Black diamonds on the P2 North Fault line between lines 271 and 276 show the uranium ore pods where the mine is located. (Reprinted with permission Tuncer et al., 2006)

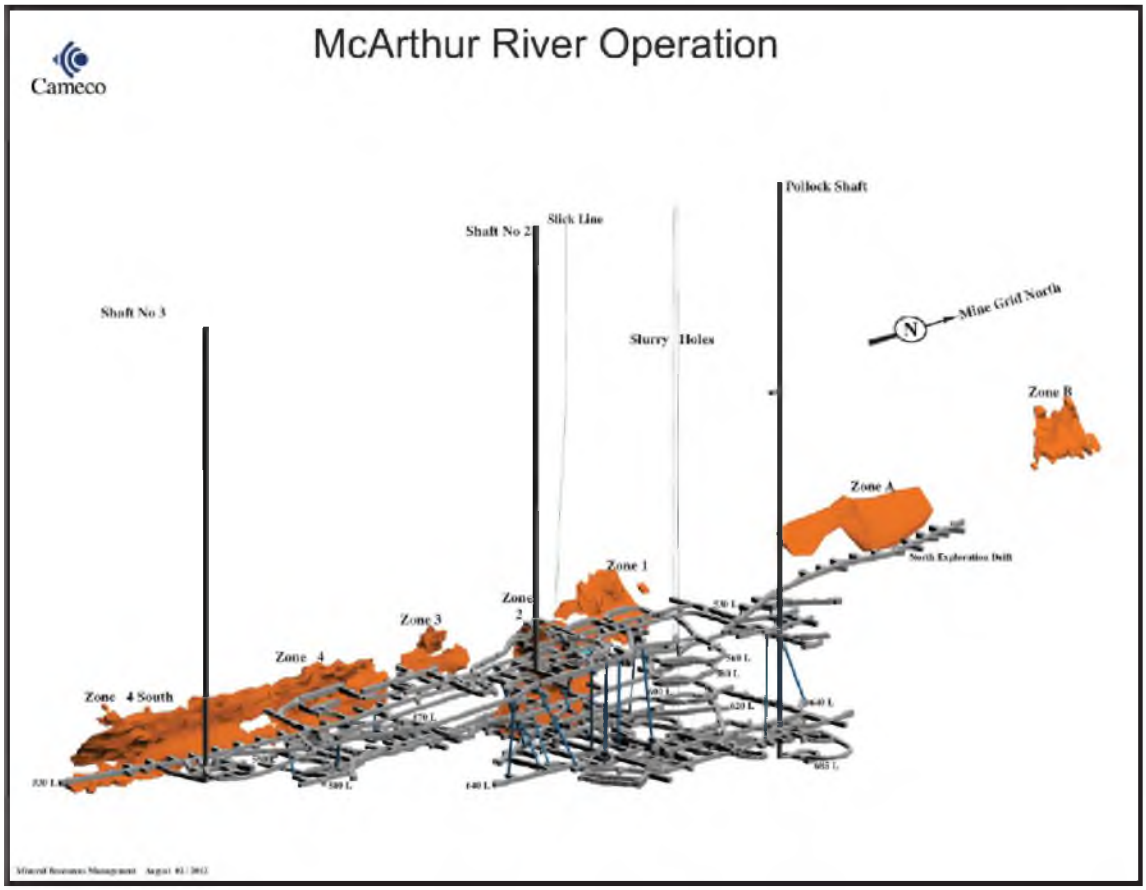


**Figure 6.3**. Orthogonal view of underground development and mineralized zones looking northwest. (Reprinted with permission Bronkhorst et al., 2012)

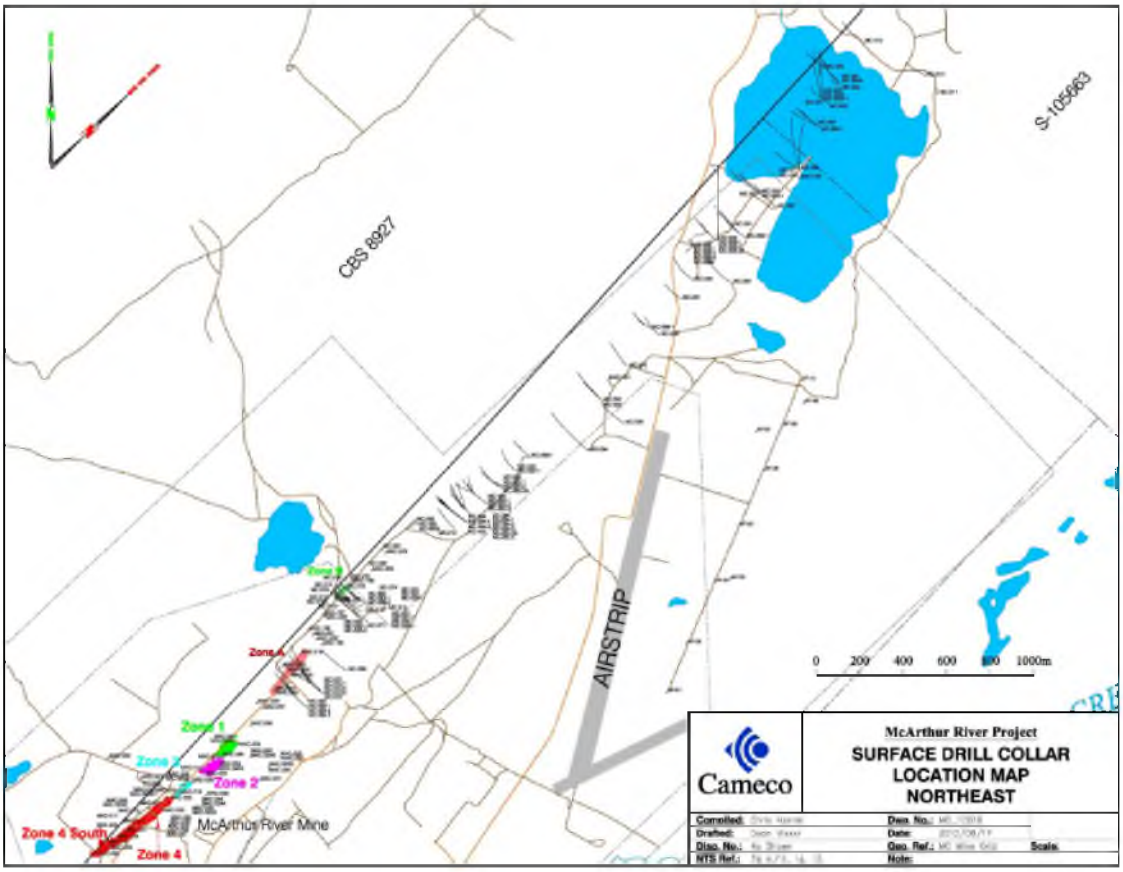


**Figure 6.4**. Surface drill collar location map - northeast. Notes: (1) green north arrow indicates true north. (2) Red north arrow indicates mine grid north. (Reprinted with permission Bronkhorst et al., 2012)

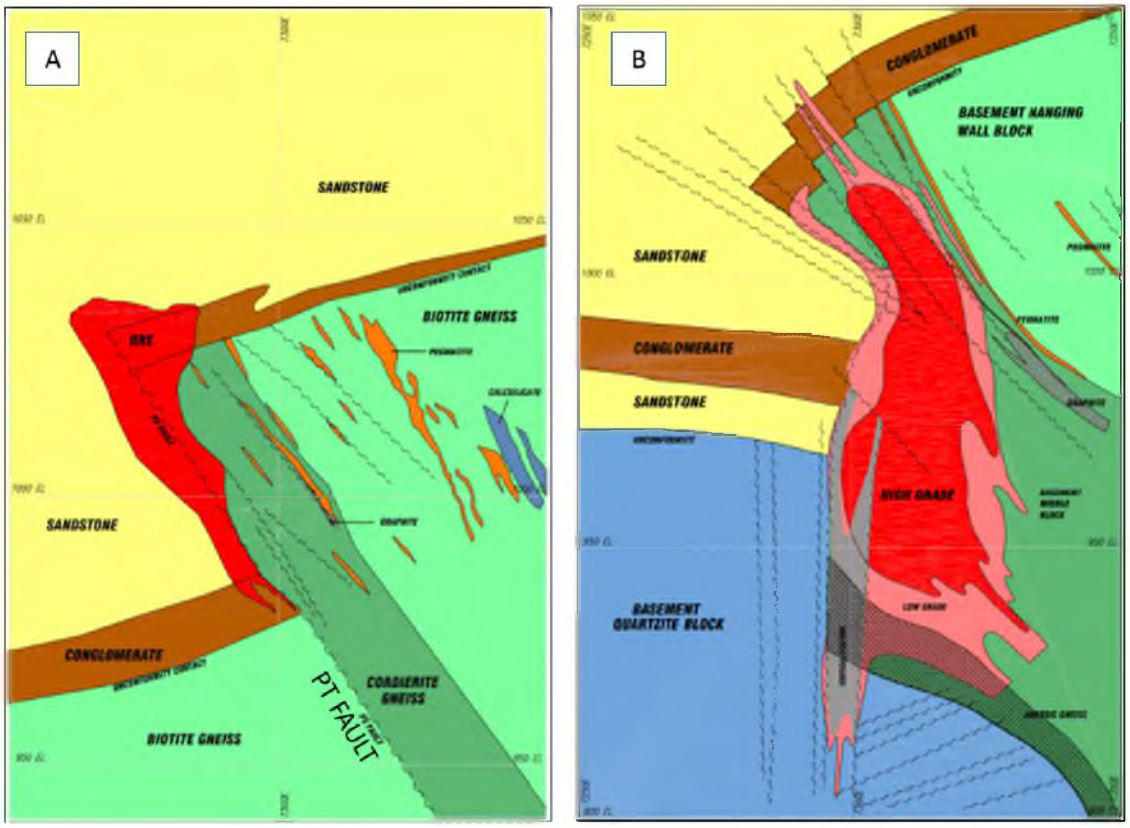


**Figure 6.5**. With the exception of Zone 2, most of the mineralization is located within the Athabasca sandstone and adjacent basement rocks, near the main zone of thrust faulting. A) typical geological cross section. B) typical Zone 2 geological cross-section with mineralization located within the basement rock. (Reprinted with permission Bronkhorst et al., 2012)

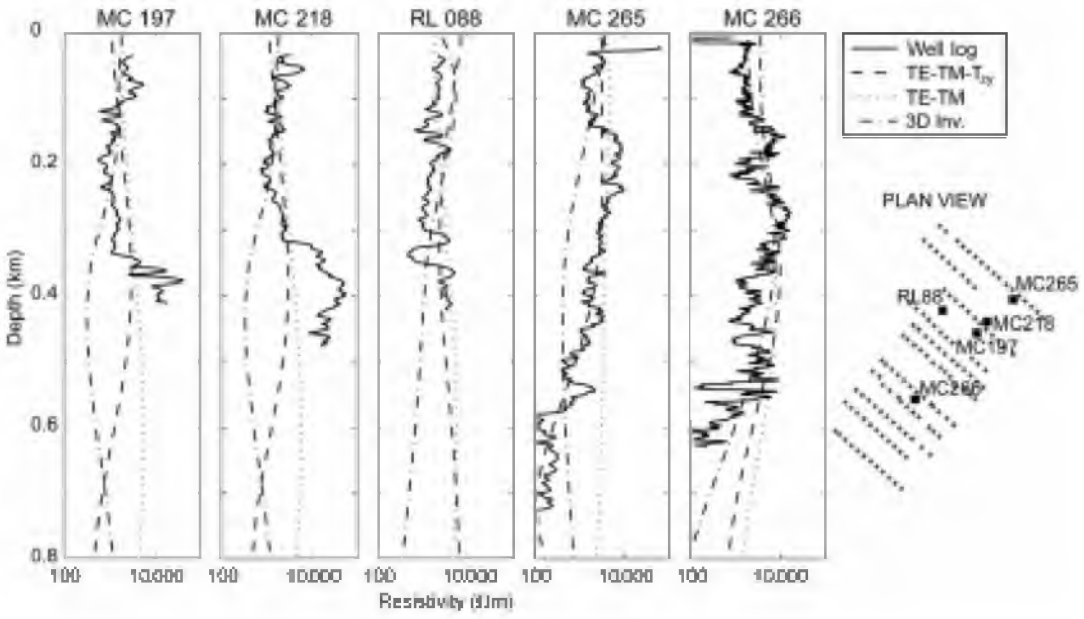


**Figure 6.6**. Comparison of borehole-log resistivity data (after Mwenifumbo et al., 2004) and inversion of 2D and 3D models. Reprinted with permission Tuncer et al. (2006). Notice that the very resistive areas are due to the silicified zones. Also notice that the 2D TE-TM-Tzy inversion results, which are the principal components of the impedance tensor and tipper, match the borehole resistivity very well.

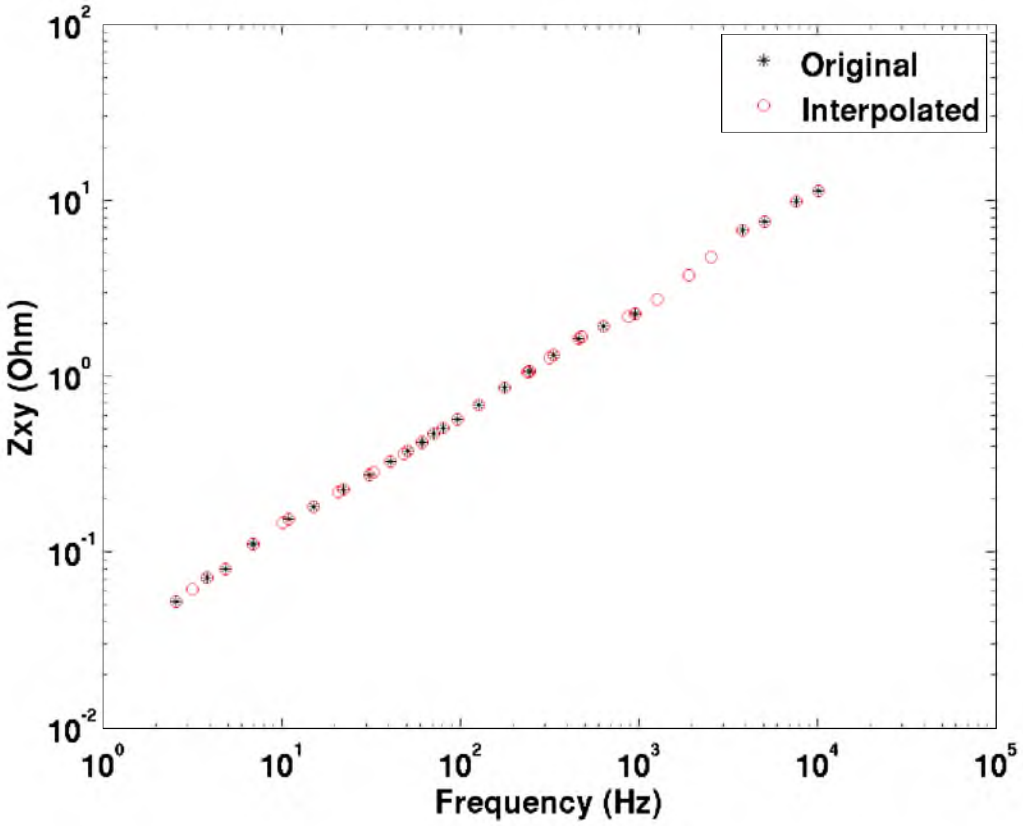


**Figure 6.7**. The impedance from the McArthur River MT data set with respect to frequency. There are dead bands with no data available in this data set. The impedance data were interpolated with respect to frequency to fill in the dead bands. The original and the interpolated data are represented by the stars (*) and circles (o), respectively.

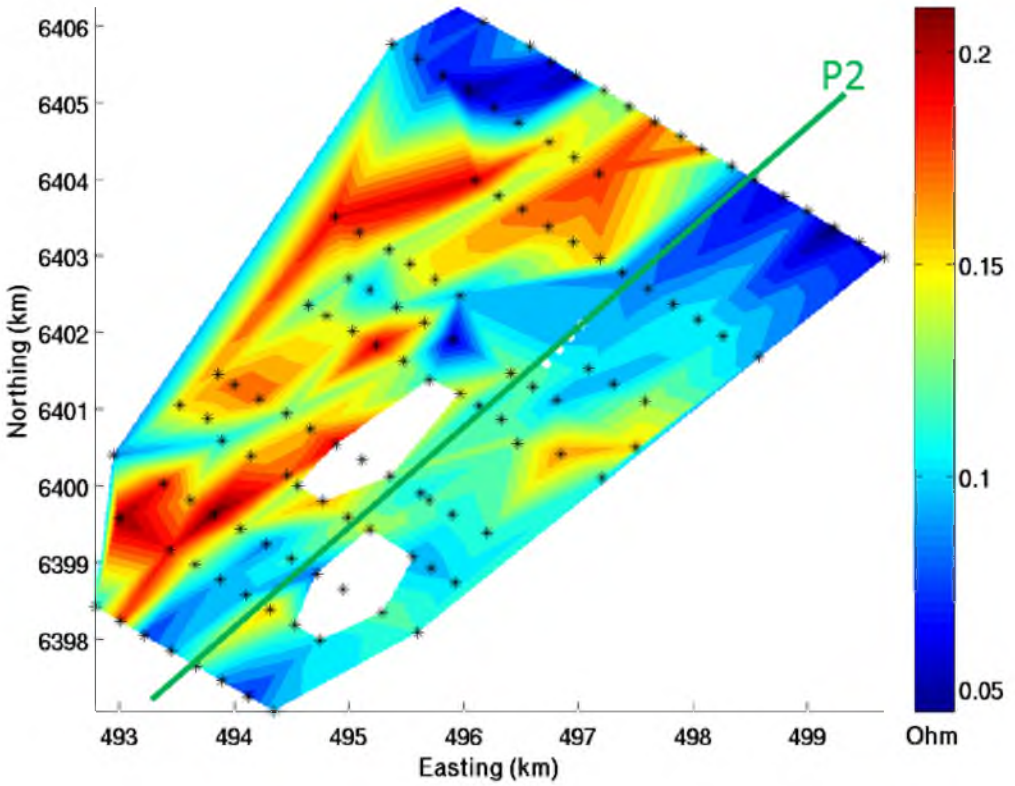


**Figure 6.8**. The real part of $Z_{xy}$ from the impedance tensor from the McArthur River data set. Notice that there are two large holes where no data exist. In Figure 6.9 these holes are removed, and it is done by interpolation. The stars represent the location of the receivers. The black dots represent the approximate location of the uranium ore pods where the mine is located within the P2 fault. The green line represents the approximate location of the P2 fault at 500 m below the surface.

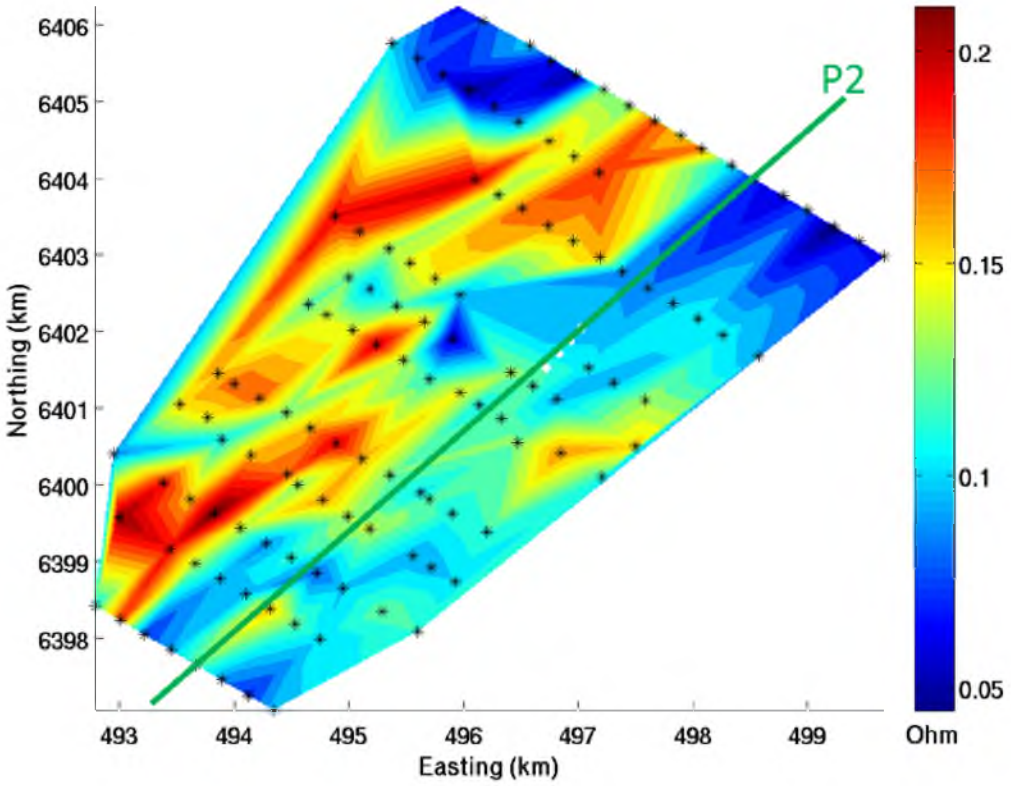


**Figure 6.9**. The real part of $Z_{xy}$ from the impedance tensor from the McArthur River data set. Notice that the two large holes where no data exist from Figure 6.8 are gone. They were removed by 2D interpolation. The triscatterdinterp function was used in MATLAB for the interpolation. The stars represent the location of the receivers. The black dots represent the approximate location of the uranium ore pods where the mine is located within the P2 fault. The green line represents the approximate location of the P2 fault at 500 m below the surface.

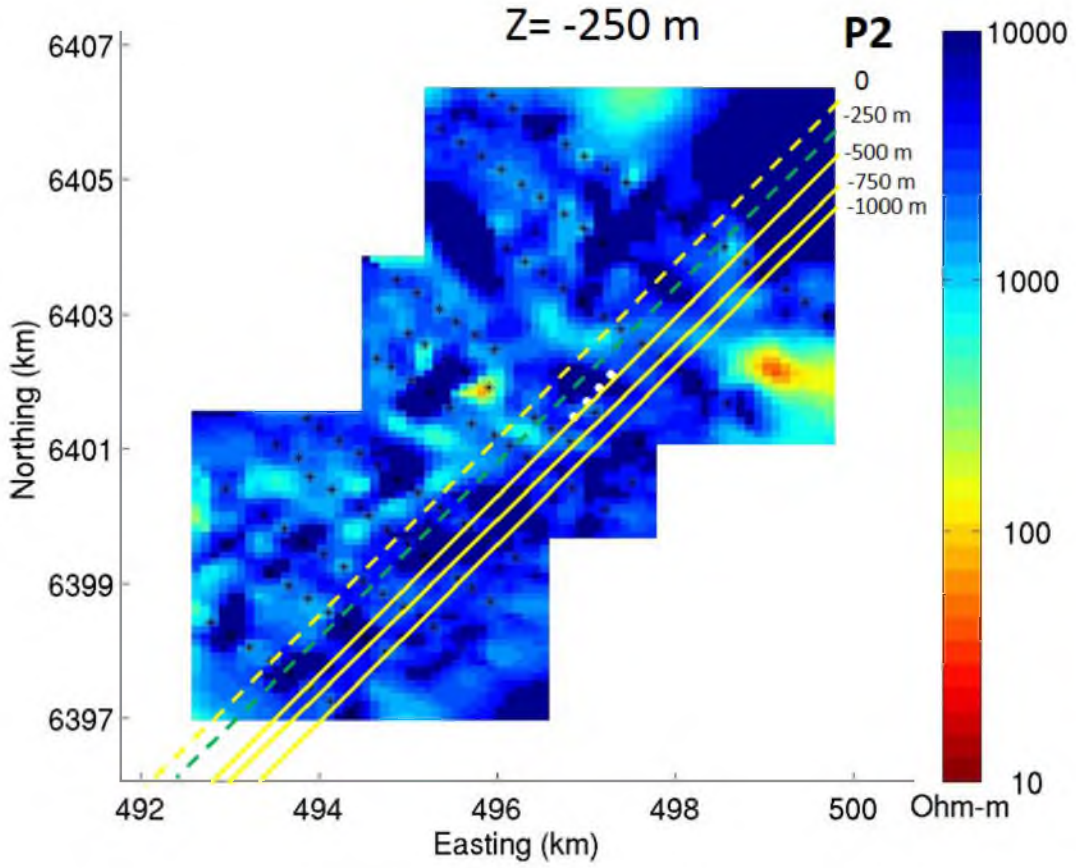


**Figure 6.10**. Horizontal slice of the inversion results located 250 m below the surface. Above the unconformity located approximately 500 m below the surface. The input data were the principal components, $Z_{xy}$ and $Z_{yx}$, of the McArthur River impedance tensor. The stars represent the location of the receivers. The white dots represent the approximate location of the uranium ore pods, at about 500 m, depth where the mine is located. The apparent dip of the P2 fault is 35°. The dashed lines represent the inferred location of the fault with depth. The solid lines represent the known location of the fault due to drilling. The green line represents the current fault location. The yellow lines represent the fault location above and below the current depth (E. Petersen, personal communication, November 25, 2013). Notice that the resistivity is mostly homogenous and very resistive. It is close to the background resistivity of 1000 Ω-m. The anomaly on the right had side does not have receivers above it, so it is unknown if it is due to low resistivity below or because an artifact. The cause of the anomaly in the center of the figure is unknown.

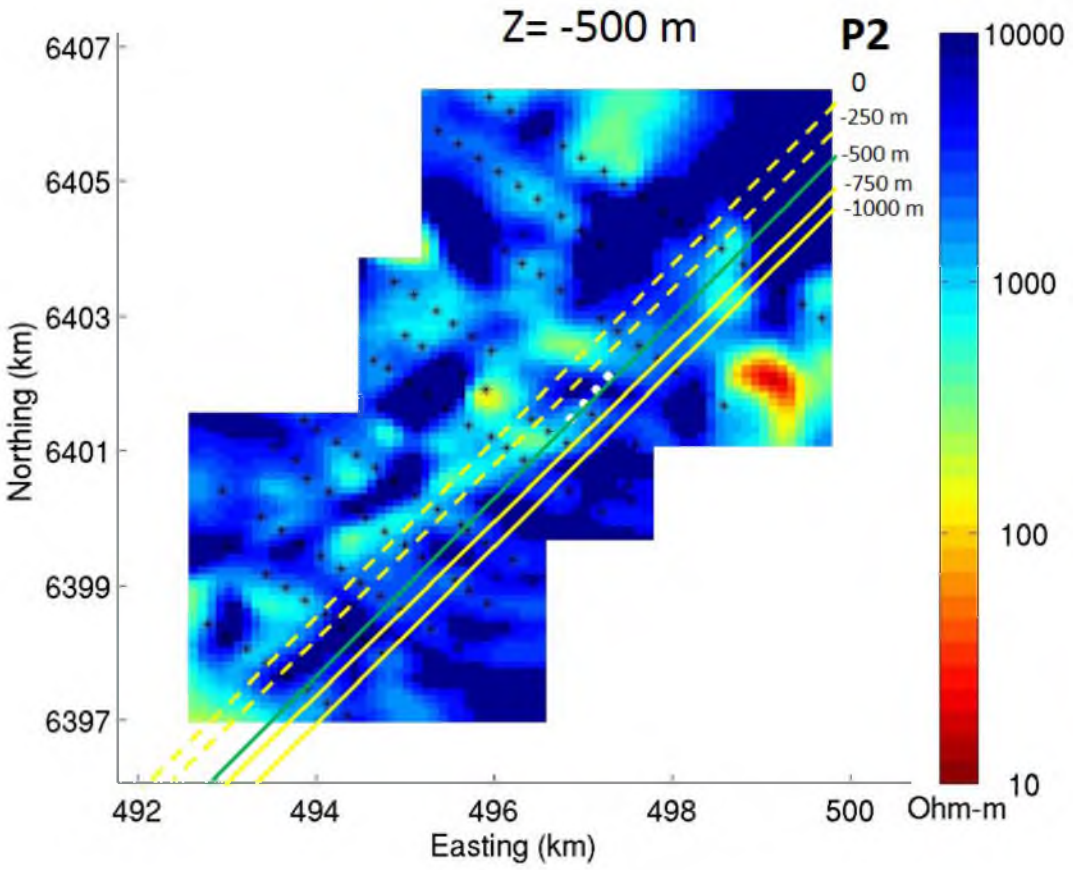


**Figure 6.11**. Horizontal slice of the inversion results located 500 m below the surface the approximate location of the unconformity. The input data were the principal components, $Z_{xy}$ and $Z_{yx}$, of the McArthur River impedance tensor. The stars represent the location of the receivers. The apparent dip of the P2 fault is 35°. The dashed lines represent the inferred location of the fault with depth. The solid lines represent the known location of the fault due to drilling. The green line represents the current fault location. The yellow lines represent the fault location above and below the current depth (E. Petersen, personal communication, November 25, 2013). The white dots represent the approximate location of the uranium ore pods, at about 500 m depth, where the mine is located. Notice that resistivity is mostly homogenous. There are no receivers above the anomaly on the right hand side, so it is could be an artifact. The cause of the anomaly in the center of the figure is unknown.

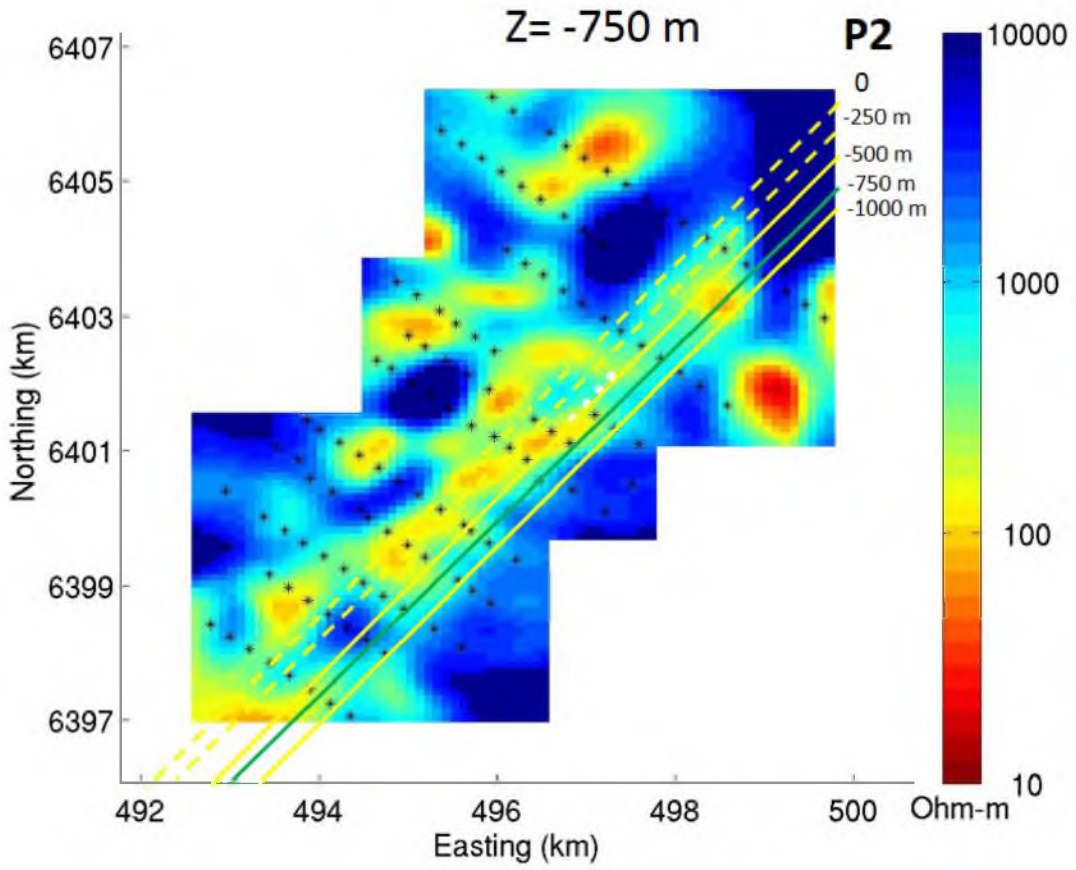


**Figure 6.12**. Horizontal slice of the inversion results located 750 m below the surface. Below the unconformity, located approximately 500 m below the surface. The input data were the principal components, $Z_{xy}$ and $Z_{yx}$, of the McArthur River impedance tensor. The locations of the receivers are represented by the stars. The white dots represent the approximate location of the uranium ore pods, at about 500 m depth, where the mine is located. The apparent dip of the P2 fault is 35°. The dashed lines represent the inferred location of the fault with depth. The solid lines represent the known location of the fault due to drilling. The green line represents the current fault location. The yellow lines represent the fault location above and below the current depth (E. Petersen, personal communication, November 25, 2013). Notice that there are several low resistivity anomalies that are in northeast direction. This is due to the low resistive graphite that is in the northeast direction.

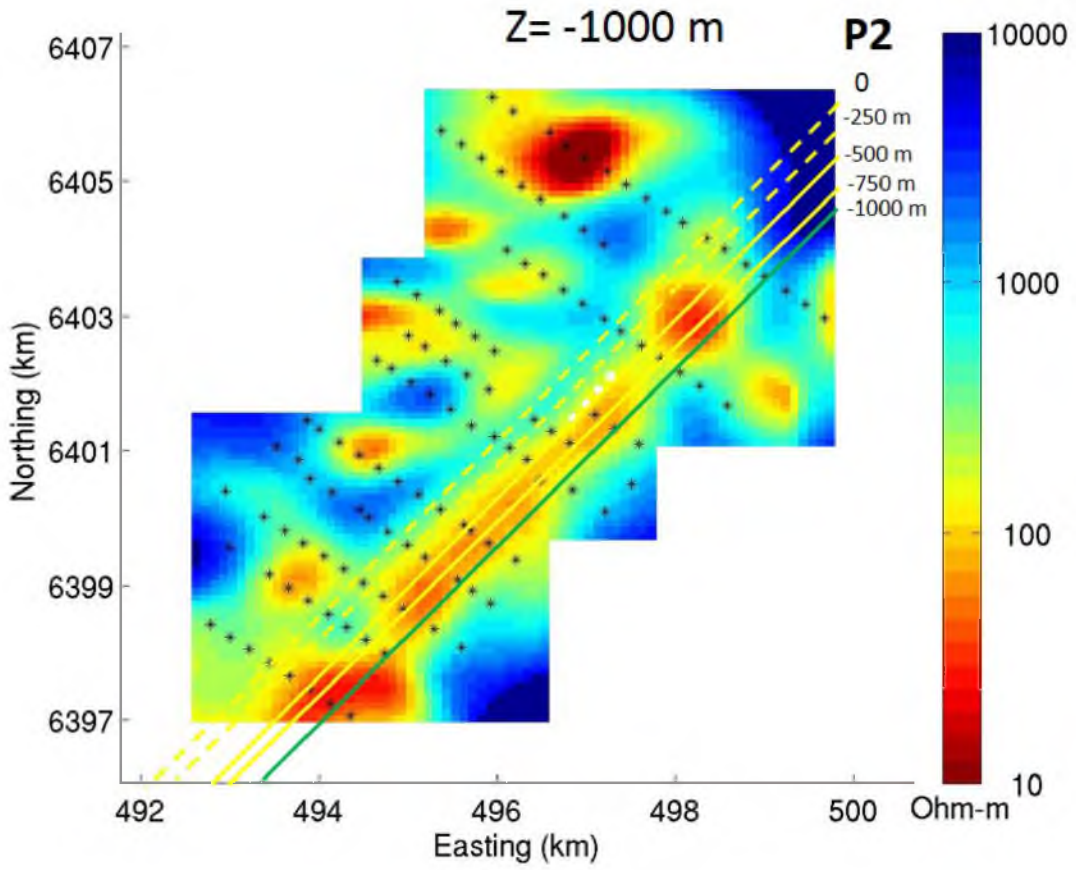


**Figure 6.13**. Horizontal slice of the inversion results located 1000 m below the surface. Below the unconformity, located approximately 500 m below the surface. The input data were the principal components, $Z_{xy}$ and $Z_{yx}$, of the McArthur River impedance tensor. The locations of the receivers are represented by the stars. The white dots represent the approximate location of the uranium ore pods, at about 500 m depth, where the mine is located. The apparent dip of the P2 fault is 35°. The dashed lines represent the inferred location of the fault with depth. The solid lines represent the known location of the fault due to drilling. The green line represents the current fault location. The yellow lines represent the fault location above the current depth (E. Petersen, personal communication, November 25, 2013). Notice several anomalously low conductive bodies in the northeast direction. They are due to the low resistive graphite in the P2 fault.

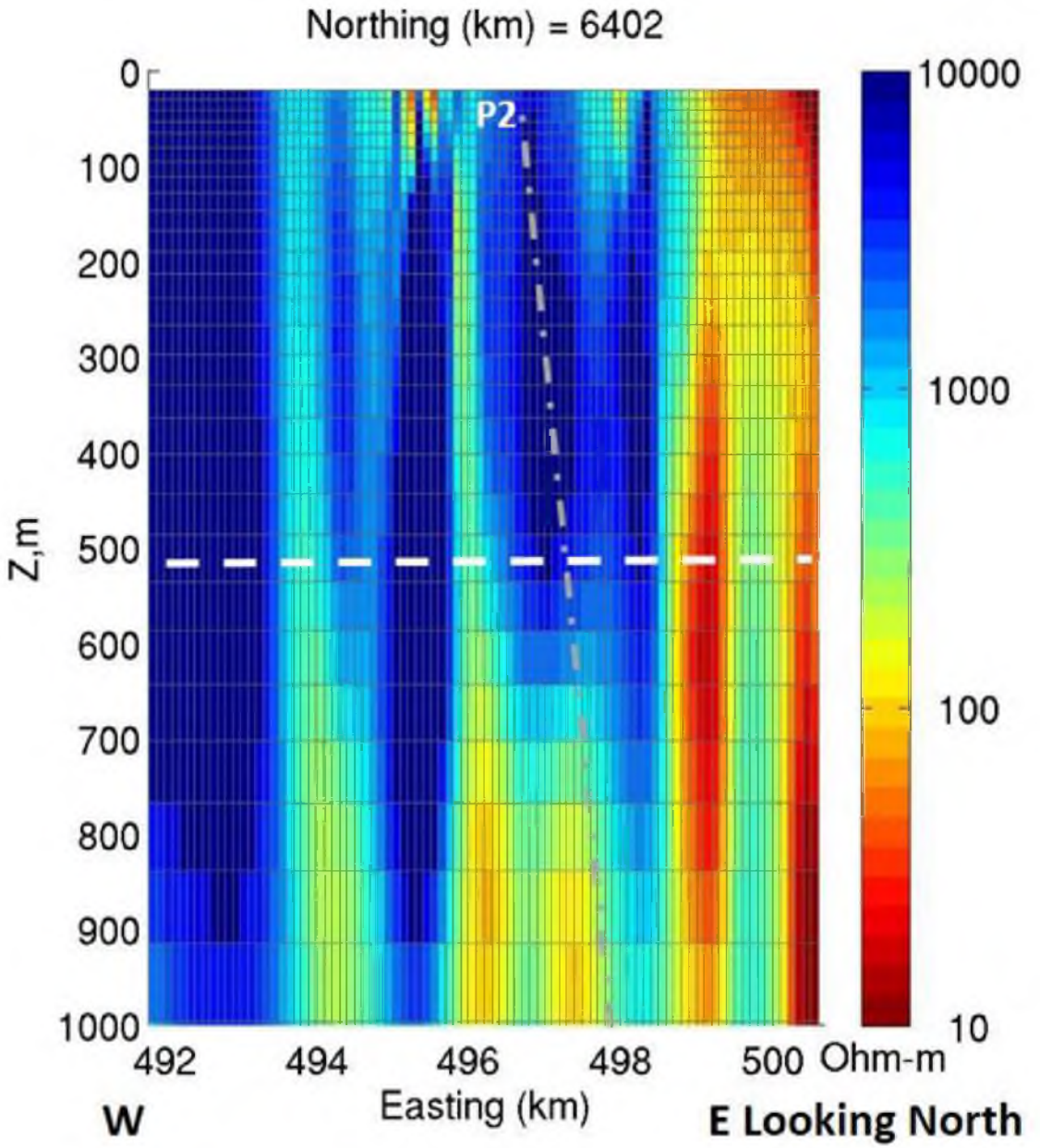


**Figure 6.14**. Vertical slice of the principal impedance, $Z_{xy}$ and $Z_{yx}$, inversion results in the north direction at 6402 km. The vertical axis is depth measured in meters, and the horizontal axis is the east direction with units of kilometers. The vertical axis has a scale 10 times larger than the horizontal axis. The very low conductivity on the far right side is believed to be edge effects. Notice how the anomalies correspond to the horizontal slices of the inversion results. Also notice that the anomalies near the surface may be caused by NSI. The gray dashed line represents the approximate location of the P2 fault. The white dashed line represents the approximate location of the unconformity.

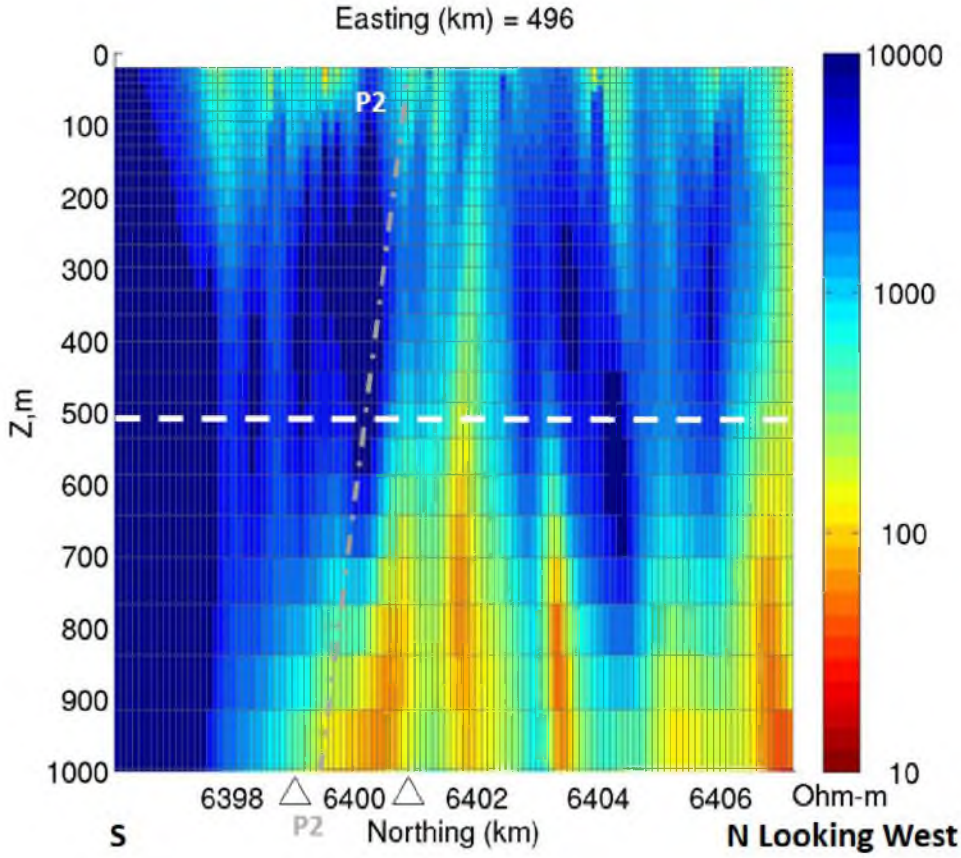


**Figure 6.15**. Vertical slice of the principal impedance, $Z_{xy}$ and $Z_{yx}$, inversion results in the east direction at 496 km. The vertical axis is depth measured in meters, and the horizontal axis is the north direction measured with units of kilometers. The vertical axis has a scale 10 times larger than the horizontal axis. Notice how the anomalies correspond to the horizontal slices of the inversion results. Also notice that the anomalies near the surface may be caused by NSI. The gray dashed line represents the approximate location of the P2 fault. The white dashed line represents the approximate location of the unconformity.

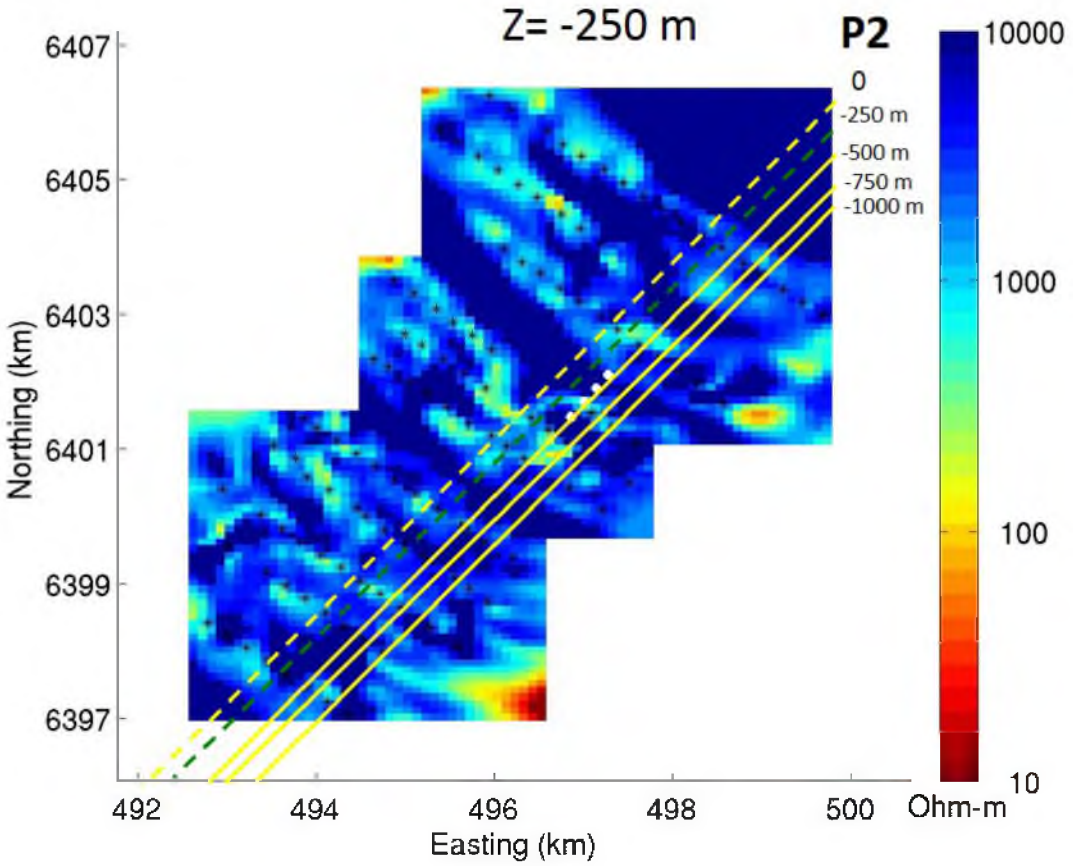


**Figure 6.16**. Horizontal slice of the inversion results located 250 m below the surface. Above the unconformity, located approximately 500 m below the surface. The input data were all the components, $Z_{xy}$, $Z_{yx}$, $Z_{xx}$, and $Z_{yy}$, of the McArthur River impedance tensor. The stars represent the locations of the receivers. The white dots represent the approximate location of the uranium ore pods, at about 500 m depth, where the mine is located. The apparent dip of the P2 fault is 35°. The dashed lines represent the inferred location of the fault with depth. The solid lines represent the known location of the fault due to drilling. The green line represents the current fault location. The yellow lines represent the fault location above and below the current depth (E. Petersen, personal communication, November 25, 2013). Notice that conductivity is very random and resistive, these are artifacts. These appear to be caused by the auxiliary components of the impedance tensor ($Z_{xx}$ and $Z_{yy}$) because they are not observed in the principal impedance inversion results (Figure 6.10). These artifacts could be caused by NSI and similar results are observed in Figure 5.23.

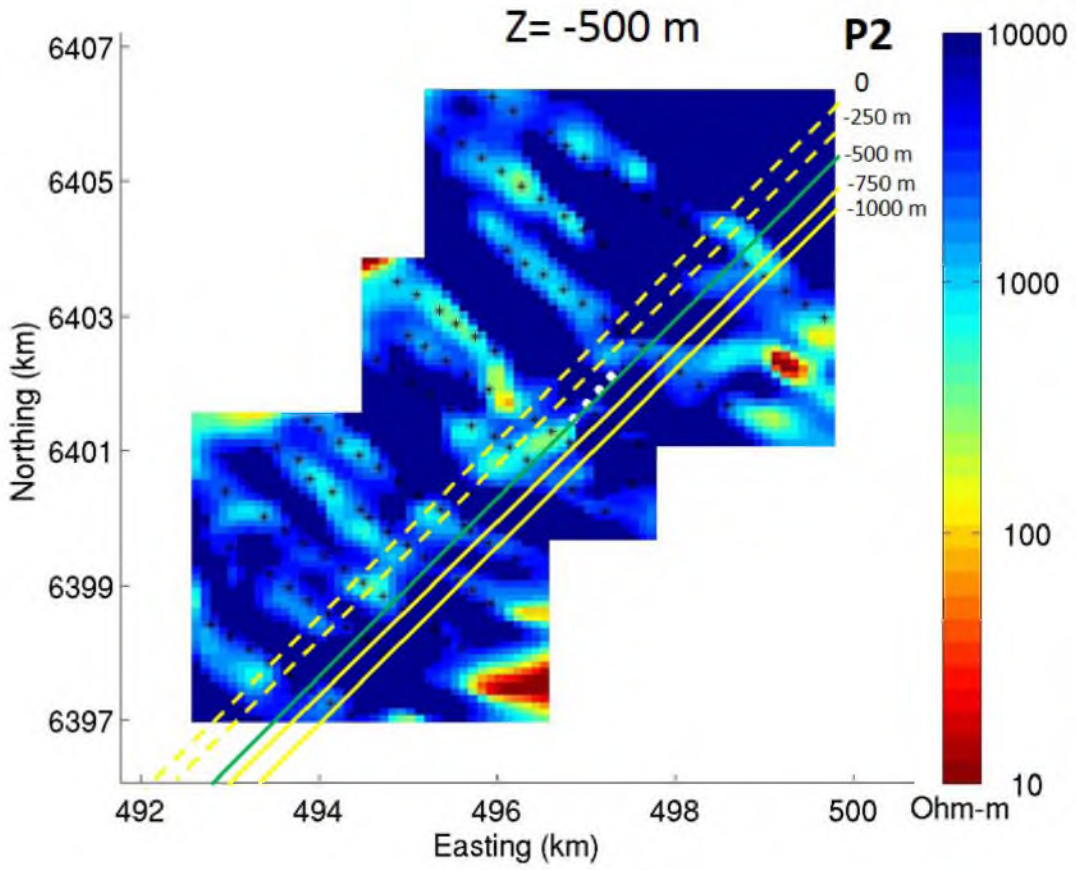


**Figure 6.17**. Horizontal slice of the inversion results located 500 m below the surface, the approximate location of the unconformity. The input data were all the components, $Z_{xy}$, $Z_{yx}$, $Z_{xx}$, and $Z_{yy}$, of the McArthur River impedance tensor. The stars represent the locations of the receivers. The white dots represent the approximate location of the uranium ore pods, at about 500 m depth, where the mine is located. The apparent dip of the P2 fault is 35°. The dashed lines represent the inferred location of the fault with depth. The solid lines represent the known location of the fault due to drilling. The green line represents the current fault location. The yellow lines represent the fault location above and below the current depth (E. Petersen, personal communication, November 25, 2013). The low resistivity anomalies are artifacts because there are no receivers above them. The anomalies directly below the receivers are also believed to be artifacts.

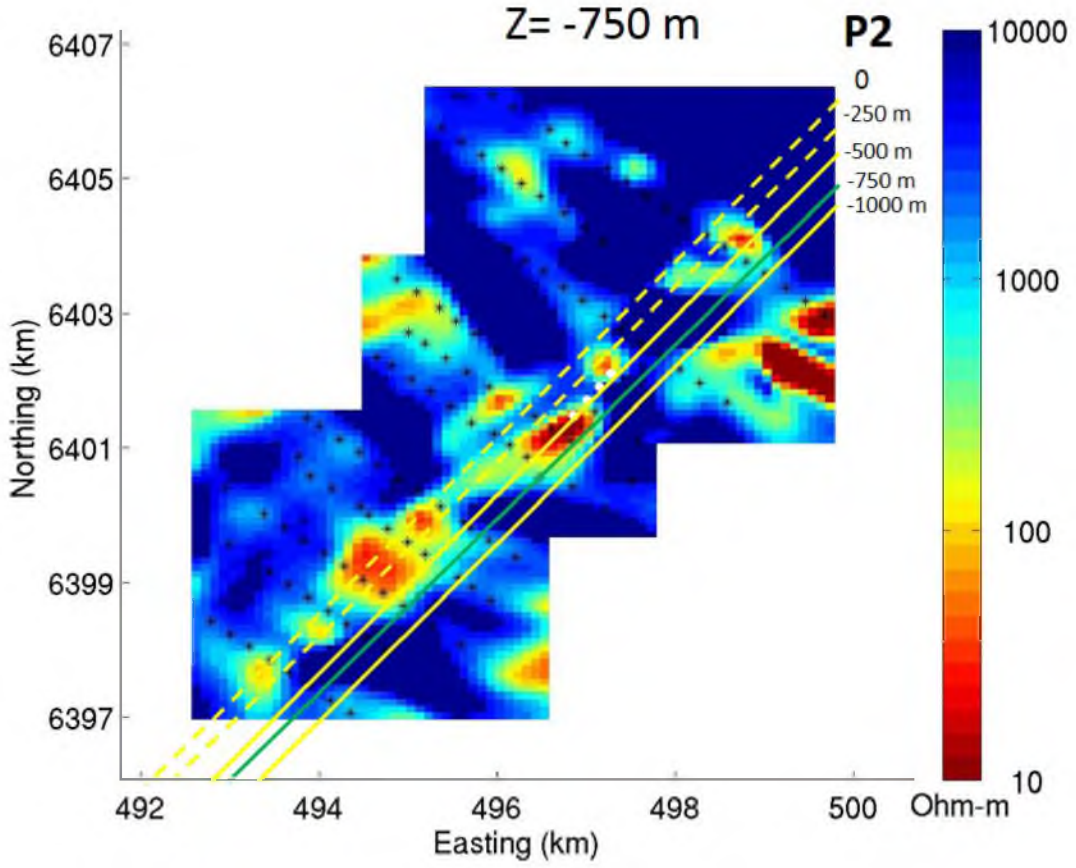


**Figure 6.18**. Horizontal slice of the inversion results located 750 m below the surface. Below the unconformity, located approximately 500 m below the surface. The input data were all the components, $Z_{xy}$, $Z_{yx}$, $Z_{xx}$, and $Z_{yy}$, of the McArthur River impedance tensor. The stars represent the location of the receivers. The white dots represent the approximate location of the uranium ore pods, at about 500 m depth, where the mine is located. The apparent dip of the P2 fault is 35°. The dashed lines represent the inferred location of the fault with depth. The solid lines represent the known location of the fault due to drilling. The green line represents the current fault location. The yellow lines represent the fault location above and below the current depth (E. Petersen, personal communication, November 25, 2013). The anomalies with low resistivity in the northeast direction are caused by the graphite located within the P2 fault.

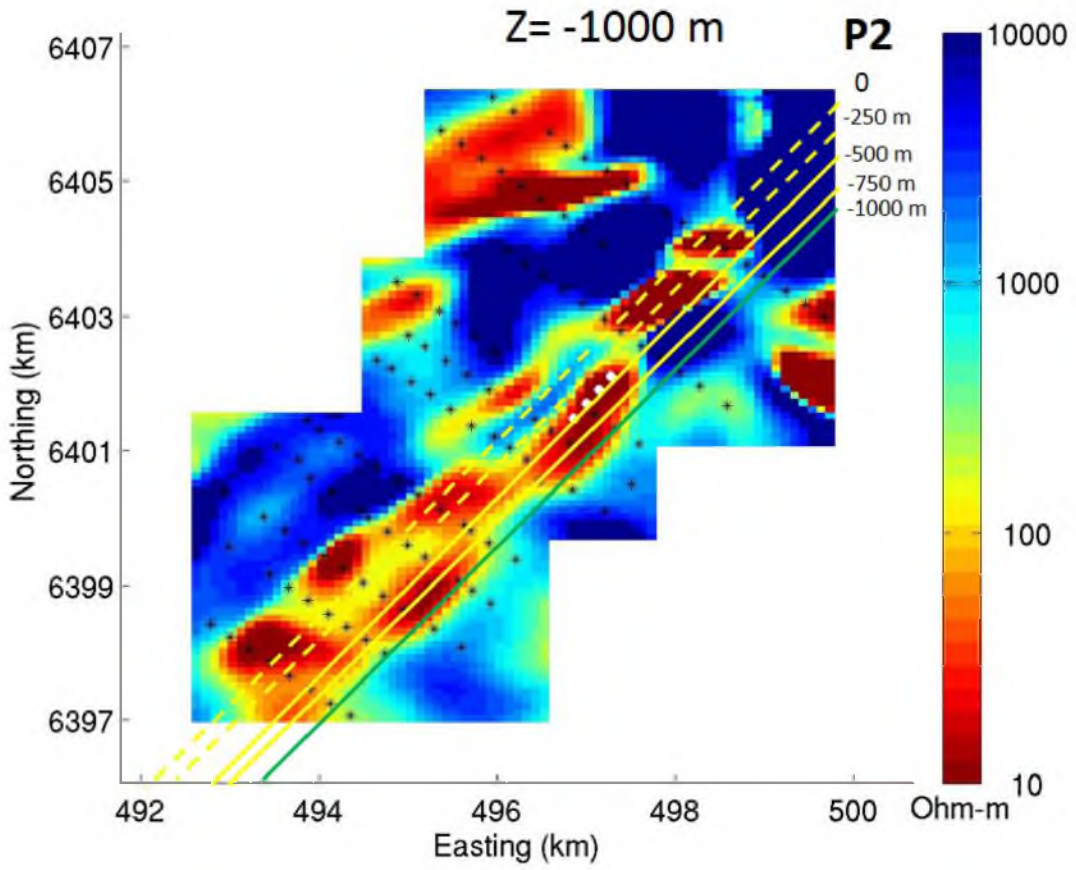


**Figure 6.19**. Horizontal slice of the inversion results located 1000 m below the surface. Below the unconformity, located approximately 500 m below the surface. The input data were all the components, $Z_{xy}$, $Z_{yx}$, $Z_{xx}$, and $Z_{yy}$, of the McArthur River impedance tensor. The stars represent the locations of the receivers. The white dots represent the approximate location of the uranium ore pods, at about 500 m depth, where the mine is located. The apparent dip of the P2 fault is 35°. The dashed lines represent the inferred location of the fault with depth. The solid lines represent the known location of the fault due to drilling. The green line represents the current fault location. The yellow lines represent the fault location above the current depth (E. Petersen, personal communication, November 25, 2013). The anomaly in the northeast direction that is very low resistivity is due to the graphite in the P2 fault. If there is no receivers below an anomaly it is very likely that it is an artifact.

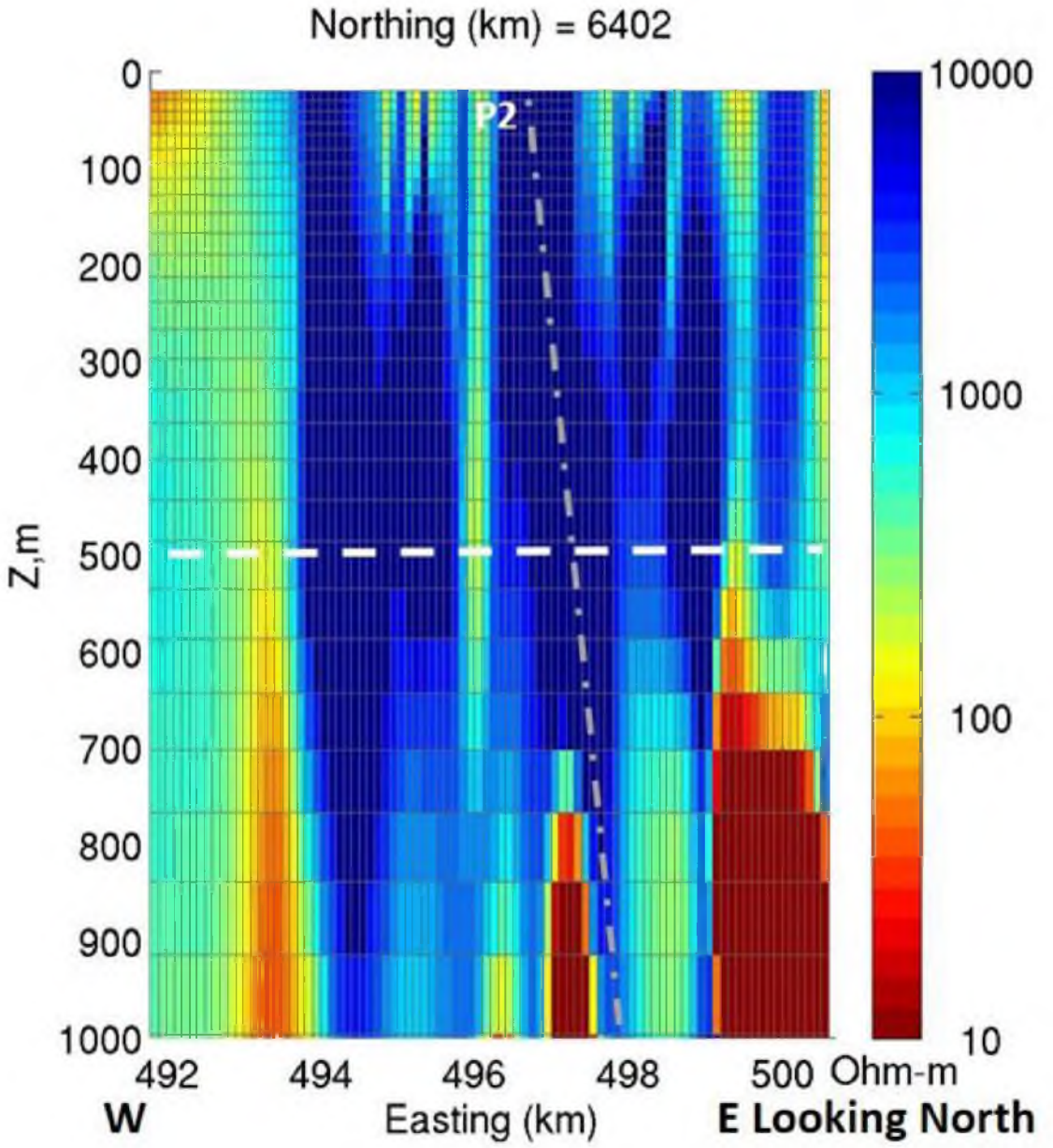


**Figure 6.20**. Vertical slice of the full impedance, $Z_{xx}$ $Z_{yy}$ $Z_{xy}$ and $Z_{yx}$, inversion results in the north direction at 6402 km. The vertical axis is depth measured in meters, and the horizontal axis is the east direction measured with units of kilometers. The vertical axis has a scale 10 times larger than the horizontal axis. The very low conductivity on the far right side is believed to be edge effects. Notice how the anomalies correspond to the horizontal slices of the inversion results. Also notice that the anomalies near the surface may be caused by NSI. The gray dashed line represents the approximate location of the P2 fault. The white dashed line represents the approximate location of the unconformity.

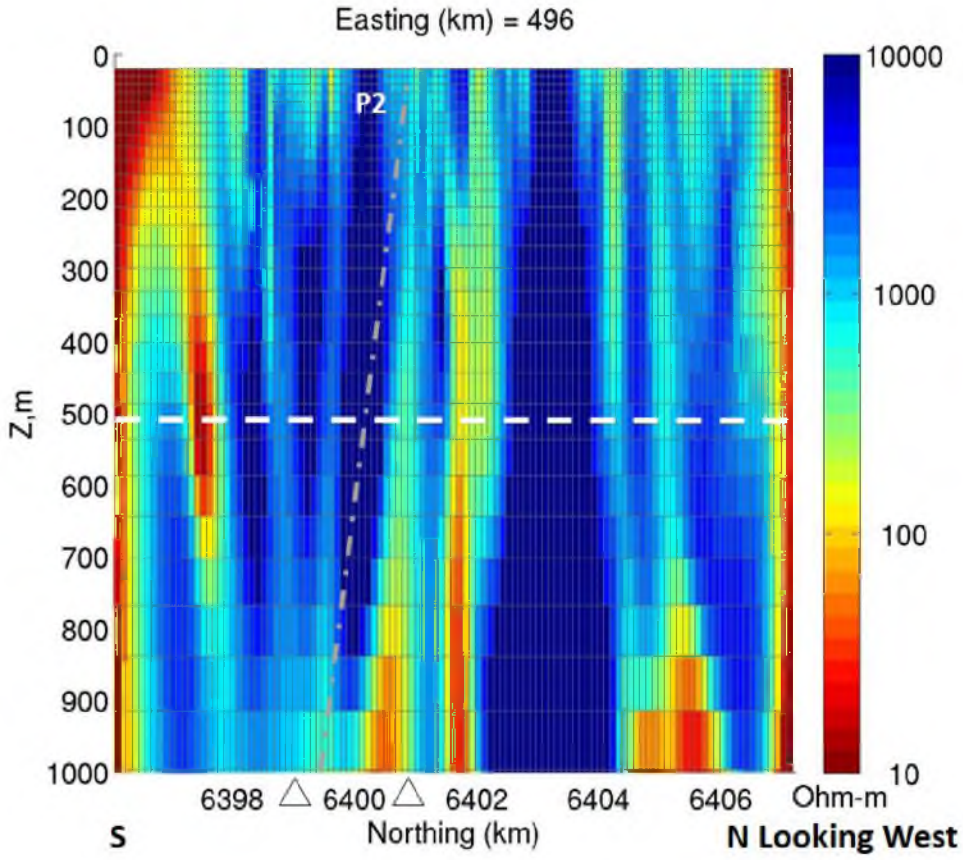


**Figure 6.21**. Vertical slice of the full impedance, $Z_{xx}$ $Z_{yy}$ $Z_{xy}$ and $Z_{yx}$, inversion results in the east direction at 496 km. The vertical axis is depth measured in meters, and the horizontal axis is the north direction measured with units of kilometers. The vertical axis has a scale 10 times larger than the horizontal axis. The very low conductivity on the far left and right sides is believed to be edge effects. Notice how the anomalies correspond to the horizontal slices of the inversion results. Also notice that the anomalies near the surface may be caused by NSI. The gray dashed line represents the approximate location of the P2 fault. The white dashed line represents the approximate location of the unconformity.

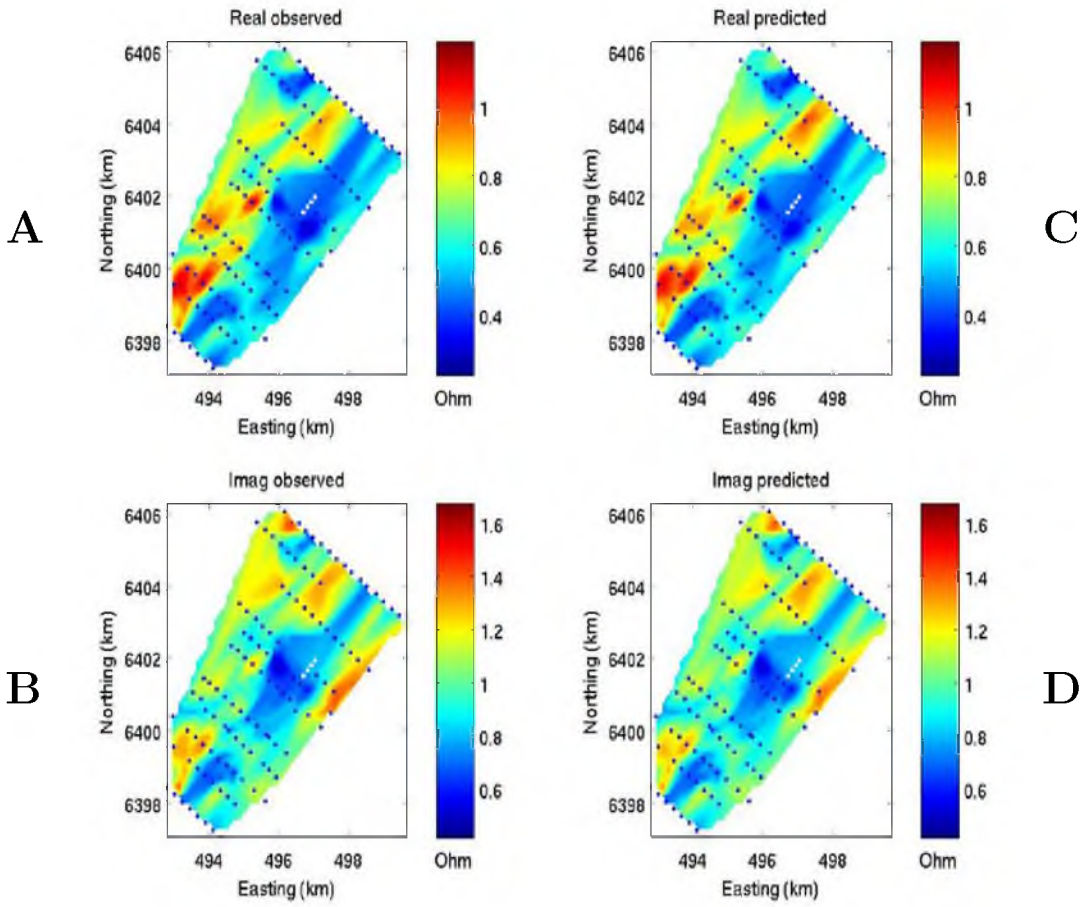


**Figure 6.22**. McArthur River data observed and predicted maps of $Z_{xy}$ at 97 Hz taken from the full impedance inversion. Parts A) and B) show the real and imaginary parts of observed data, respectively. Parts C) and D) show the real and imaginary parts of the predicted data, respectively. The dots represent the location of the receivers. The white dots represent the approximate location of the uranium ore pods, at about 500 m depth, where the mine is located.

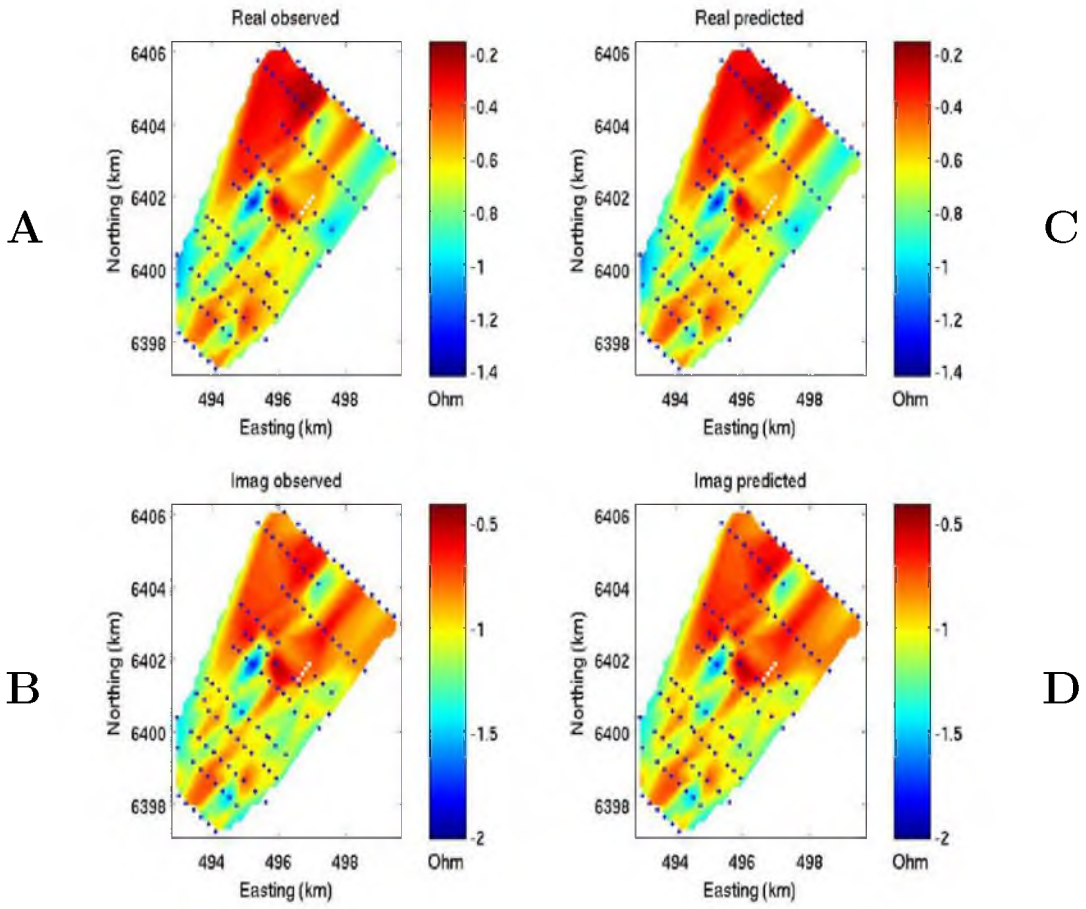


**Figure 6.23**. McArthur River data observed and predicted maps of $Z_{yx}$ at 97 Hz taken from the full impedance inversion. Parts A) and B) show the real and imaginary parts of observed data, respectively. Parts C) and D) show the real and imaginary parts of the predicted data, respectively. The dots represent the location of the receivers. The white dots represent the approximate location of the uranium ore pods, at about 500 m depth, where the mine is located.

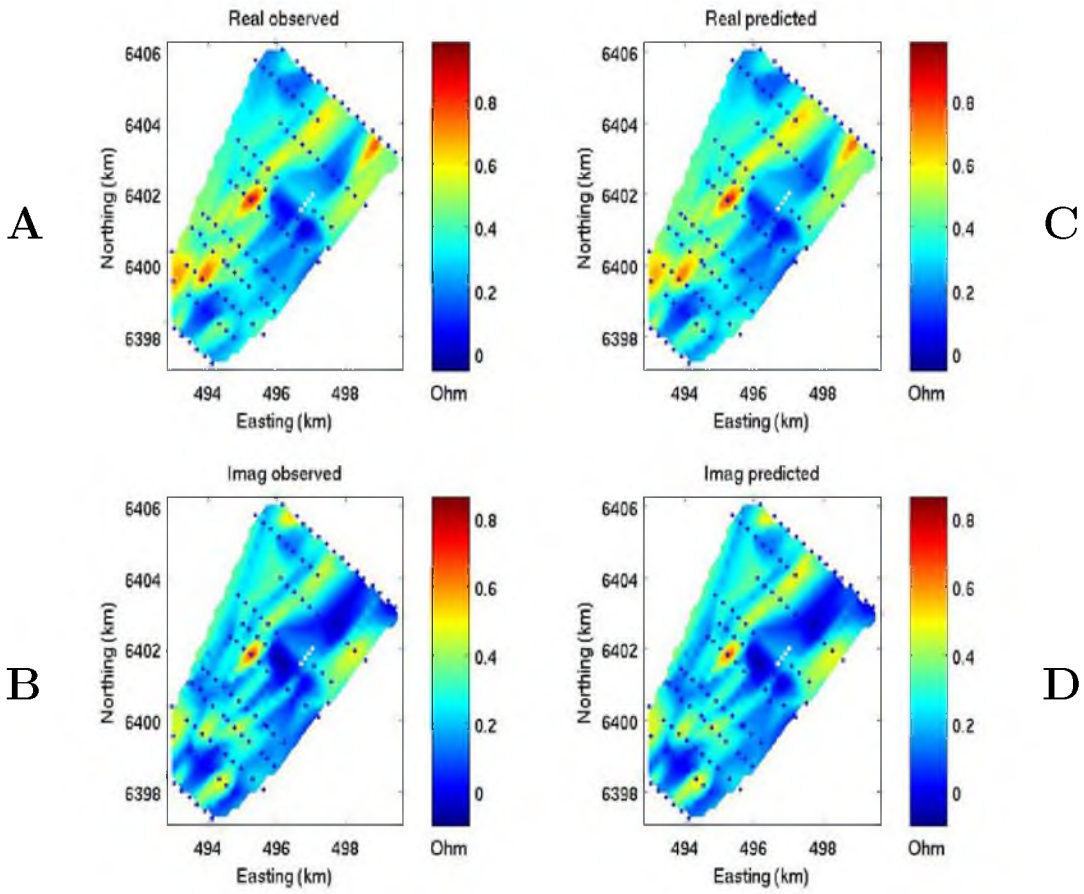


**Figure 6.24**. McArthur River data observed and predicted maps of $Z_{xx}$ at 97 Hz taken from the full impedance inversion. Parts A) and B) show the real and imaginary parts of observed data, respectively. Parts C) and D) show the real and imaginary parts of the predicted data, respectively. The dots represent the location of the receivers. The white dots represent the approximate location of the uranium ore pods, at about 500 m depth, where the mine is located.

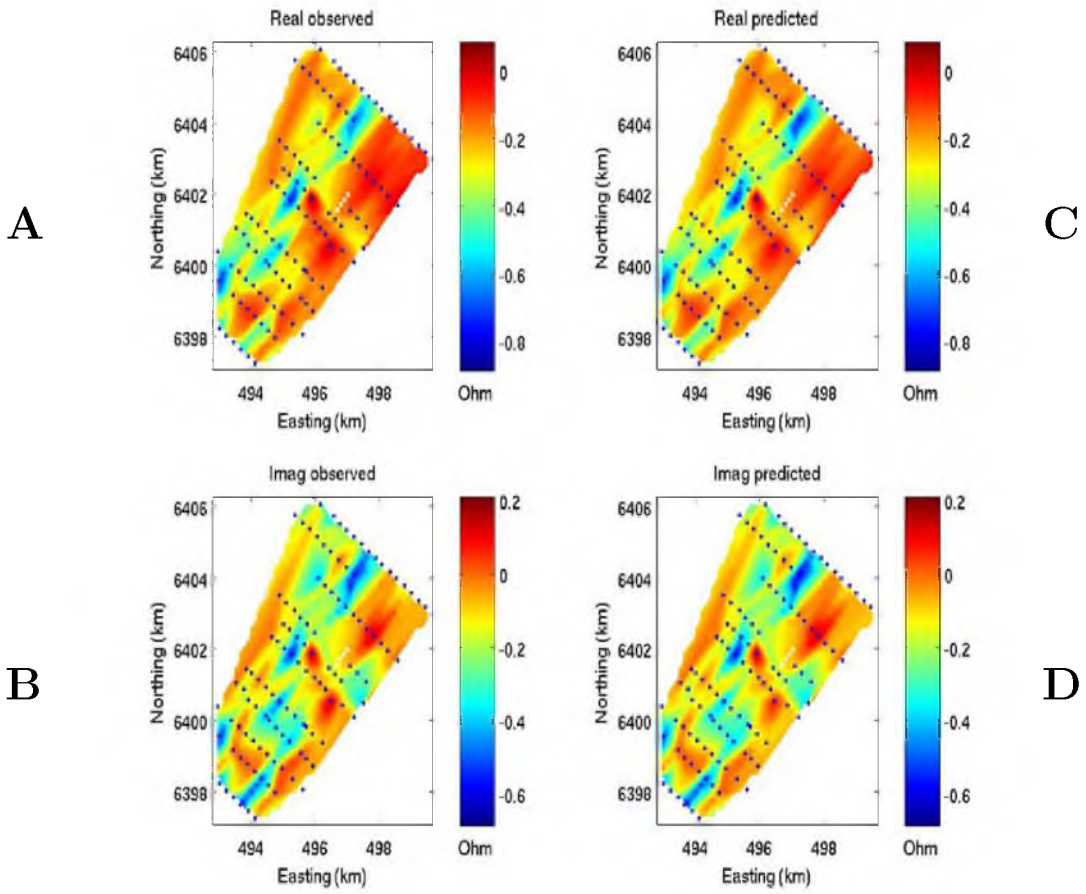


**Figure 6.25**. McArthur River data observed and predicted maps of $Z_{yy}$ at 97 Hz taken from the full impedance inversion. Parts A) and B) show the real and imaginary parts of observed data, respectively. Parts C) and D) show the real and imaginary parts of the predicted data, respectively. The dots represent the location of the receivers. The white dots represent the approximate location of the uranium ore pods, at about 500 m depth, where the mine is located.

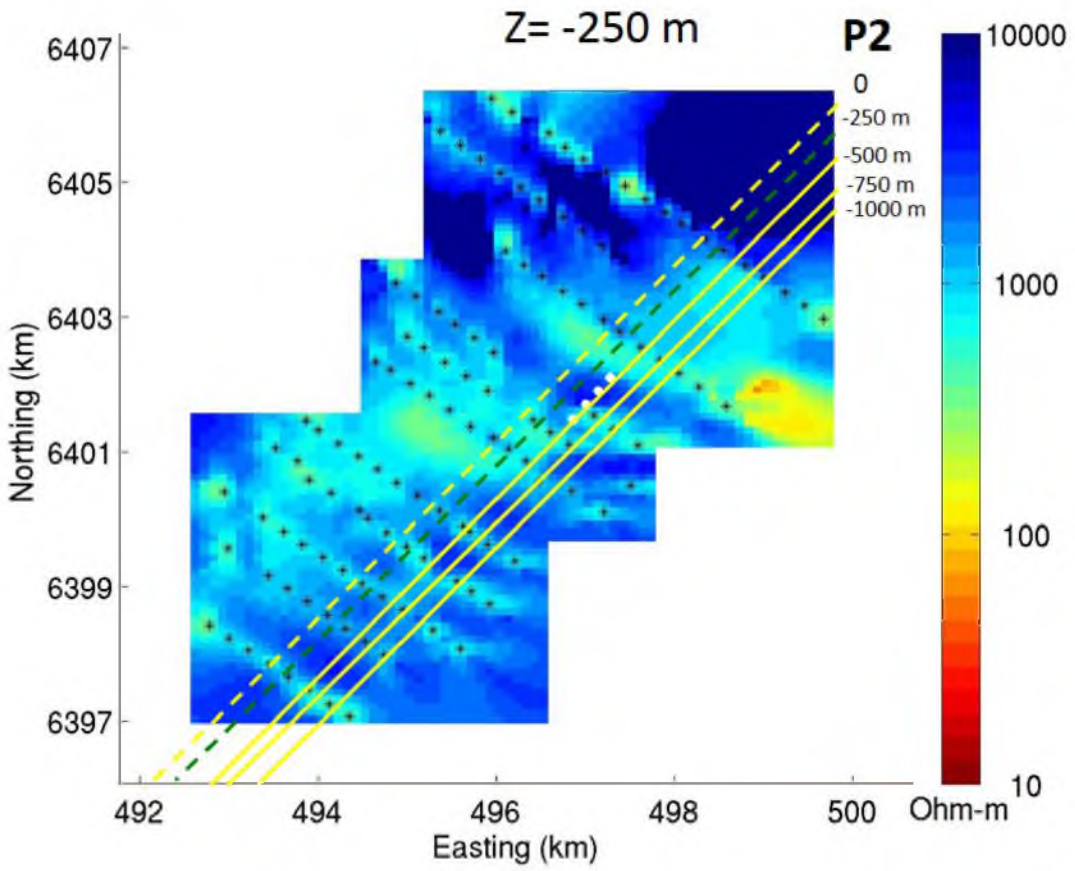


**Figure 6.26**. Horizontal slice of the inversion results located 250 m below the surface. Above the unconformity, located approximately 500 m below the surface. The input data were the principal components, $\Phi_{xx}$ and $\Phi_{yy}$, of the McArthur River phase tensor. Notice that the resistivity is fairly homogenous, similar to the background conductivity with small anomalies. The stars represent the location of the receivers. The white dots represent the approximate location of the uranium ore pods, at about 500 m depth, where the mine is located. The apparent dip of the P2 fault is 35°. The dashed lines represent the inferred location of the fault with depth. The solid lines represent the known location of the fault due to drilling. The green line represents the current fault location. The yellow lines represent the fault location above and below the current depth (E. Petersen, personal communication, November 25, 2013).

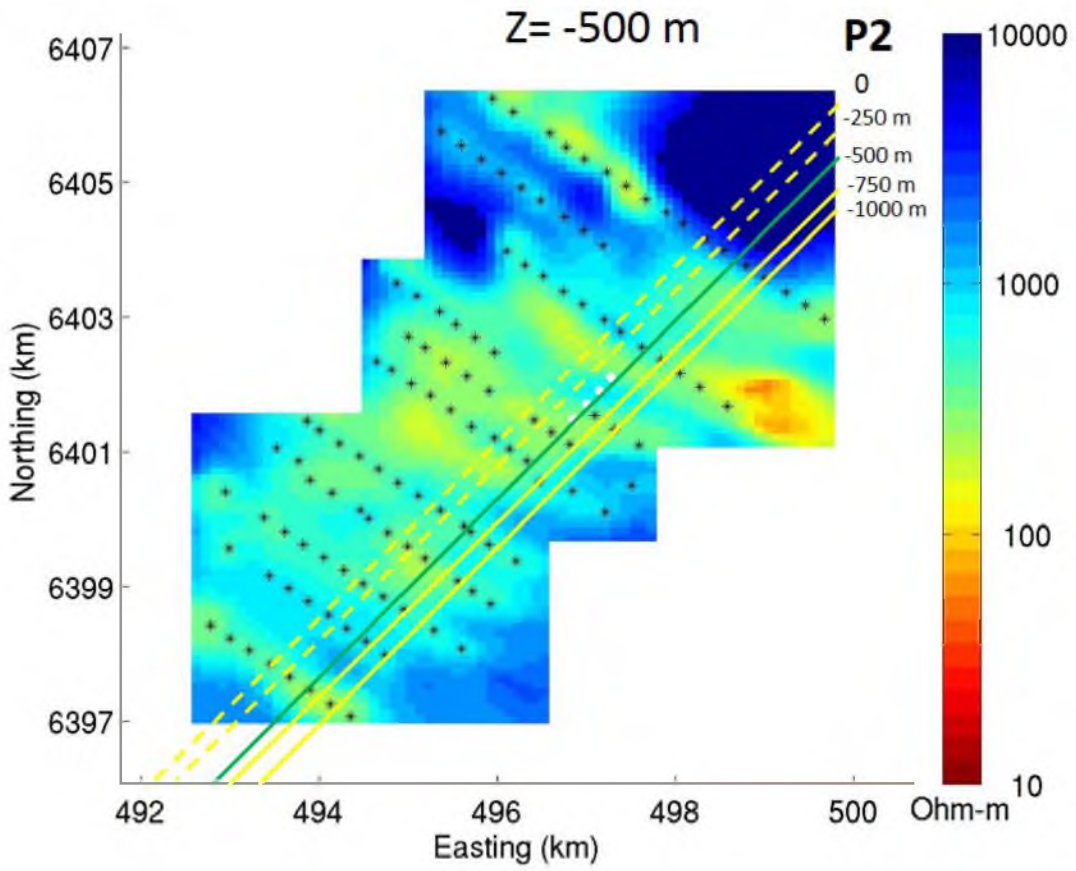


**Figure 6.27**. Horizontal slice of the inversion results located 500 m below the surface, the approximate location of the unconformity. The input data were the principal components, $\Phi_{xx}$ and $\Phi_{yy}$, of the McArthur River phase tensor. Notice that there is a large anomaly with a lower resistivity. The cause of this is unknown, and it might be an artifact. The stars represent the location of the receivers. The white dots represent the approximate location of the uranium ore pods, at about 500 m depth, where the mine is located. The apparent dip of the P2 fault is 35°. The dashed lines represent the inferred location of the fault with depth. The solid lines represent the known location of the fault due to drilling. The green line represents the current fault location. The yellow lines represent the fault location above and below the current depth (E. Petersen, personal communication, November 25, 2013).

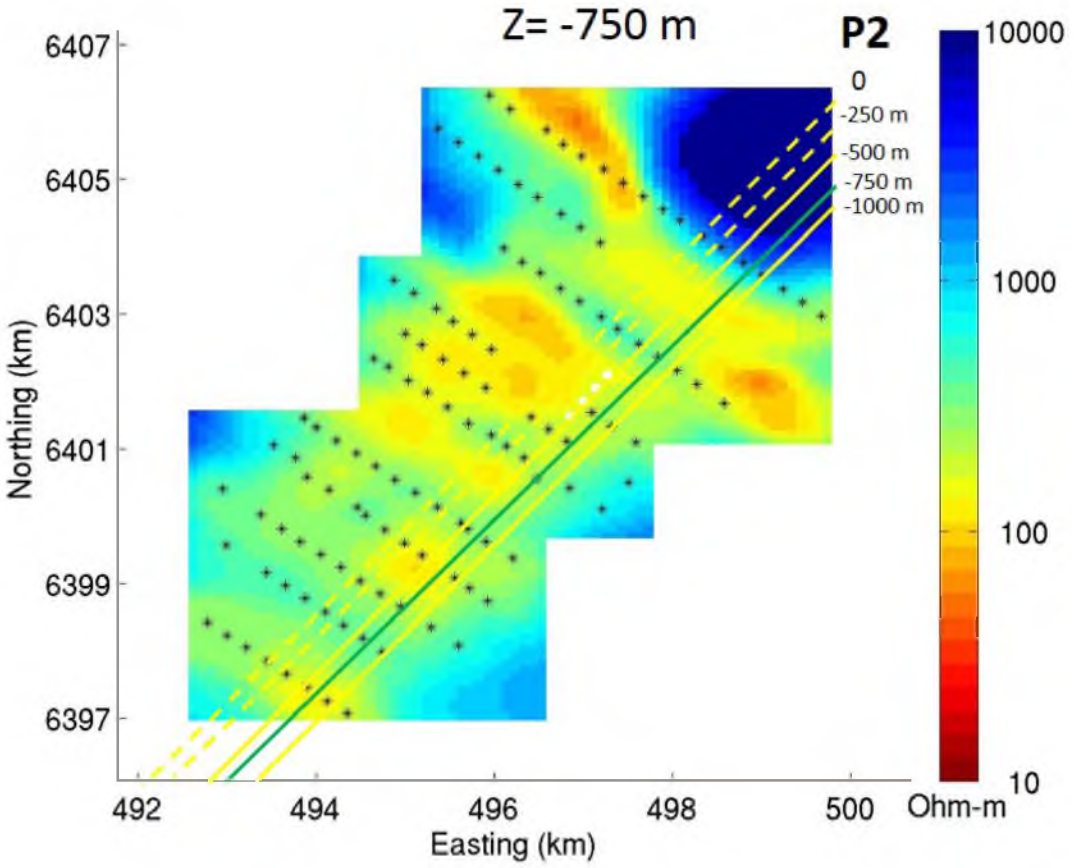


**Figure 6.28**. Horizontal slice of the inversion results located 750 m below the surface. Below the unconformity, located approximately 500 m below the surface. The input data were the principal components, $\Phi_{xx}$ and $\Phi_{yy}$, of the McArthur River phase tensor. Notice that there are several anomalies near the center. The stars represent the location of the receivers. The white dots represent the approximate location of the uranium ore pods, at about 500 m depth, where the mine is located. The apparent dip of the P2 fault is 35°. The dashed lines represent the inferred location of the fault with depth. The solid lines represent the known location of the fault due to drilling. The green line represents the current fault location. The yellow lines represent the fault location above and below the current depth (E. Petersen, personal communication, November 25, 2013).

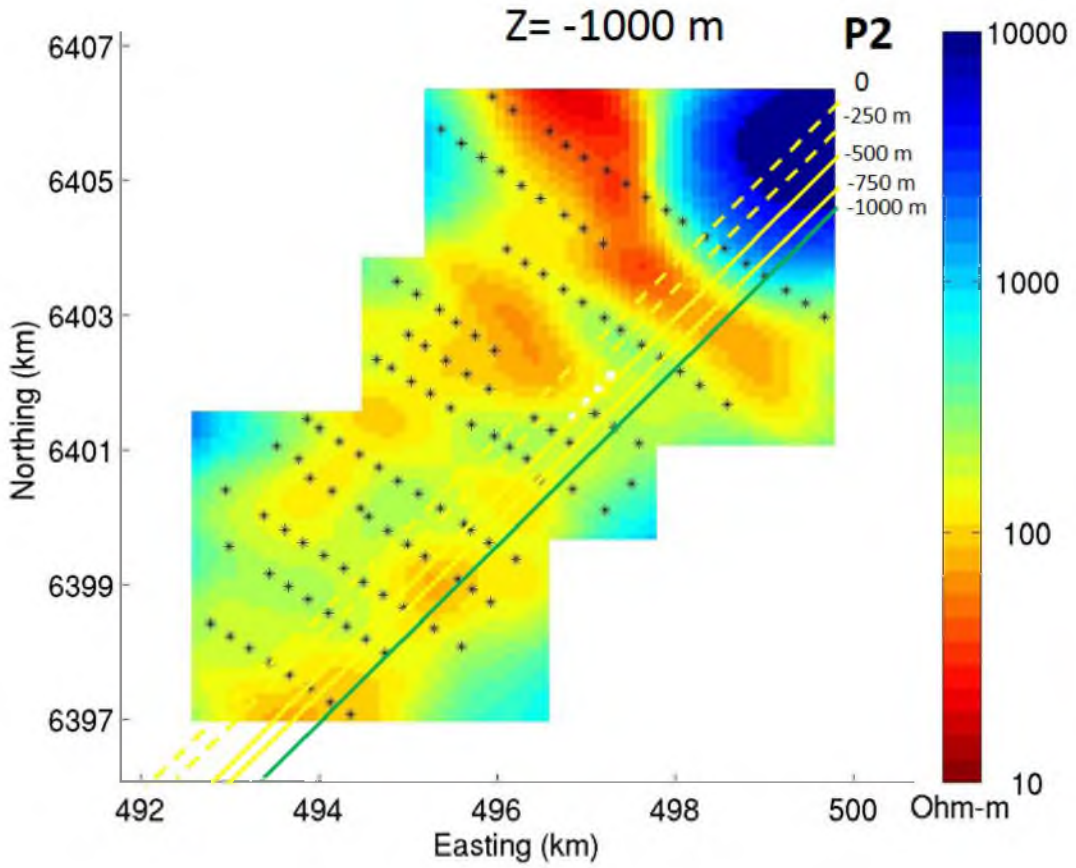


**Figure 6.29**. Horizontal slice of the inversion results located 1000 m below the surface. Below the unconformity, located approximately 500 m below the surface. The input data were the principal components, $\Phi_{xx}$ and $\Phi_{yy}$, of the McArthur River phase tensor. Notice there are several anomalies that are trending in the northwest direction. This does not appear to match the graphite trend in the northeast direction. The stars represent the location of the receivers. The white dots represent the approximate location of the uranium ore pods, at about 500 m depth, where the mine is located. The apparent dip of the P2 fault is 35°. The dashed lines represent the inferred location of the fault with depth. The solid lines represent the known location of the fault due to drilling. The green line represents the current fault location. The yellow lines represent the fault location above the current depth (E. Petersen, personal communication, November 25, 2013).

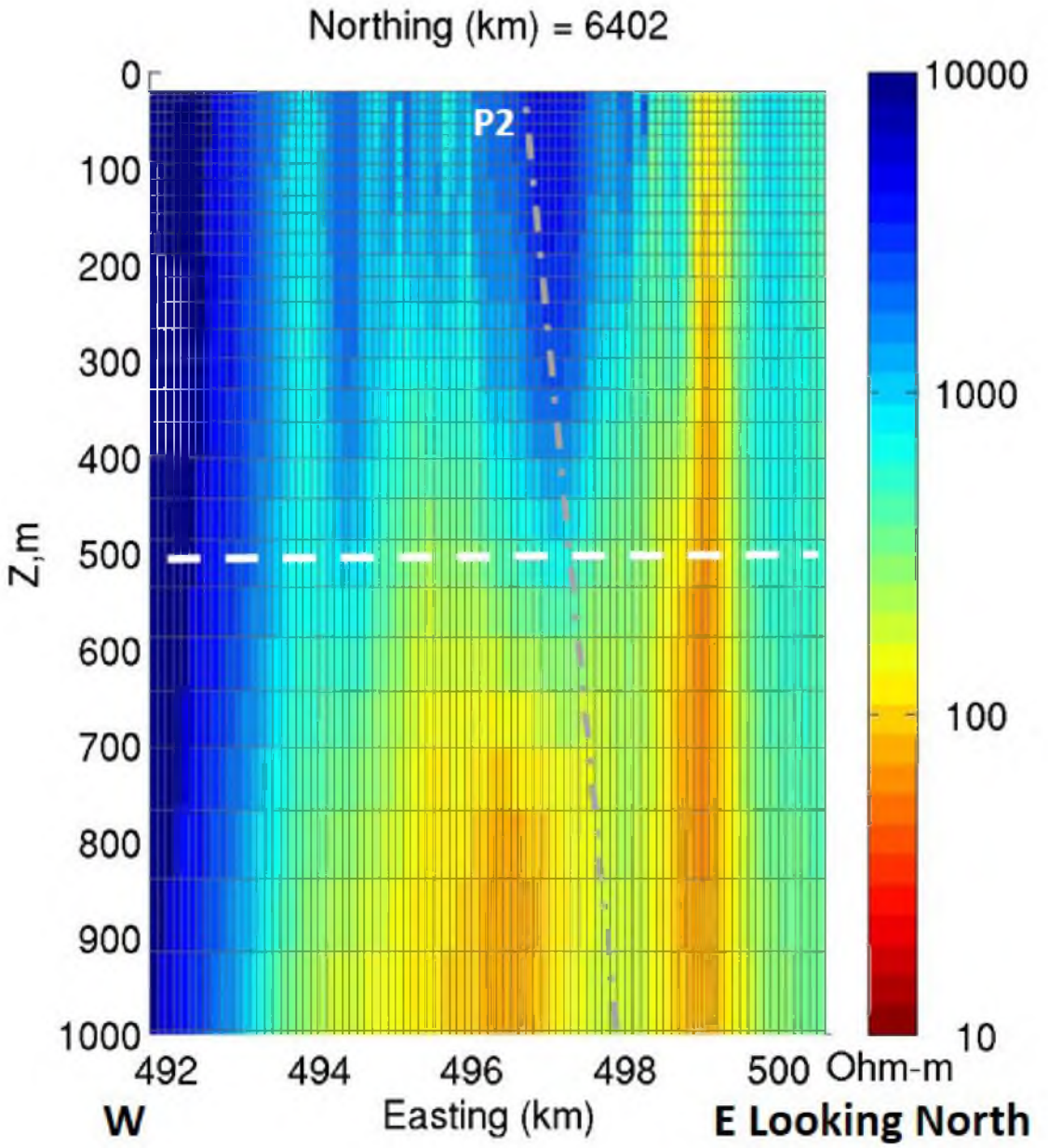


**Figure 6.30**. Vertical slice of the principal phase tensor, $\Phi_{xx}$ and $\Phi_{yy}$, inversion results in the north direction at 6402 km. The vertical axis is depth measured in meters, and the horizontal axis is the east direction measured with units of kilometers. The vertical axis has a scale 10 times larger than the horizontal axis. Notice how the anomalies correspond to the horizontal slices of the inversion results. The gray dashed line represents the approximate location of the P2 fault. The white dashed line represents the approximate location of the unconformity.

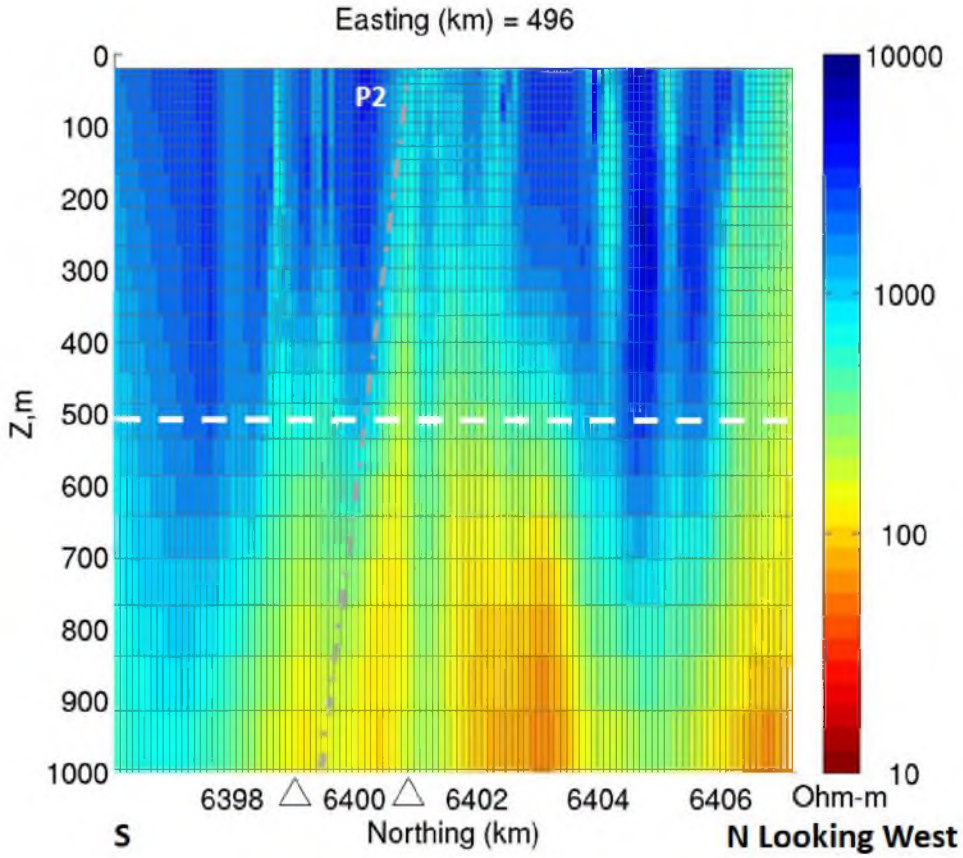


**Figure 6.31**. Vertical slice of the principal phase tensor, $\Phi_{xx}$ and $\Phi_{yy}$, inversion results in the east direction at 496 km. The vertical axis is depth measured in meters, and the horizontal axis is the north direction measured with units of kilometers. The vertical axis has a scale 10 times larger than the horizontal axis. Notice how the anomalies correspond to the horizontal slices of the inversion results. The grey dashed line represents the approximate location of the P2 fault. The white dashed line represents the approximate location of the unconformity.

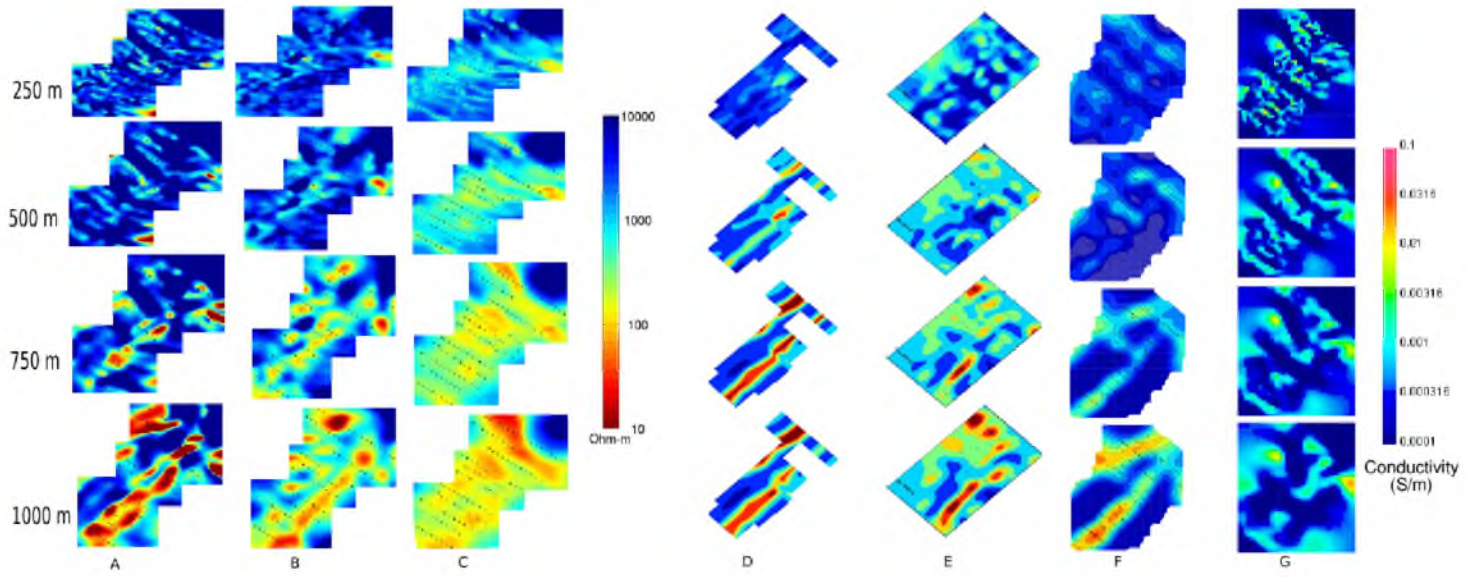


**Figure 6.32**. The inversion results of the McArthur river MT data set using different methods all compared using one figure. The rows represent the same depths, and the columns represent the same inversion results for individual tests. Column A used the all the components of the impedance tensor (xy, yx, xx, yy) for inversion. Column B used the principal components of the impedance tensor (xy, yx) for inversion. Column C used the principal components of the phase tensor (xx, yy) in the inversion. Columns A, B, and C all used the same data set and algorithm described in Zhdanov et al. (2011). Column D represent 2D inversion results from V. Tuncer (modified from Craven et al., 2006) which used the principal components of impedance (xy, yx) and the tipper or Z component of the magnetic field in inversion. Column E represents the 3D inversion results from W. Siripunvaraporn (modified from Craven et al., 2006) which also used the principal components of impedance (xy, yx) in inversion. Column F represents the 3D inversion results from R. L. Mackie (modified from Craven et al., 2006) which used all the components of the impedance tensor (xy, yx, xx, yy) and tipper or Z component of the magnetic field in inversion. Column G represents the 3D inversion results from C. G. Farquharson (modified from Craven et al., 2006) which also used all the components of the impedance tensor in the inversion.

# CHAPTER 7

# CONCLUSIONS

A major problem in MT data is galvanic distortions due to near-surface inhomogeneities. The phase tensor introduced by Caldwell et al. (2004) was designed to overcome these distortions. In this thesis, 3D inversion was done using the phase tensor to see if the phase tensor would work to remove effects due to NSI, and create physically-meaningful models of the subsurface resistivity. Synthetic inversion using the impedance and phase tensor was done which showed potential for the phase tensor to work. A MT data set from the McArthur River was also inverted to test this method. The inversion results from this thesis were compared with the results from Craven et al. (2006), which used the same data set and different inversion algorithms (Figure 6.33). The results show that the phase tensor is not an effective means for inverting MT data in this case. One possible reason the phase tensor does not work is the auxiliary components are used with the principal components to calculate the components of the phase tensor. The auxiliary components are much more susceptible to noise and therefore they contaminate the principal components, and produce phase tensor values that are contaminated by this noise.

In summary, the impedance inversion results of this thesis compare well with results from three different publications and with the low resistivity of the subsurface. Also, the inversion results from Tuncer et al. (2006) were compared with borehole data from Mwenifumbo et al. (2004) and they matched well. The very good comparison between inversion models and correlation to borehole data are good indicators that the impedance results of this thesis are correct, and the inversion algorithm is working properly. The fact that the resistivity anomaly from the phase tensor is not similar to the other results is a good indicator that it does not work properly for 3D inversion in this case. For future work it would be interesting to test the phase tensor using a

different data set to see if it works properly. One other interesting study would be to obtain more borehole data and correlate it to the inversion results of impedance to test the accuracy of the impedance method.

# APPENDIX

# OBSERVED AND PREDICTED DATA MAPS

Figure A.1 shows that the predicted data match the observed data very well when full impedance inversion is done. Figure A.2 shows that the predicted data does not match the observed data very well at all when the full phase tensor is inverted. Figure A.3 shows that the principal phase tensor predicted data match the observed data fairly well. The principal phase tensor observed and predicted data match is better than the results from the full phase tensor inversion, but they are not as good as the full impedance results.

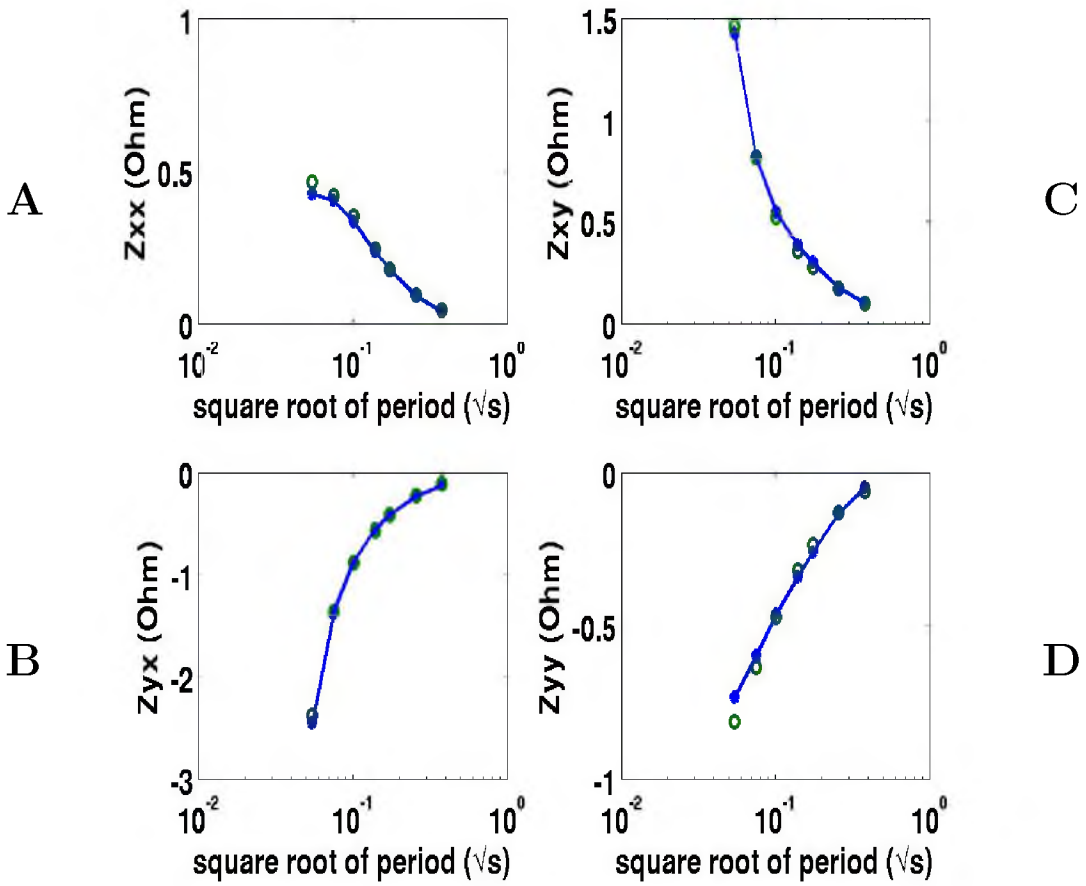


**Figure A.1**. Observed full impedance data from the McArthur River data set shown by the blue dots. The predicted data, after full impedance tensor inversion, are represented by the green circles. Parts A), B), C), and D) represent $Z_{xx}$, $Z_{yx}$, $Z_{xy}$, and $Z_{yy}$, respectively. Notice that the predicted data matches the observed data for all of the components of the impedance tensor. The location of this receiver is 494345 mE, 6397062 mN using UTM coordinates.

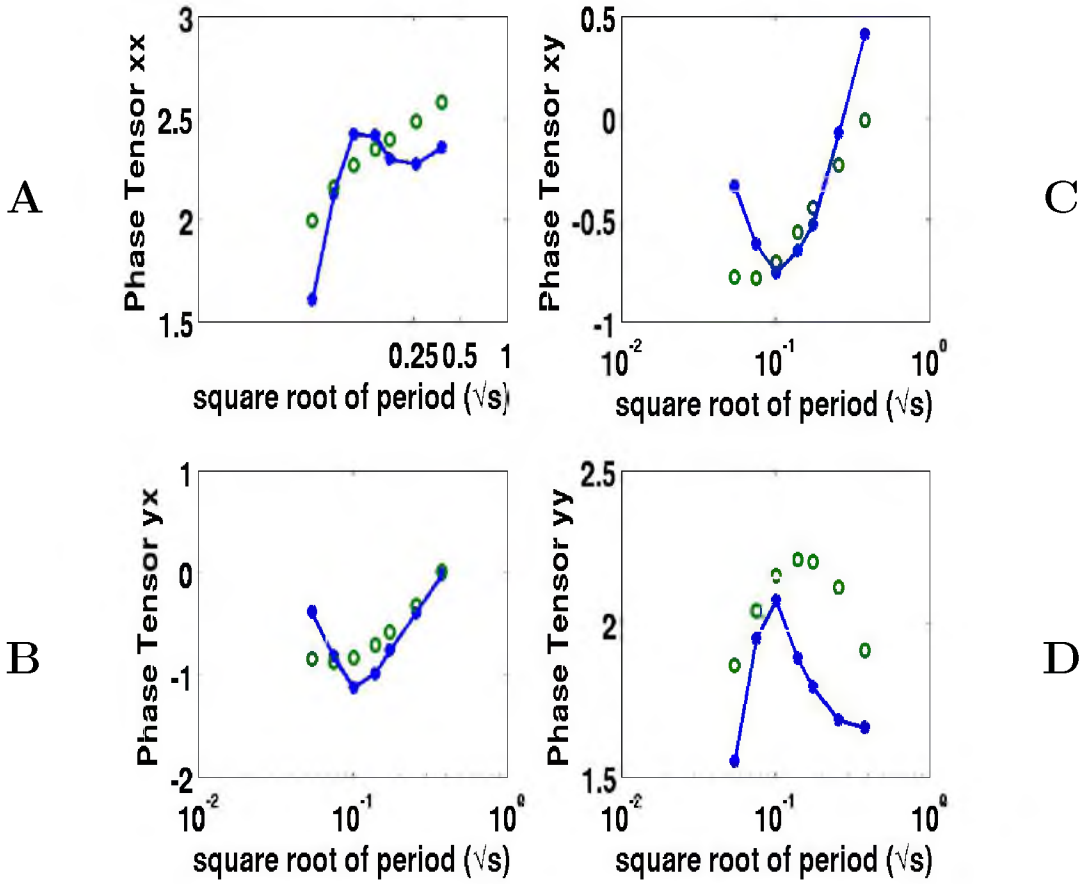


**Figure A.2**. Observed full phase tensor data from the McArthur River data set shown by the blue dots. The predicted data, after full phase tensor inversion, are represented by the green circles. Parts A), B), C), and D) represent xx, yx, xy, and yy, components of the phase tensor, respectively. Notice that the predicted data do not match the observed data for all of the components of the impedance tensor. The location of this receiver is 494345 mE, 6397062 mN using UTM coordinates.

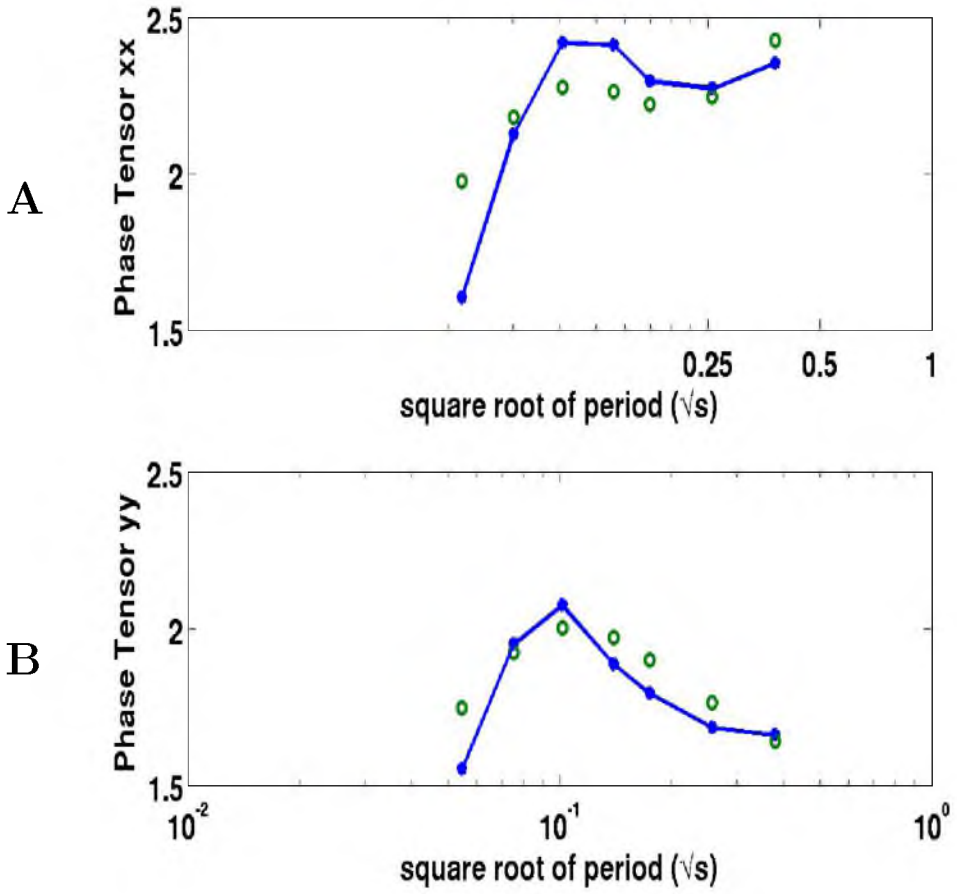


**Figure A.3**. Observed principal phase tensor data from the McArthur River data set shown by the blue dots. The predicted data, after principal phase tensor inversion, are represented by the green circles. Parts A) and B) represent xx and yy components of the phase tensor. Notice that the predicted data matches the observed data fairly well when using the principal components of the phase tensor. The results are better than the full phase tensor results, but worse than the full impedance tensor. The location of this receiver is 494345 mE, 6397062 mN using UTM coordinates

# REFERENCES


Berdichevsky, M. N., Dmitriev, V. I., 1976a. Distortions of magnetic and eletrical fields by near-surface lateral inhomogeneities. Acta Geodaetica, Geophysica et Monatanista, Akademy of Science Hungary 34 (11), 447–483.

Berdichevsky, M. N., Dmitriev, V. I., 1976b. Basic principles of interpretation of magnetotelluric sounding curves. In: Adam, A. (Ed.), Geoelectric and Geothermal Studies. KAPG Geophysical Monograph, Akademiai Kiado, pp. 165–221.

Berdichevsky, M. N., Dmitriev, V. I., 2002. Magnetotellurics in the context of the theory of ill-posed problems. Society of Exploration Geophysics, USA.

Berdichevsky, M. N., Vanyan, L. L., Dmitriev, V. I., 1989. Methods used in the U.S.S.R. to reduce near-surface inhomogeneity effects on deep magnetotelluric sounding. Physics of the Earth and Planetary Interiors 22, 1–11.

Berdichevsky, M. N., Zhdanov, M. S., 1984. Advanced theory of deep geomagnetic sounding. Elsevier, Amsterdam.

Booker, J. R., 2012. Magnetotelluric phase tensor evolution. In: $21^{st}$ Electromagnetic (EM) Induction Workshop Darwin, Australia.

Bronkhorst, D., Mainville, A. G., Murdock, G. M., Yesnik, L. D., 2012. Cameco: McArthor river operation Northern Saskatchewan, Canada. Tech. rep., Cameco.

Cagniard, L., 1953. Basic theory of the magnetotelluric method of geophysical prospecting. Geophysics 18, 605–635.

Caldwell, T. G., Bibby, H. M., Brown, C., 2004. The magnetotelluric phase tensor. Geophysical Journal International 158, 457–469.

Chatterjee, S., Sinharay, R. K., Frugier-Dorrington, T., 2008. Exploration of marine sub-volcanic basins using magnetotellurics - A case study. In: 7th International Conference and Exposition on Petroleum Geophysics. pp. 419–422.

Chave, A. D., Jones, A. G. (Eds.), 2012. The Magnetotelluric Method: Theory and Practice. Cambridge University Press, New York, Ch. 6, pp. 219–302.

Craven, J. A., Farquharson, C. G., Mackie, R. L., Siripunvaraporn, W., Tuncer, V., Unsworth, M. J., 2006. A comparison of two- and three-dimensional modeling of audiomagnetotelluric data collected at the world's richest uranium mine, Saskatchewwan, Canada. In: 18th International Workshop of Electromagnetic Induction in the Earth, Spain.

Egbert, G. D., Kelbert, A., 2012. Computational recipes for electromagnetic inverse problems. Geophysical Journal International 189, 251–267.

Farquharson, C. G., Oldenburg, D. W., Harber, E., Shekhtman, R., 2002. An algorithm for the three-dimensional inversion of magnetotelluric data. 72nd Annual International Meeting of the Society of Exploration Geophysicists, 649–652.

Gribenko, A., Zhdanov, M. S., 2007. Rigorous 3D inversion of marine CSEM data based on the integral equation method. Geophysics 72, WA73–WA84.

Gribenko, A., Zhdanov, M. S., 2011. 3D modeling and inversion of the magnetotelluric phase tensor. Consortium for Electromagnetic Modeling and Inversion Proceedings of 2011 Annual Meeting, 249–263.

Groom, R. W., Bahr, K., 1992. Corrections for near surface effects: Decomposition of the magnetotelluric impedance tensor and scaling corrections for regional resistivities: A tutorial. Surveys in Geophysics 13, 341–379.

Hursán, G., Zhdanov, M. S., 2002. Contraction integral equation method in three-dimensional electromagnetic modeling. Radio Science 37 (6).

Jefferson, C. W., Delaney, G., Olson, R. A., 2003. EXTECH IV Athabasca uranium multi-disciplinary study of northern Saskatchewan and Alberta, Part 1: Overview and impact Current Research 2003-C18. Geological Survey of Canada.

Jefferson, C. W., Thomas, D. J., Gahdhi, S. S., Ramaekers, P., Delaney, G., Brisbin, D., Cutts, C., Quirts, D., Portella, P., Olson, R. A., 2007. Unconformity-associated uranium deposits of the Athabasca Basin Saskatchewan and Alberta. In: Goodfellow, W. D. (Ed.), Mineral Deposits of Canada: A Synthesis of Major Deposit-Types, District Metallogeny, the Evolution of Geological Provinces, and Exploration Methods. Geological Association of Canada, Mineral Deposits Division, Special Publication, pp. 273–305.

Jiracek, G. R., 1990. Near surface and topographic distortions in electromagnetic induction. Surveys in Geophysics 11, 163–203.

Jones, A. G., 1988. Static-shift of magnetotelluric data and its removal in a sedimentary basin environment. Geophysics 7, 967–978.

Lehmann, B., 2008. Uranium ore deposits. Reviews in Economic Geology AMS Online 2, 16–26.

Mackie, R. L., Madden, T. R., Wannamaker, P. E., 1993. Three-dimensional magnetotelluric modeling using difference equations - Theory and comparisons to integral equation solutions. Geophysics 58 (2), 215–226.

McGill, B. D., Marlatt, J. L., Matthews, R. B., Sopuck, V. J., Homeniuk, L. A., Hubregtse, J. J., 1993. The P2 north uranium deposit Saskatchewan, Canada. Mining Geology 2, 321–331.

Ng, R., Alexandre, P., Kyser, K., 2013. Mineralogical and geochemical evolution of the unconformity-related McAurthur River zone 4 orebody in the Athabasca Basin, Canada: Implications of a silicified zone. Economic Geology 108, 1657–1689.

Pankratov, O. V., Kuvshinov, A., 2010. Fast calculations of the sensitivity matrix for responses to the Earth's conductivity. Physics of the Solid Earth 46 (9), 788–804.

Peace, D. G., Schofield, J., Orange, A., Servodio, R., Lansdell, R., Woodfin, M., 2002. Marine magneto-telluric exploration helps unravel secrets of the Faroe Islands. In: Society of Exploration Geophysicists Expanded Abstracts. Vol. 21. p. 600.

Rodi, W., Mackie, R. L., 2001. Nonlinear conjugate gradients algorithm for 2-D magnetotelluric inversion. Geophysics 66 (1), 174–187.

Ruzicka, V., 1996. Unconformity-associated uranium. In: Rckstrand, O. R., Sinclair, W. D., Thorpe, R. I. (Eds.), Geology of Canadian Mineral Deposit Types. No. 8. Geology Survey of Canada, Geology of Canada, pp. 197–210.

Sasaki, Y., 2004. Three-dimensional inversion of static-shifted magnetotelluric data. Earth Planets Space 56, 239–248.

Schmucker, U., 1970. Anomalies of geomagnetic variations in the Southwestern United States. Bull. Scripps Inst. Oceanogr., Univ. of Calif. Press 13, 165.

Simpson, F., Bahr, K., 2005. Practical Magnetotellurics. Cambridge University Press.

Siripunvaraporn, W., Egbert, G., Lenbury, Y., Uyeshima, M., 2005. Three-dimensional magnetotelluric inversion: Data-space method. Physics of the Earth and Planetary Interiors 150, 3–14.

Tikhonov, A. N., 1950. On determination of electric characteristics of deep layers of the Earth crust. Dokl. Acad. Nauk SSSR 151, 295–297.

Travis, B. J., Chave, A. D., 1989. A moving finite element method for magnetotelluric modeling. Physics of the Earth and Planetary Interiors 53, 432–443.

Tuncer, V., Unsworth, M. J., Siripunvaraporn, W., Craven, J. A., 2006. Exploration for unconformity-type uranium deposits with audio-magnetotelluric data: A case study from the McArthur River Mine, Saskatchewan, Canada. Geophysics 71, 201–209.

Zhdanov, M. S., 2002. Geophysicsl Inverse Theory and Regularization Problems. Elsevier, Amsterdam.

Zhdanov, M. S., 2009. Geophysicsl Electromagnetic Theory and Methods. Elsevier, Amsterdam.

Zhdanov, M. S., Smith, R. B., Gribenko, A., Cuma, M., Green, M., 2011. Three-dimensional inversion of large-scale EarthScope magnetotelluric data based on the integral equation method: Geoelectrical imaing of the Yellowstone conductive mantle plume. Geophysical Research Letters 38, 1–7.

Zhu, Y., 2012. Three-dimensional joint inversion of Earthscope magnetotelluric and magnetovariational data. Master's thesis, University of Utah.